Central auditory pathways study using Magnetic Resonance Imaging

Arnaud Attyé

Communauté
UNIVERSITÉ Grenoble Alpes

THÈSE

Pour obtenir le grade de

DOCTEUR DE LA COMMUNAUTÉ

UNIVERSITÉ GRENOBLE ALPES

Spécialité : BIS - Biotechnologie, instrumentation, signal et

imagerie pour la biologie, la médecine et l'environnement

Arrêté ministériel : 25 mai 2016

Présentée par

Arnaud ATTYÉ

Thèse dirigée par **Alexandre Krainik** (EDISCE, UGA)

et codirigée par **Emmanuel Barbier** (Inserm)

préparée au sein du **Laboratoire Grenoble Institut des Neurosciences**

dans **l'École Doctorale Ingénierie pour la santé la Cognition et l'Environnement**

Central auditory pathways studies using Magnetic Resonance Imaging

Thèse soutenue publiquement le 7 décembre 2018

Devant le jury composé de :

Professeur Sébastien SCHMERBER, Président

Docteur Frédérique DUBRULLE, Rapporteur

Docteur Jacques-Donald TOURNIER, Rapporteur

Professeur Claire BOUTET, Examinateur

Professeur Alexandre KRAINIK, Directeur

Docteur Emmanuel BARBIER, Co-Directeur

Short abstract in English

The inner ear is the organ of sound detection and balance. Within the inner ear, there are two distinct compartments filled with endolymph and perilymph. The accumulation of endolymph fluid is called “endolymphatic hydrops” (EH). EH presence is linked to a variety of disorders, including Meniere’s Disease (MD) or internal auditory canal tumors.

In MD, previous studies have demonstrated swelling of cochleo-vestibular nerves, raising the hypothesis that although cellular death would theoretically be expected to lead to a decreased nerve thickness, the increase of nerves diameter will support a mechanism of neuroinflammation.

Diffusion-Weighted Imaging (DWI) play a crucial role because it can help to assess the intracellular compartment of cranial nerves by displaying the Brownian movements of water molecules. The acquisition of High-Angular Resolution DWI data allows to estimate the local Fiber Orientation Distribution (FOD).

This work had two main objectives :

1°) to better characterize the role of EH in sensorineural hearing loss (SNHL) occurrence.

2°) to study auditory pathways alteration in patients with cochleo-vestibular disorders.

1°) EH can be identified using MRI, acquired 4-6-hours after injection of contrast media. We have demonstrated the feasibility and improved this technique in a clinical setting. The current classification for grading the amount of endolymph liquid using MRI is based on a global semi-quantitative evaluation, without distinguishing the utricle from the saccule, whose biomechanical properties are different in terms of compliance.

Using optimized morphological sequences, we were able to illustrate inner ear microanatomy based on temporal bone dissection. In accordance with a multi-compartmental model, we observed that the saccular hydrops was a specific biomarker of SNHL in the context of MD. In these patients, the vestibular aqueduct, a tubular structure linking the brain with the temporal bone, is frequently obstructed.

In patients with schwannomas, we have demonstrated that utricular hydrops was linked to the degree of SNHL, supporting a relationship between endolymph circulation and the internal auditory canal nerves modification.

We raise the hypothesis that both utricle and saccule compartment play the role of a buffer in endolymph reabsorption. When their compliance is overstretched secondary to mechanical

obstruction, inner ear endolymph regulation fails, subsequently leading to cochlear cellular lesions.

Thus, we were able to prove the high prevalence of EH in patients with SNHL.

2°) The second objective was to study the acoustico-facial bundle in patients with cochleo-vestibular disorders using DWI. We have evaluated the role of the Apparent Fiber Density (AFD) coefficient, a recent quantitative biomarker extracted from the FOD, and the potential added value of a newly-developed toolbox, based on Machine-Learning algorithms.

We have started by designing a new method for anatomical structure extraction named Spectral Clustering-based Tractography. The first step of the algorithm was to reduce the FOD Data in a low-dimensional space to perform robust clustering method, as demonstrated with test-retest procedure in the brain. We have then evaluated the value of this approach in MD patients, demonstrating increase of the AFD coefficient, as extracted from the acoustico-facial bundles.

Finally, we have used another algorithm in order to analyze FOD variation between volunteers and patients, named Manifold Learning. The manifold analysis allows to take into account the complex mathematical structure of the spherical harmonics deconvolution from DWI signal. We have tested this new approach on corpus callosum segmentation, with reference to surgical dissection of rhesus monkey, then on neurovascular compression of the acoustico-facial bundle, as a model of unilateral disease.

Thus, we have developed a toolbox efficient in term of computer requirement and at the individual level scale for diagnosis.

Short abstract in French

Dans ce travail de thèse, nous avons cherché à mieux caractériser les surdités neurosensorielles (SNHL) en IRM, et à étudier les altérations potentiellement associées du nerf cochléo-vestibulaire en cas d'hydrops endolymphatique (EH) ou de compression nerveuse.

1°/Nous avons d'abord étudié les liquides de l'oreille interne, l'endolymphe et la périlymphe.

L'EH est supposé être lié à la présence de SNHL et de vertiges récurrents pour de nombreux patients. Nous avons montré que son diagnostic peut être posé en imagerie chez l'homme par une analyse visuelle sur une acquisition 3D-FLAIR réalisée 4 heures après injection de chélates de gadolinium à simple dose.

En isolant l'hydrops sacculaire, nous avons démontré qu'il était lié à la présence de SNHL pour les patients avec une Maladie de Ménière (MD) mais également qu'il pouvait être détecté pour des patients présentant des surdités isolées sur les basses fréquences, qui ne sont habituellement pas classés comme porteurs cliniquement de MD.

Pour les patients porteurs de schwannomes cochléo-vestibulaires, nous avons démontré que le degré de SNHL était cette fois liée à la présence d'un hydrops utriculaire.

Nous avons proposé une théorie bi-compartimentale pour les échanges endolymphe/ liquide céphalorachidien. Nous avons posé l'hypothèse que l'utricule et le saccule joue un rôle de tampon entre le cerveau et la cochlée. En cas d'obstruction mécanique, au niveau de l'aqueduc du vestibule pour la MD et du nerf cochléo-vestibulaire pour les tumeurs du conduit auditif interne ; le tampon ne joue plus son rôle et les contraintes biomécaniques augmentent sur le labyrinthe membraneux. Surviennent alors des lésions cellulaires de la cochlée.

2°/Le second objectif de ce travail de thèse était de mieux caractériser les altérations structurelles neuronales rétro-cochléaires dans un contexte d'EH, mais également de proposer une nouvelle méthode d'analyse du signal de diffusion à l'aide d'algorithme d'apprentissage statistique.

Nous avons décidé d'étudier le nerf cochléaire en IRM de diffusion pour des patients porteurs de la MD mais également de conflit vasculo-nerveux. En cas de MD, les études histologiques ont mis en évidence une perte axonale le long nerf cochléo-vestibulaire, depuis remise en cause par des mesures morphologiques sur des séquences IRM haute résolution.

L'étude du nerf cochléaire en IRM de diffusion possède l'avantage de posséder une structure simple essentiellement composée d'une seule population de fibre à modéliser par voxel, au prix d'une région d'étude compliquée intriquant de l'os, du liquide et de l'air dans l'os temporal. Nous avons donc appris à utiliser des algorithmes de normalisation du champ B0, de correction des artéfacts de Gibbs et des artéfacts de susceptibilité magnétique, de mouvements, de correction des artéfacts de champ B1 et des courants de Foucault.

Nous avons ensuite appris à extraire le coefficient de diffusion apparent des fibres (AFD), directement issus du signal de l'IRM de Diffusion dont nous avons préalablement testé la reproductibilité sur des données de diffusion multi-compartimentale de haute qualité au niveau de l'encéphale.

Nous avons ensuite proposé une méthode originale d'extraction de l'information des voxels du paquet acoustico-faciale appelée *Spectral Clustering* pour obtenir l'AFD au niveau de notre population témoin. Nous avons ainsi démontré que les patients porteurs de la MD présentaient une augmentation de l'AFD, en faisant de particulier bons candidats à l'implantation cochléaire.

Enfin, nous avons implémenté un algorithme d'apprentissage de variété (*Manifold Learning*) pour l'analyse de ce signal de diffusion, dont nous avons montré la capacité à segmenter en cluster anatomique pertinent le corps calleux sans réaliser de processus de tractographie. Le manifold learning surpasse les biomarqueurs scalaires en confrontation à un modèle pathologique de compression vasculo-nerveuse du paquet acoustico-faciale, en tenant compte de l'hétérogénéité du signal de diffusion dans un cluster.

Long abstract in French

Introduction

En 2010, près de 6 millions de français et 36 millions d'américains avaient une baisse de l'audition. Les surdités neuro-sensorielles représentent la principale cause de ce trouble qui peut être appareillé par des aides auditives voire une stimulation neuronale directe par implantation cochléaire.

Le succès de l'implantation cochléaire repose sur l'intégrité respectée du ganglion spiral du nerf cochléaire et des voies auditives antérogrades. L'imagerie complète l'examen clinique et les explorations physiologiques. La prise en charge diagnostique des patients repose sur :

— La tomodensitométrie haute résolution des rochers pour :

a°) éliminer une surdité de transmission à la recherche d'anomalies de l'oreille externe et de l'oreille moyenne

b°) rechercher des anomalies osseuses de l'oreille interne

— L'IRM de l'oreille interne et du cerveau pour rechercher

a°) une étiologie cochléaire ou rétrocochléaire à la surdité

b°) une contre-indication à l'implantation cochléaire

Les surdités neuro-sensorielles

Les principales causes de surdité neuro-sensorielle sont :

1°) *La presbyacousie* qui est liée au vieillissement physiologique et se caractérise par une dégénérescence de l'organe de Corti (presbyacousie sensorielle), et/ou du ganglion spiral (presbyacousie neurale), et/ou de la strie vasculaire (presbyacousie métabolique). Le diagnostic est actuellement porté sur la clinique (gêne aux bruits ambiants) et les épreuves fonctionnelles otologiques (atteinte des hautes fréquences). Les explorations IRM morphologiques de l'oreille interne sont normales.

2°) *L'hydrops endolymphatique* qui est caractérisé par un excès d'endolymphe dans l'oreille interne. L'excès d'endolymphe apparait lié à la maladie de Ménière, dans laquelle s'exprime une atteinte auditive sur les basses fréquences et/ou des vertiges récurrents. Clinique jusqu'en 2007, le diagnostic d'hydrops est actuellement proposé en IRM et reposait avant ce travail de thèse sur une analyse semi-quantitative visuelle de cet endolymphe sur une acquisition réalisée 4 heures après injection de chélates de gadolinium, l'excès d'endolymphe étant visualisé par contraste négatif, seule la périlymphe étant rehaussée par le produit de contraste.

3°) *Les schwannomes du nerf vestbulo-cochléaire* . Il s'agit d'une tumeur bénigne de la gaine de Schwann, débutant au niveau du ganglion vestibulaire dans le conduit auditif interne ou de l'organe de Corti dans la cochlée. Le gold standard de diagnostic est l'IRM injectée. Les schwannomes peuvent être traités chirurgicalement quand ils sont volumineux, nécessitant une visualisation préopératoire du paquet acoustico-faciale pour limiter les risques de paralysie faciale iatrogène.

Une cause plus débattue d'acouphènes et de crises vestibulaires paroxystiques repose sur

les conflits vasculo-nerveux, en l'occurrence la compression du nerf cochléo-vestibulaire par le plus souvent par l'artère cérebelleuse postéro-inférieure. Si les séquences IRM morphologiques classiques permettent de visualiser le contact artère/nerf dans la zone clef constituée de myéline d'origine centrale (root entry zone), l'absence de possibilité d'extraction de biomarqueurs quantitatifs de ces séquences IRM fait défaut en pratique clinique pour évaluer l'état du nerf.

L'IRM de diffusion

Les séquences d'IRM de diffusion permettent d'évaluer le mouvement Brownien des molécules d'eau à partir d'une séquence T2 Echo Planar Imaging en écho de spin sur laquelle sont appliqués, de part et autre du pulse de 180°, 2 gradients de même amplitude.

L'imagerie à haute résolution angulaire est une technique de diffusion dans laquelle les gradients de diffusion sont appliqués successivement dans au moins 30 à 60 directions de l'espace, et non plus seulement dans les trois directions xx', yy' et zz'. L'objectif peut être de modéliser la fonction de distribution des fibres nerveuses dans un voxel (l'orientation dans les 3 plans de l'espace) de façon la plus précise possible afin de réaliser dans un second temps un processus de tractographie robuste.

Pour obtenir cette fonction de distribution de fibre, plusieurs modèles mathématiques existent visant à modéliser proprement l'orientation du signal de diffusion quand un voxel contient au moins 2 populations de fibre différentes. Les différents modèles mathématiques dits «d'ordre élevés» disponible en recherche clinique apparaissent globalement équivalents en confrontation avec l'anatomopathologie, robustes quand il s'agit de modéliser un croisement de fibre orthogonal ou à plus de 30° de dispersion angulaire, moins robuste pour les croisements inférieurs en résolution angulaire.

L'utilisation de séquences IRM de diffusion de type echo-planar imaging induit de nombreux artéfacts qu'il est possible d'atténuer à l'aide de conditions particulières d'acquisition ou de boites à outils de post-traitement. Ainsi les courants de Foucault correspondent à des courants électriques induits par les changements rapides de champ magnétique. Les artefacts de susceptibilité magnétique entraine des erreurs de codage de fréquence et de phase. Ces artefacts prédominent aux interfaces entre des structures aériques et cérébrales, leur correction apparaît particulièrement importante dans cette thèse de par la région étudiée. Ils peuvent être gérés par l'acquisition d'image b=0 dans un sens de blip opposé (postéro-antérieur et antéro-postérieur) pour moyenner ensuite la distorsion. On citera aussi les artéfacts de Gibbs à l'interface avec les structures graisseuses, les artéfacts de champ B1 ou de mouvements.

Travail de thèse

1ère partie : Mieux caractériser les surdités neuro-sensorielles liées à la présence d'un hydrops endolymphatique

Etat des connaissances anatomiques au niveau de l'oreille interne

L'oreille interne est constituée dans la labyrinthe membraneux de deux liquides biologiques différents : l'endolymphe et la périlymphe. Le compartiment endolymphatique est séparé du labyrinthe osseux par le liquide périlymphatique. Le liquide périlymphatique est riche en sodium, pauvre en potassium avec une osmolarité et un contenu en protéines faible. A l'inverse, la composition du liquide endolymphatique est différente de la périlymphe : hyperosmotique, riche en potassium, pauvre en sodium et en protéines.

Le compartiment endolymphatique cochléaire s'enroule dans le labyrinthe osseux cochléaire et occupe la partie externe de la cochlée, entre la rampe vestibulaire et cochléaire. La partie externe du canal cochléaire correspond à la strie vasculaire ; la partie supérieure correspond à la membrane de Reissner ; la partie inférieure correspond à la membrane basilaire où siègent les cellules ciliées internes.

Le compartiment endolymphatique vestibulaire comprend l'utricule, le saccule, les canaux semi-circulaires et le canal endolymphatique. L'utricule occupe la partie supérieure du vestibule osseux au sein de la fossette ovoïde. Les trois canaux semi-circulaires s'y abouchent. Le saccule occupe la partie inférieure et antéromédiale du vestibule au sein de la fossette hémisphérique. Les ampoules des canaux semi-circulaires supérieur et latéral communiquent directement avec l'utricule, alors que celle du canal postérieur est reliée par un petit canalicule.

Le canal endolymphatique naît de la réunion du canalicule utriculaire et sacculaire. Le canal endolymphatique communique par l'intermédiaire de l'aqueduc du vestibule avec le sac endolymphatique qui est situé dans un repli de dure dure-mère à la face postérieure du rocher. Le sac endolymphatique possède plusieurs fonctions : résorption de l'endolymphe, élimination des déchets endolymphatiques, participation à la défense immunitaire de l'oreille interne et transmission des variations de pression du LCR à l'endolymphe.

Physiologie des liquides de l'oreille interne

La sécrétion de périlymphe peut provenir de deux sources différentes :

1°) Le plasma par l'intermédiaire de la barrière hémato-périlymphatique. Cette barrière est constituée de cellules endothéliales unies par des jonctions serrées. Elle ne permet pas le passage des macromolécules. Cependant, elle permet un passage sélectif des électrolytes et des molécules hydrosolubles neutres en fonction de leur poids moléculaire.

2°) Le Liquide céphalo-rachidien. Les espaces sous-arachnoïdiens communiquent avec la rampe tympanique du tour basal de la cochlée par l'intermédiaire de l'aqueduc cochléaire lorsque ce dernier est perméable (30% des cas). L'aqueduc cochléaire permet l'adaptation rapide de la pression périlymphatique aux changements rapides de pression de LCR. Cependant, lorsqu'il est obstrué, l'équilibre des pressions est limité et retardé. Le changement de pression du LCR est d'abord transmis au sac endolymphatique puis à l'endolymphe et enfin au liquide périlymphatique. Le drainage de la périlymphe se fait dans le conduit auditif interne. La présence de micropores au sein du modiolus autorise un passage de la périlymphe à travers ce dernier pour rejoindre le conduit auditif interne.

Le liquide précurseur de l'endolymphe est la périlymphe et non le plasma. La sécrétion de l'endolymphe se fait par la strie vasculaire du canal cochléaire et les cellules sombres de l'utricule, du saccule et des ampoules. Le drainage de l'endolymphe se fait au niveau du sac endolymphatique par l'intermédiaire de l'aqueduc du vestibule. D'un point de vue biomécanique, le modèle actuellement répandu est celui de Pender qui en réalisant une méta-analyse d'études sur l'os temporal a mis en évidence qu'il existait une répartition cochléocentrique de la maladie hydropique (cochlée puis saccule puis utricule puis ampoules).

Etude en IRM de l'endolymphe

Concernant la pathologie obstructive de l'endolymphe, l'étude pré-clinique apparaît difficile, les modèle d'hydrops endolymphatique génétique ou mécaniques étant débattus sur l'animal, et de nombreux auteurs considèrent qu'il n'existe pas de modèle pré-clinique de la maladie de Ménière.

Néanmoins, En 1999, Counter et ses collègues étudient en IRM 4,7 T le compartiment endolymphatique cochléaire chez le cochon d'inde, après une injection intraveineuse de gadolinium. Ils démontrent que l'injection de gadolinium diffuse préférentiellement vers la périlymphe à travers la barrière hémato-périlymphatique. En effet, la barrière hémato-périlymphatique est similaire à la barrière hémato-encéphalique et permet le passage de molécules de bas poids moléculaire tel que la taurine, le mannitol, les hormones stéroïdiennes et le gadolinium. A l'inverse les barrières hémato-endolymphatique et perilymphatique-endolymphatique sont imperméables au gadolinium. Ce passage préférentiel du gadolinium offre une image contrastée entre la périlymphe imprégnée de gadolinium, et donc en hypersignal, et l'endolymphe en hyposignal.

Les premières images de l'endolymphe en IRM in vivo chez l'homme remontent à 2007, et ont été apportés par l'équipe de Pr Shinji Naganawa (Nagoya, Japon) à l'aide d'une injection intra-tympanique de gadolinium dilué et d'une acquisition des images réalisées 24 heures après cette injection. A suivi à cette publication princeps d'importants travaux méthodologiques sur les séquences IRM d'inversion récupération et le passage de la voie intra-tympanique à la voie intra-veineuse, d'abord avec une double dose de produit de contraste gadoliné, puis maintenant à simple dose.

Concernant la quantification de l'endolymphe, le diagnostic de l'hydrops est actuellement porté chez l'homme par une analyse semi-quantitative visuelle sur une acquisition réalisée 4 heures après injection de chélates de gadolinium, suivant la publication des Prs Nakashima et Naganawa en 2009. Cependant, les seuils pathologiques restent débattus dans la littérature, et l'absence d'individualisation au sein du vestibule du saccule, responsable de l'équilibre statique lors de mouvement verticaux (exemple : dans un ascenseur) et de l'utricule, l'organe de l'équilibre statique horizontal (accélération linéaire au volant d'une voiture) limite l'utilisation de cette classification en pratique courante.

Dans ce travail de thèse, nous avons étudié deux modèles de maladie responsables de surdité neuro-sensorielle en rapport avec une accumulation d'endolymphe : la maladie de Ménière et les schwannomes cochléo-vestibulaire, afin de mieux comprendre la circulation de l'endolymphe et les corrélations clinico-radiologiques.

Nouvelles connaissances issues du travail de thèse concernant l'imagerie de l'endolymphe

Nous avons démontré que nous étions capables d'utiliser en soin courant une sé-

quence 3D-FLAIR pour faire le diagnostic d'hydrops endolymphatique 4 heures après l'injection d'une simple dose de produit de contraste gadoliné. En publiant la première étude cas-témoin pour poser le diagnostic d'hydrops endolymphatique, **nous avons démontré que le grading semi-quantitatif ne permettait pas avec notre séquence IRM de différencier les patients symptomatiques de la maladie de Ménière des témoins; tandis que l'analyse fine du saccule était beaucoup plus spécifique.**

D'un point de vue mise au point de séquence IRM, nous avons d'abord démontré que la fusion de séquence 3D-FLAIR/Hyper-pondération T2 permettait de diminuer le signal de l'os temporal pour le distinguer de l'endolymphe, ce qui était particulièrement utile pour les internes de radiologie peu familiers de la radioanatomie temporale. Néanmoins le processus de co-registration est chronophage en pratique clinique et dans notre expérience peut produire de fausses images d'hydrops cochléaire. **Nous avons ensuite démontré que la séquence Brainview du constructeur Philips permettait d'individualiser le saccule et l'utricule pour faire le diagnostic d'hydrops compartiment par compartiment, sans nécessité de processus de fusion d'image.**

Nous avons donc défini la présence de l'hydrops sacculaire comme une inversion du rapport entre le saccule et l'utricule, afin d'utiliser l'utricule comme un repère anatomique constant avec une surface peu modifiée en condition pathologique de par son manque de compliance dans sa portion vestibulaire. Le rationnel repose sur les propriétés biomécaniques différentes de ces deux structures notamment en termes de compliance. **En isolant l'hydrops sacculaire, nous avons démontré qu'il était lié à la présence de surdité neurosensorielle** pour les patients avec une Maladie de Ménière mais également qu'il pouvait être détecté pour des patients présentant des surdités isolées sur les basses fréquences, qui ne sont habituellement pas classées comme porteurs cliniquement de la Maladie de Ménière.

Nous avons également étudié l'influence du produit de contraste sur le rehaussement de la périlymphe, démontrant que le Gadovist, produit par Bayer, permettait grâce à sa double concentration (avec deux fois moins de quantité de produit injectée) de mieux rehausser la périlymphe pour faire une analyse visuelle plus fiable du saccule normal sur des machines General Electric à l'aide d'une séquence 3D-FLAIR.

D'un point de vue paramètres d'acquisition, nous avons testé l'influence du temps d'inversion sur la surface occupée par le saccule et l'utricule, démontrant que sur la même machine, **la simple variation de 100 ms du TI entrainait une importante modification du rapport endolymphe/perilymphe** rendant inutilisable le grading semi-quantitatif en pratique clinique. En cas de variation du TI, étant donné que toute l'endolymphe est concernée par une variation de volume apparent, le ratio utricule/saccule reste identique.

Nous avons ensuite étudié l'aqueduc du vestibule, correspondant à la paroi osseuse du conduit endolymphatique qui relie l'oreille interne au cerveau. Les études pré-cliniques suggérent que lors de la survenue de l'hydrops endolymphatique, les concentrations de Sodium et de Potassium dans l'endolymphe varient peu entre les oreilles saines et pathologiques, au contraire de la concentration en Calcium qui augmente de façon significative. De précédentes études en imagerie CT ou CBCT (Cone Beam CT) démontrent des calcifications de l'aqueduc du vestibule pour les patients porteurs de la maladie de Ménière. Nous avons donc étudié l'aspect morphologique de l'aqueduc sur des séquences FLAIR sans et avec injection tardive dans une nouvelle étude contrôlée, **démontrant que l'aqueduc s'ossifié de façon bilatérale pour les patients porteurs**

de maladie de Ménière à expression clinique unilatérale.

Nous avons finalement mis au point une séquence 3D-FLAIR utilisable en pratique clinique pour la détection d'hydrops sacculaire, utilisable à 1.5T comme à 3T sur des imageurs Philips, General Electric ou Siemens, en passant d'une séquence à angle de bascule variable à une séquence à angle de bascule constant pour augmenter le rapport signal sur bruit lié à la présence de gadolinium dans l'oreille interne, et être plus sensible aux ruptures de la barrière hémato-labyrinthique fréquente dans de nombreuses pathologies cochléo-vestibulaires.

Pour les patients porteurs de schwannomes cochléo-vestibulaires, nous avons démontré que le degré de perte auditive était cette fois liée à la présence d'un hydrops utriculaire. Ce diagnostic peut être porté sans injection de produit de contraste puisque la présence d'un schwannome obstructif entraine mécaniquement une augmentation du taux protidique dans la périlymphe et donc une discrimination périlymphe/ endolymphe sur les séquences T2 en echo de gradient.

Enfin, nous avons challenger la portabilité de notre classification en mettant à disposition des autres équipes de recherche clinique nos data IRM sur sujets sains et pathologiques sur à l'aide d'une database online. Un travail de review des études d'imagerie contrôlées par une population témoin concernant la maladie de Ménière a également été soumis en collaboration avec l'équipe du Pr Lopez-Escamez (Granada, Spain), qui a publié la classification clinique de référence pour la maladie de Ménière en 2015.

En revisitant l'anatomie histologique avec la remnographie, nous avons proposé une théorie bi-compartimentale pour les échanges liquides lymphatiques/liquide céphalorachidien. Nous avons posé l'hypothèse que l'utricule et le saccule joue un rôle de tampon entre le cerveau et la cochlée. En cas d'obstruction mécanique, au niveau de l'aqueduc du vestibule pour la maladie de Ménière et du nerf vestibulaire supérieur pour les tumeurs du conduit auditif interne ; le tampon ne joue plus son rôle et les contraintes biomécaniques augmentent sur le labyrinthe membraneux. Surviennent alors des lésions cellulaires des stéréocils de la cochlée et la surdité attenante. Nous avons également oeuvré à la portabilité du protocole hydrops, en testant sa robustesse en fonction du produit de contraste, du temps d'inversion de la séquence 3D-FLAIR, en partageant notre database via des publications scientifiques et en proposant des séquences IRM utilisables dans des temps d'utilisation compatibles avec la pratique clinique et sur des IRM 1.5 Tesla et 3 Tesla.

2ème partie : Evaluer l'altération potentielle des voies auditives centrales en IRM de Diffusion

La déconvolution sphérique contrainte

L'augmentation de la puissance des aimants des machines IRM, la numérisation du signal RMN et la présence de technique d'accélération multi-coupes expliquent la réduction drastique des temps d'acquisitions des séquences de diffusion EPI et l'arrivée en pratique clinique de séquences de diffusion à haute résolution angulaire.

Classiquement, on parle de haute résolution angulaire à partir de 30 à 60 directions de gradient tandis que le modèle dit de tenseur de diffusion ne demandait que 6 directions de diffusion pour permettre la reconstruction des faisceaux de substance blanche cérébrale. La limite majeure du modèle tenseur, énoncé dès le papier princeps de Basser en 1995, repose sur l'impossibilité de modéliser 2 populations de fibres de directions différentes dans un même voxel.

On pensait à l'époque que les voxels à «croisement de fibres» ne concernaient qu'une partie mineure du cerveau (essentiellement le tronc cérébral) alors que les estimations actuelles évoquent de 70% à 90% des voxels du cerveau possédant au moins 2 populations de fibres. L'apport supplémentaire d'information spatiale induite par les acquisitions de diffusion haute résolution permet l'utilisation de modèles mathématiques complexes pour estimer la fonction d'orientation de la densité de fibre, également dénommée fonction de distribution d'orientation.

Il existe globalement 2 catégories de modélisation du signal de diffusion visant à estimer respectivement la fonction de distribution d'orientation de la diffusion, qui inclut donc les fibres mais également le mouvement libre des molécules d'eau ; et la fonction de distribution d'orientation des fibres, sujet de ce travail de thèse.

L'estimation de la distribution des fibres nécessite de poser des hypothèses à priori, comme celle d'échange négligeable de molécules d'eau entre les compartiments intra et extra-cellulaire durant le temps d'acquisition de la séquence IRM de diffusion ; ou celle d'une isotropie de la substance grise et du liquide céphalo-rachidien, en opposition avec une anisotropie de la substance blanche ou des nerfs crâniens dans notre étude.

La déconvolution sphérique contrainte est le modèle le plus populaire d'estimation de la distribution d'orientation des fibres. Elle suppose que le signal de diffusion est la convolution de la distribution d'orientation des fibres avec le signal de diffusion correspondant à une seule population de fibre, appelée fonction de réponse. Ayant estimé cette fonction de réponse, la déconvolution permet d'estimer la distribution d'orientation des fibres. Cependant ce problème nécessite des contraintes de positivité pour répondre à des considérations physiques. Mathématiquement, les différentes fonctions sont modélisées par des harmoniques sphériques. Ce modèle de diffusion est disponible à l'aide du logiciel MRtrix initialement développé par l'équipe du Brain Research Institute de Melbourne (Australie).

Etude des voies auditives centrales centrée sur le nerf cochléaire : rationnel

Les voies auditives centrales pour l'homme débutent au niveau du nerf cochléaire dans le faisceau acoustico-facial avant d'inclure des faisceaux de fibres blanches via le lemnisque latéral qui ont pour relais le complexe olivaire supérieur, le colliculus inférieur, le corps genouillé médial du thalamus puis le cortex du gyrus de Heschl.

Nous avons décidé dans cette thèse d'étudier le nerf cochléaire en IRM de diffusion pour

mieux caractériser les relations entre lésions endocochléaires et rétrocochléaires. Le choix du nerf cochléaire est à la fois théorique et pratique. On peut d'abord supposer qu'en cas d'altération neuronale antérograde les modifications débuteront à ce niveau en tant que premier relais de l'influx auditif. Dans le cas particulier des maladies liées à la dérégulation du système endolymphatique, les données de la littérature sont contradictoires : les études histologiques ont mis en évidence au début des années 1990 une perte axonale, depuis remise en cause par des mesures morphologiques sur des séquences IRM haute résolution.

Hors l'enjeu est crucial puisque les surdités sur les basses fréquences peuvent être stimulée par implantation chirurgicale cochléaire. Après avoir démontré dans la première partie de thèse que le mécanisme de l'hydrops était également la cause de surdité sévère isolée, il apparait important d'apporter au chirurgien otologiste une information sur l'état du nerf cochléaire à visée pré implantatoire. La formulation d'une théorie d'écoulement de l'endolymphe via la gaine des nerfs crâniens renforce l'intérêt d'apporter des marqueurs quantitatifs extraits de l'étude IRM de diffusion du conduit auditif interne.

Du point de vue biophysique de l'IRM de diffusion, l'étude du nerf cochléaire possède l'avantage de posséder une structure simple essentiellement composée d'une seule population de fibre à modéliser par voxel, au prix d'une région d'étude compliquée intriquant de l'os, du liquide et de l'air dans l'os temporal.

Le *gold standard* actuel en tractographie des nerfs crâniens repose sur des algorithmes probabilistes, qui génèrent un grand nombre de fibres probables à partir d'un point de départ et établissent une probabilité d'orientation vers une ou plusieurs directions. Ce modèle de reconstruction des fibres permet de réduire l'incertitude liée au bruit et à la présence de liquide cérébro-spinal ou de tumeur dans un même voxel, nécessitant cependand un temps de calcul informatique important.

D'un point de vue validation méthodologique, nous avons d'abord étudié la position du paquet acoustico-faciale, estimé par tractographie probabiliste, en pathologie tumorale de la base du crâne, qui possède l'intérêt de pouvoir être confronté à la "vérité de terrain" du chirurgien à visée qualitative (position correcte ou incorrecte du nerf tel que reconstruit par la tractographie).

Enfin, l'étude du conduit auditif interne en condition de compression vasculaire (conflit neuro-vasculaire) permet d'allier la force du «ground truth» et d'un modèle de maladie pour laquelle le nerf est peu ou pas déplacée, de façon unilatérale, et altéré sur le plan histologique. C'est un modèle permettant de tester la fiabilité de l'IRM de diffusion pour le recueil d'information quantitative plutôt que qualitative dans le cas des tumeurs compressives.

La réduction de dimension pour l'étude du signal de diffusion

Tous les médecins intéressés par la recherche clinique ont déjà fait l'expérience lors de leur recueil de données quantitatives de réponses laconiques de leur statisticien, indiquant que leur échantillon numérique ne suit pas la loi «normale» (ou loi de Gauss) et que les analyses vont donc être limitées. Or nous travaillons sur le corps humain, sur des régions anatomiques qui de par leur complexité (variabilité anatomique chez le sujet sain, plasticité. . .) ou les processus physiopathologiques intriqués peuvent entrainer des distributions statistiques irrégulières. C'est tout l'intérêt de l'apprentissage statistique (ou *Machine Learning*), par des techniques de réduction de dimension comme le *Spectral Clustering* ou l'apprentissage de variété (en anglais *Manifold Learning*).

En IRM de diffusion, nous sommes souvent confrontés à la problématique suivante : nos jeux de données présentent de multiples dimensions (ici la fonction d'orientation de distribution des fibres) qui nécessitent une étape de «réduction » afin de pouvoir capturer uniquement les degrés de liberté pertinents des ces données pour une analyse plus robuste. Le cerveau humain fait ça au quotidien par exemple en extrayant des informations visuelles pertinentes de 10 millions de fibres des nerfs optiques pour nous en simplifier l'intégration.

Un premier algorithme pertinent pour résoudre cette problématique est le *Spectral Clustering*, qui permet de regrouper des voxels proches spatialement en se basant sur des graphes de similarité, l'idée étant pour l'étude des nerfs crâniens de regrouper entre eux les voxels le long du nerf étudié sans avoir dans le cluster dédié de voxels contenant majoritairement du liquide céphalo-rachidien ou des tissus non nerveux adjacents. Contrairement au processus de tractographie, le *Spectral Clustering* demande très peu de ressources informatiques et s'obtient sans supervisation.

Le second domaine novateur pour l'analyse statistique en imagerie médicale est le *Manifold Learning*. L'article fondateur qui a emmené le *Manifold Learning* vers des horizons prometteurs est paru dans *Science* en 2000. Il proposait une méthode de «capture» des degrés de liberté non linéaires pour rendre compte au mieux de la variabilité de nos données cliniques. Jusqu'à la fin du XXème siècle, les analyses statistiques étaient limitées par leur difficulté à capturer les degrés de liberté non linéaires des données. Un exemple de la vie courante est la reconnaissance automatique de visages, comme elle est pratiquée en Chine : il suffisait que le visage soit de biais ou ombré pour faire échouer l'algorithme. En radiologie, de nombreuses start-up butent sur l'interprétation radiologique, par exemple pour détecter automatiquement une fracture fémorale, dès que le cliché est mal centré ou artéfacté par rapport à la base de données d'apprentissage.

L'algorithme *Isomap* publié par l'équipe de Tenenbaum a donné lieu à des développements informatiques « Open Source», nous permettant d'accéder à ces outils gratuitement pour nos études cliniques. Il s'agit d'une sous classe de *Machine Learning* initialement non supervisé puisque reposant sur une meilleure visualisation de données complexes, sans étiquetage initial entre données «saines» et «pathologiques». Charge à nous dans un second temps de trouver la meilleure méthode d'analyse pour récupérer une information clinique.

Habituellement l'IRM de diffusion nous permet d'extraire à la console des cartes de valeurs scalaires, par exemple le coefficient apparent de diffusion ou le coefficient apparent de densité des fibres (qui correspond à une estimation du volume de la fonction de distribution des fibres). Or, il s'agit toujours d'une simplification d'un volume de diffusion qui comporte de multiples caractéristiques dans un espace en 3 dimensions, le voxel. L'utilisation du *Manifold Learning* sur l'intégralité du signal permettrait théoriquement d'en capturer la structure géomètrique, de construire un atlas des formes variables chez nos sujets sains et de l'adapter à l'exploration des maladies, qu'elle soit associée à une diminution du signal (atrophie nerveuse, musculaire. . .) ou à une augmentation de celui-ci (extensions nerveuses péri-tumorales par exemple).

Contrairement au *Deep-Learning*, efficace mais avec un effet «black box» lié à l'absence de modèle à priori puisque l'algorithme repose sur les données en elle-même plutôt que sur une hypothèse physiopathologique, nous maitrisons ici les étapes de traitement de données de façon compréhensible. C'est une façon d'approcher l'intelligence artificiel adaptée aux études avec peu de patients, en s'affranchissant des contraintes du «big data». Il reste à tester ces nouveaux outils pour que leur utilisation ne reste pas cantonné à un effet de mode et n'échappe aux radiologues.

Nouvelles connaissances issues du travail de thèse concernant l'intelligence artificielle pour l'analyse de l'IRM de diffusion et ses applications sur les altérations du paquet acoustico-facial

Nous avons donc commencé par apprendre à utiliser **une chaine d'algorithme de pré-traitement** des données de diffusion qui utilise les toolbox récentes pour corriger les artéfacts de susceptibilité magnétique, de mouvements, de champ B0 et B1, les courants de Foucault, les artéfacts de Gibbs. Nous avons utilisé une séquence de Diffusion optimisée pour être utilisable en pratique clinique en cas de mouvements des patients, construite par bloc de 15 directions, préalablement appliquée pour l'étude des voies optiques. L'objectif était de modéliser de la façon la plus propre possible le signal de diffusion pour ensuite utiliser la déconvolution sphérique contrainte afin d'estimer l'orientation de distribution des fibres.

Nous avons donc ensuite transféré ces connaissances vers nos confrères Lyonnais afin de réaliser une étude clinique de grande envergure pour évaluer l'intérêt de la déconvolution sphérique contrainte dans une population de patients opérés de tumeurs de la base du crâne. L'objectif était de faire de la tractographie probabiliste qualitative afin de repérer les nerfs de la base du crâne en pré-opératoire. **Nous avons ainsi montré que la déconvolution sphérique contrainte permettait de façon robuste de planifier l'acte neurochirurgical et de modifier dans un nombre important de cas l'abord anatomique choisi.**

Nous avons ensuite extrait le coefficient apparent de diffusion des fibres, directement issus du signal de diffusion et qui est proportionnel au volume axonal orienté dans cette direction à valeur de facteur b élevée. Nous avons préalablement testé la reproductibilité du coefficient de diffusion apparent des fibres sur des données de diffusion multi-compartimentale de haute qualité au niveau de l'encéphale. En effet, nous avons bénéficié de l'acquisition de données de diffusion à plusieurs valeurs de b sur le cerveau selon une **procédure de test-retest, qui consistait à explorer 3 fois sur une année 15 jeunes patients en IRM de diffusion.** Nous avons utilisé sur cette population une version adaptée de la déconvolution sphérique contrainte aux données multi-compartimentales, puis utilisé la méthode du *Spectral Clustering* pour extraire la structure du corps calleux, en confrontation avec des IRM pondérées en T1, anatomiques.

A partir de ces clusters, nous avons démontré que le coefficient apparent de diffusion des fibres était extrêmement reproductible d'une session IRM à l'autre. Nous avons ensuite démontré comment **le Manifold Learning permettait de représenter différentes parties du corps calleux dans des espaces statistiques de dimension réduite et contrôlée**, de façon robuste dans le temps, en individualisant des clusters basés sur l'amplitude de la fonction de distribution d'orientation des fibres, cohérents avec l'anatomie post-mortem sur l'animal. Il s'agit d'une méthode innovante de segmentation du corps calleux, réalisable d'habitude avec un post-traitement complexe de type tractographie.

Nous avons ensuite appliqué la méthode de *Spectral Clustering* pour extraire le coefficient apparent de densité des fibres le long des paquets acoustico-facial de notre population témoin et de patients porteurs de la maladie de Ménière. **Nous avons comparé le *Spectral Clustering* à la tractographie probabiliste, démontrant que l'extraction de cluster basé sur les métriques de type amplitude permettait d'obtenir une représentation anatomique plus réaliste que la tractographie probabiliste** du trajet du paquet acoustico-facial dans le conduit auditif interne.

Nous avons enfin montré que les patients porteurs de la Maladie de Ménière pré-

sentaient bien une augmentation de la densité de fibre du paquet acoustico-facial, concordante avec des études anatomiques récentes en IRM morphologique. Ces résultats sont également concordants avec les bons résultats de l'implantation cochléaire dans la réhabilitation auditive des patients avec une maladie de Ménière avancée.

Finalement, nous avons implémenté un algorithme de *Manifold Learning* pour l'analyse de la fonction de distribution d'orientation des fibres dans nos clusters acoustico-facial. Pour des patients opérés porteurs de compression vasculo-nerveuse, avec des lésions histopathologiques de démyélinisation, **nous avons montré la valeur ajoutée d'une méthode d'analyse statistique originale dans l'espace réduit basée sur des estimations de densité par noyau.** Cette méthode surpasse notre biomarqueur scalaire de référence en tenant compte de l'hétérogénéité du signal de diffusion dans un cluster. Il s'agit d'une avancée majeure puisque dans notre étude le coefficient de densité apparent des fibres ne permettait pas de détecter les anomalies nerveuses.

Nous avons démontré qu'il était possible d'extraire des informations quantitatives de l'imagerie IRM de diffusion de régions anatomiques cohérentes à l'aide d'algorithmes d'apprentissage statistique. L'association des techniques de *Spectral Clustering* et de *Manifold Learning* a une utilité potentielle à visée exploratoire sur un groupe de patient ; ou pour faire du diagnostic individuel. Nous avons en effet montré que les patients avec la maladie de Ménière présentaient des nerfs cochléo-vestibulaires sans atteinte en IRM de diffusion, confirmant l'efficacité observée de l'implantologie cochléaire. Nous avons également proposé une nouvelle méthode de diagnostic individuel des atteintes démyélinisantes des nerfs crâniens avec comme modèle pathologique les conflits vasculo-nerveux. Nous avons appris à utiliser des outils Python extremement rapide en terme de temps de calcul informatique qui permettent d'analyser la géométrie complexe du signal de diffusion dans un espace statistique réduit et contrôlé. Cette approche basée sur une méthode d'intelligence artificielle nous semble promise à un bel avenir dans d'autre régions anatomiques et pour d'autres modèles pathologiques.

ABBREVIATIONS

AFD : Apparent Fiber Density
CSF : Cerebrospinal fluid
cVEMP : Cervico vestibular-evoked myogenic potential
CSD : Constrained Spherical Deconvolution
DPOAEs : Distorsion product otoacoustic emissions
DTI : Diffusion Tensor Imaging
DWI : Diffusion Weighted Imaging
EH : Endolymphatic Hydrops
EcochG : Electrocochleography
FA : Fractional Anisotropy
FOD : Fiber Orientation Distribution
FLAIR : Fluid Attenuated Inversion Recovery
Isomap : Isometric Feature Mapping
MD : Meniere's disease
fODF : Fiber Orientation Density Function
RF : Response Function
ROI : Region of Interest
SC :Spectral Clustering
SH :Spherical Harmonics
SIR :Signal Intensity Ratio
SNR : Signal to Noise Ratio
SNHL : Sensorineural Hearing Loss
SURI : Saccule to utricle ratio inversion
TI : Inversion Time
VA :Vestibular Aqueduct
VBA :Voxel Based Analysis
VISTA : Volume Isotropic TSE acquisition

TABLE OF CONTENTS

TABLE DES FIGURES

FIGURE **Page**

CHAPITRE 1

ENDOLYMPHATIC LIQUID EXPLORATION USING MRI

1.1 Evidence from temporal bone analysis

Prosper Ménière, in 1861, was the first physician to suspect that recurrent attacks of vertigo accompanied by tinnitus and hearing loss were due to a crisis in the inner ear rather than the central nervous system as was commonly believed. The inner ear contains the neurosensory organs of hearing and equilibrium, receiving the terminal distributions of the auditory and vestibular nerves. It is known as the labyrinth with 2 parts : the osseous labyrinth, and the membranous labyrinth, which is filled by two liquids : the endolymph and the perilymph (figure 1.1).

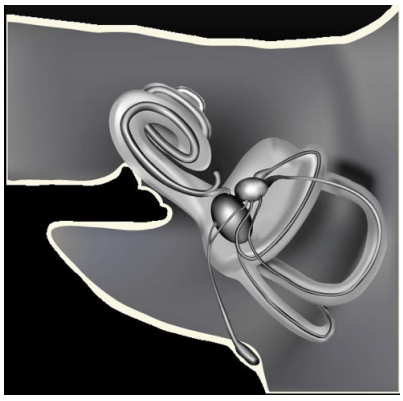

FIGURE 1.1 – **Schematic illustration of the membranous labyrinth**. The dark grey structures (cochlear duct, saccule, utricle, ampullae, endolymphatic duct) contain the endolymphatic liquid, while the light grey structures contain the perilymphatic liquid.

The first temporal bone laboratory in the United States was developed at Johns Hopkins Hospital early in the 20th century, by Stacey Guild, Ph.D. He firstly identified in 1927 the temporal bone endolymphatic sac as the site of “outflow of inner ear endolymph” in his study of guinea pigs.

This study was a major insight into the mechanics of endolymphatic flow in the inner ear, allowing Hallpike [1] to describe endolymphatic hydrops (EH) in 1938. EH represents a pathologic anatomic finding in which the structures bounding the endolymphatic space are distended by an enlargement of endolymphatic volume. The degree of distension appears to be related to the mechanical compliance of membranous components of the inner ear.

These structures contain endolymph, and a change in volume of these structures is tightly correlated with the symptoms of Meniere's Disease (MD), as observed on human temporal bone analysis and in animal models of MD [2]. The diagnostic criteria for MD now includes two categories : definite MD and probable MD [3], based on clinical examination and without the necessity of advanced vestibular or audiological testing. In this classification, Probable MD includes episodes of spontaneous vertigo, lasting from 20 minutes to 12 hours and fluctuating aural symptoms while Definite MD requires the addition of audiometrically documented low- to medium-frequency sensorineural hearing loss in one ear. The aetiology is multifactorial yet a characteristic sign in this disease is endolymphatic hydrops (EH), a disorder in which excessive endolymph accumulates in the inner ear and causes damage to the ganglion cells.

In temporal bone studies of MD patients, EH typically involves the pars inferior of the labyrinth, mainly the saccule [4]. Saccular hydrops can range from mild to severe (Figure 1.2), based on the degree of membrane distension toward the stapes footplate, as seen in post-mortem studies [5].

A recent meta-analysis of temporal bone studies also proposed a cochleocentric distribution of the endolymph fluid with constant cochlear duct dilatation in healthy subjects [7]. Furthermore, the degree of distension of the inner ear structures appears to be related to their mechanical compliance, which is high in the case of the saccule, but lower for the utricle and semi-circular canals [8].

Besides MD, Vestibular schwannomas are benign neurogenic tumors, which can involve a surgical approach depending on the growth potential and their relationship with brain structures. In Vestibular Schwannoma condition, Hizli et al. [9] observed with histopathological examination EH involving the saccule in 50% of cases and involving the utricle in 40% of cases, while Mahmud et al. [10] never reported EH in non-operated schwannoma when speech discrimination was greater than 50%. Schindler et al. [11] demonstrated that the endolymphatic sac presents similar changes in patients with Meniere's disease and in patients with schwannoma suggesting that endolymphatic sac degeneration is the result of the disease potentially leading to EH.

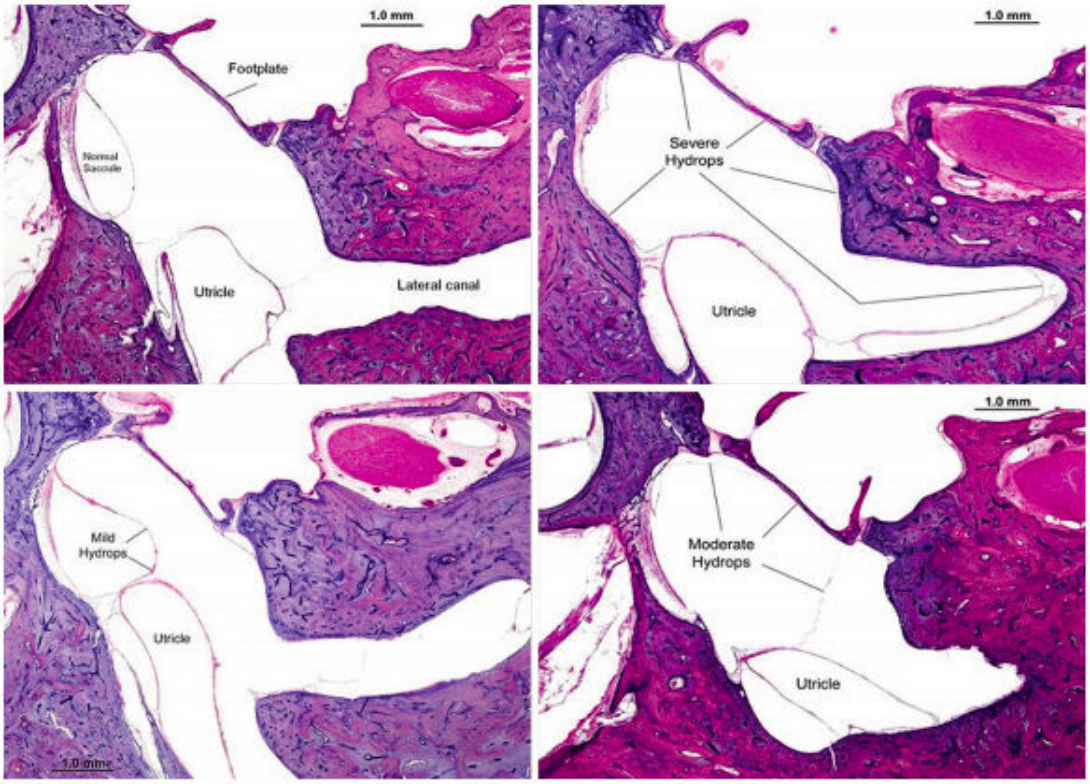

Fig. 1. Grading scale for saccular hydrops: upper left panel, normal; lower left panel, mild hydrops; upper right panel, moderate hydrops; and lower right panel, severe hydrops.

FIGURE 1.2 – **Grading scale for saccular hydrops on pathological analysis**, from [6]. It has established to score the severity of saccular hydrops in sections examined by light microscopy.

1.2 MRI sequence setting to explore the endolymphatic liquid

Rationale

The method of MRI Hydrops evaluation in MD patients requires contrast media injection and delayed acquisition, in order to selectively enhances the perilymphatic fluid [12]. Two alternative routes for contrast media administration have been assessed : intratympanic and intravenous. The main advantage of an intratympanic injection is a higher perilymphatic contrast, particularly in the basal turn of the cochlea, although previous studies suggest this method can cause local toxicity in animal models [13]. However, cases of bilateral disease require a double intratympanic injection and MR scan waiting time of 24 h before imaging acquisition. In contrast, the intravenous method requires a shorter waiting time, which has been evaluated as optimal in the 4.5-6 hours interval. Initially, complex acquisition methods using a Siemens® MRI scan required a 3D-Inversion Recovery (IR) sequence with different Inversion Time (TI), giving the ability to differentiate between endolymph, perilymph, and bone in a single image [14]. However, 3D-IR is not as sensitive to low concentration of contrast media as 3D-FLAIR, requiring intratympanic injection [15].

A grading method for the degree of EH has been proposed with the IR sequence [16]. Authors have divided hydrops grades into three categories : none, mild and significant, both in the cochlea and the vestibule. This semi-quantitative grading system was initially based on the histopathology of the dilated endolymphatic spaces, with separate evaluations for the vestibule and the cochlea, yet the saccule and the utricle were not individually evaluated. This is important because these two structures have different biomechanical properties. We have hypothesized in this work that each compartment follow a different communication route between the inner ear and the intracranial spaces, requiring separate evaluation.

We aimed at optimizing a 3D-FLAIR sequence for direct anatomical visualization of the saccule and the utricle using single dose injection of contrast media with delayed acquisition.

Summarized methods

First study, published in European Radiology 2015 [17]

Firstly, we have evaluated whether 3D-FLAIR sequences using a variable flip angle with single-dose injection of contrast media enables EH visualization only 4 hours after a single-dose intravenous injection of gadolinium. Previous studies have used double-dose of contrast media injection for exploration of the hydrops disease. A volume isotropic TSE acquisition (Philips 3D-FLAIR VISTA® sequence) technique was used for this work.

In this retrospective study, we have included 132 patients with various forms of MD [17]. Inter-rater agreement on detecting EH with the semi-quantitative grading method was estimated using Cohen's kappa coefficient for the FLAIR sequence before and after subtraction with the heavily-

weighted T2 sequence. The objective of the subtraction process was to distinguish endolymph liquid from temporal bone by nulling out the MR signal of the bone (Figure 1.3).

Second study, published in European Radiology 2017 [18]

The parameters of the 3D-FLAIR sequences has been then modified in this study because we have observed that the flip angle variation during the acquisition was important for distinguishing subtle inner ear structures, in particular to precisely display the saccule boundaries. We have then decided to use the Philips 3D-FLAIR View® MR sequence instead of the Vista® MR sequence. The View technique used small refocusing control angles, adapted to specific tissue properties. We have provided a table for comparing Philips View® and Vista® sequence parameters. We have then assessed the possibility of constantly displaying the normal saccule using the View® MR sequence, publishing for the first time a case-controlled MRI study using the Hydrops protocol in 30 volunteers and 30 MD patients.

To assess the usefulness of saccular imaging, we have proposed a new measure based on the size and morphology of the saccule obtained with the saccule to utricle ratio inversion (SURI) in MD patients. We calculated the sensitivity, specificity and positive/negative predictive values of each MRI examination, taking the clinical examination as the gold standard.

	3D-FLAIR VISTA	3D-FLAIR BRAINVIEW
FOV	200 x 200	200 x 200
Acquisition voxel size (mm)	0.8 x 0.8 x 0.4	0.8 x 0.8 x 0.4
Reconstruction voxel size (mm)	0.4 x 0.4 x 0.4	0.4 x 0.4 x 0.4
SENSE factor	2.5	2.5
Number of slices	90	50
Orientation	Axial	Axial
TE (ms)	316	345
TR (ms)	8000	7600
TI (ms)	2400	2300
TSE echo spacing / shot (ms)	5.1 / 586	5.9 / 642
T2 prep	TE = 125 ms	TE = 125 ms
Water Fat Shift (pix) / BW (Hz)	0.969 / 448	1.226 / 354.3
Scan time	8'40"	9'14"

TABLE 1.1 – Comparison between 3D-FLAIR VISTA® and 3D-FLAIR BRAINVIEW® acquisition parameters. A crucial step for inner ear structures precise anatomy is the optimization of the sequence for specific tissues properties. We have to manually set T1 and T2 parameters for inner ear but further studies should be performed to determine these values for healthy volunteers and patients, extracted from Attyé et al. [19]

Third study, published in Journal of Neuroradiology 2017 [20]

Besides 3D-FLAIR acquisitions, we have intended to explore whether the hydrops diagnosis vary with the TI of the MRI sequence, particularly the ratio between endolymphatic and perilym-

phatic fluids. We have raised the hypothesis that previously published discrepancies in EH rate for MD patients were influenced by the TI value. Indeed, the semi-quantitative grading system relies on a ratio between endolymph and perilymph liquids, as evaluated by drawing region of interest on axial slices [16]. The patients were considered as having vestibular hydrops when the endolymph occupies more than 50% of the vestibule area. In this classification, cochlear hydrops was diagnosed when the endolymphatic duct presented with a nodular dilatation, implying a displacement of the Reissner's membrane.

To explore the TI influence, we have performed two 3D-FLAIR sequences with two different TI values (2300ms and 2400ms) in 6 MD patients in comparison with 6 healthy volunteers. The main outcome was to evaluate the variation of the endolymph to perilymph area ratio with the two MRI sequences.

Fourth study, published in Diagnostic and Interventional Imaging 2018 [21]

Finally, we have intended to study the role of the contrast media molecule in the perilymphatic spaces' enhancement. It is well known that the physiochemical properties of gadolinium-based contrast agents are determining factors to cross the round window after intratympanic administration [13]. We have hypothesized that the passage of the blood-labyrinth barrier also depends on biochemical properties of contrast agents. We have conducted a study comparing the degree of enhancement of the perilymph obtained with two different macrocyclic gadolinium-based contrast agents (gadobutrol and gadoterate meglumine) in MD patients.

A 5 mm2 circular ROI was set in the basal turn of the cochlea and a 50 mm2 circular ROI was set at the same level in the medulla. The signal intensity ratio (SIR) was defined as the signal intensity of the basal turn divided by that of the medulla. The SIR was measured 3 times and the average SIR value was calculated for each ear.

Main Results

First study, published in European Radiology 2015 [17]

Using the 3D-FLAIR VISTA® sequence, we have firstly identified a high prevalence of hydrops in the MD groups (61 out of 68 patients in the Define MD Group ; 31 out of 64 patients in the possible MD group), particularly in the cochlea, using the semi-quantitative grading system [17]. We have observed that using a coregistration and fusion method between FLAIR and Heavily-Weighted T2 sequences ; the inter reader agreement for hydrops evaluation was higher than for analyze of the 3D-FLAIR sequence alone (0.62 vs 0.72 with the fusion process). Using the previously published grading scale, we have found a high prevalence of EH in patients with recurrent vestibulopathy (clinically classified with "probable Meniere's Disease"). The lack of control group in this study was a limitation to characterize the added value of the hydrops protocol in these patients.**We have concluded that we were able to evaluate EH using single dose of contrast media 4 hours before images acquisition, based on the semi-quantitative**

grading system.

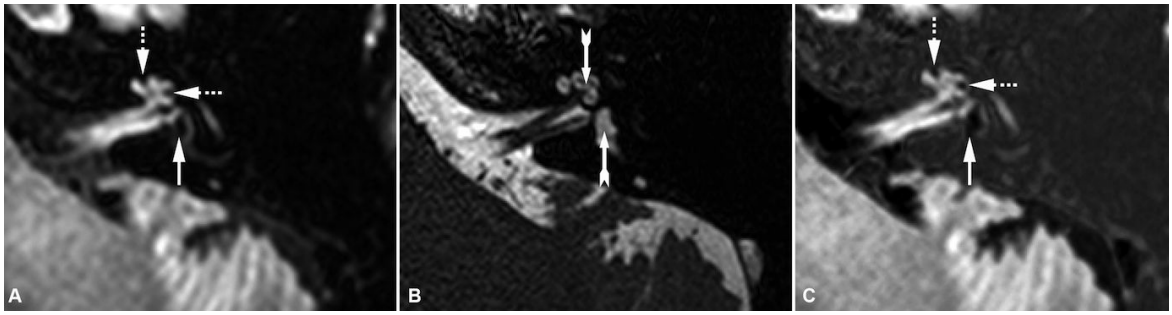

FIGURE 1.3 – **Example of the postprocessing method with fusion of the two MRI sequences**. Heavily-Weighted T2 sequence (B) was subtracted from 3D-FLAIR sequence (A) to achieve the sequence used to highlight endolymphatic hydrops (C) leading to a decrease in the temporal bone signal around the inner ear structures. As described in the text, CH (dotted arrows) was more easily separated from adjacent bone on the C image and appeared as a nodular dilatation of the endolymphatic canal. T2 sequence (B) didn't allow the distinction between perilymph and endolymph fluids (arrows).

Second study, published in European Radiology 2017 [18]

In this study [18], direct analysis (without postprocessing method) using the 3D-FLAIR Philips View®, showed variable inter-reader agreement for detecting EH using the semi-quantitative grading system (between 0.63 and 0.80, depending on the hydrops grade). Moreover, we showed no significant difference regarding the number of subjects with EH between 30 healthy volunteers and 30 MD patients using the semi-quantitative method of grading.

We have then demonstrated that systematic differentiation between utricles and saccules in all subjects was possible with the 3D-FLAIR Philips View® sequence (Figure 1.4). **We have further proposed a new classification for grading the hydrops disease in the saccule, named the SURI sign, ie. Saccule to Utricle Ratio Inversion (Figure 1.5).** In our cohorts, the SURI sign was estimated as having 100% and 50% specificity and sensitivity respectively. This scoring system has a perfect inter-reader agreement, yet has to be challenged to other MD diagnostic tests.

Third study, published in the Journal of Neuroradiology 2017 [20]

In this technical note, we have demonstrated that the endolymph to perilymph liquid ratio variation led to major differences in grading and locating hydrops with the semi-quantitative grading system (Figure 1.6). With the 2300 ms sequence, all patients and 5 out of 6 healthy volunteers presented with at least one hydrops location, either in the cochlea or the vestibule. Six out of 6 patients and 3 out of 6 volunteers displayed bilateral hydrops. With the 2400 ms sequence, 2 out of 6 healthy volunteers and 6 out of 6 patients presented with

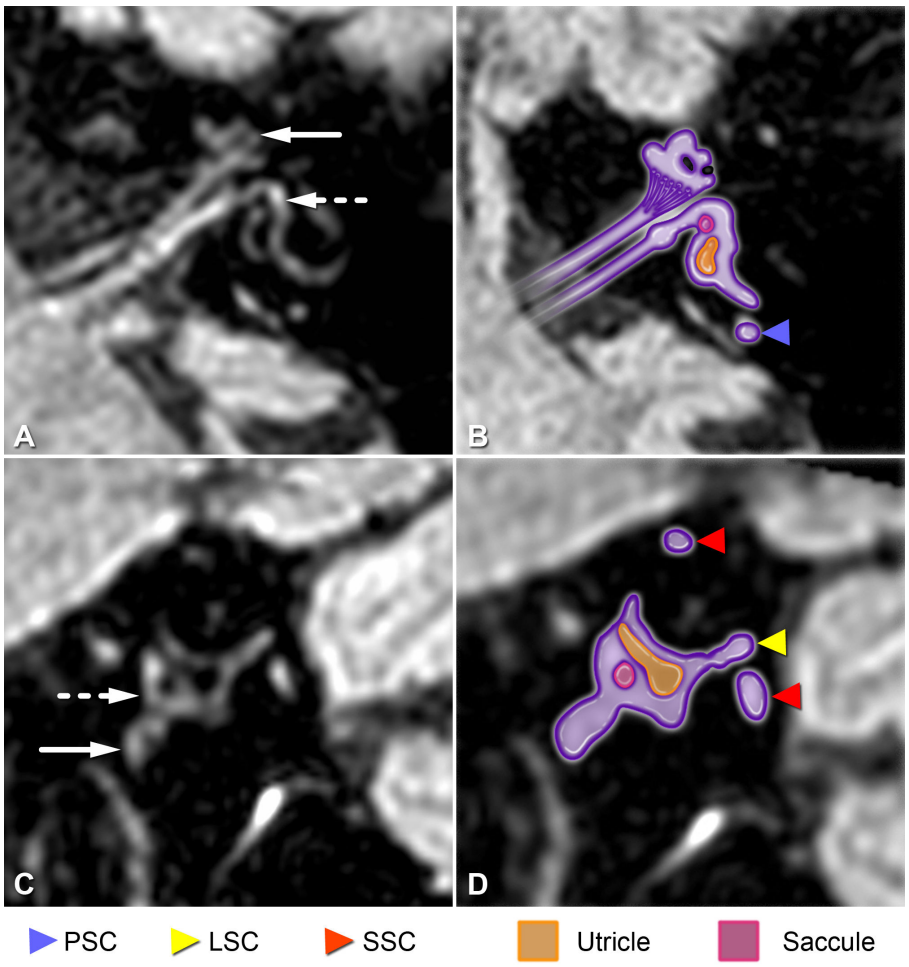

FIGURE 1.4 – **Normal inner ear radioanatomy on axial slice through the inferior part of the vestibule and sagittal reference slice in a healthy subject**. PSC : Posterior semicircular canal. LSC : Lateral semicircular canal. SSC : Superior semicircular canal. White arrow : cochlea. Dotted arrow : vestibule.

at least one hydrops location, either in the cochlea or the vestibule. By contrast, the SURI grading system was less influenced with the TI setting due to the use of the utricle as an anatomical landmark to diagnose saccular hydrops.

We would mention that the effect of raising the TI would probably increase the global fluid signal, for example in the cerebrospinal spaces. Yet, this is not sufficient to explain the local variation of the inner ear fluids in our study, also previously reported by Bykowski et al.[22]. Previous authors suggested that the variability in endolymph/perilymph contrast could be related to variable uptake of gadolinium into the perilymph [23]. We further raise the hypothesis that high TI values modified the endolymph to perilymph ratio due to close protein and ionic concentration of the two inner ear liquids, despite the known differences in composition.

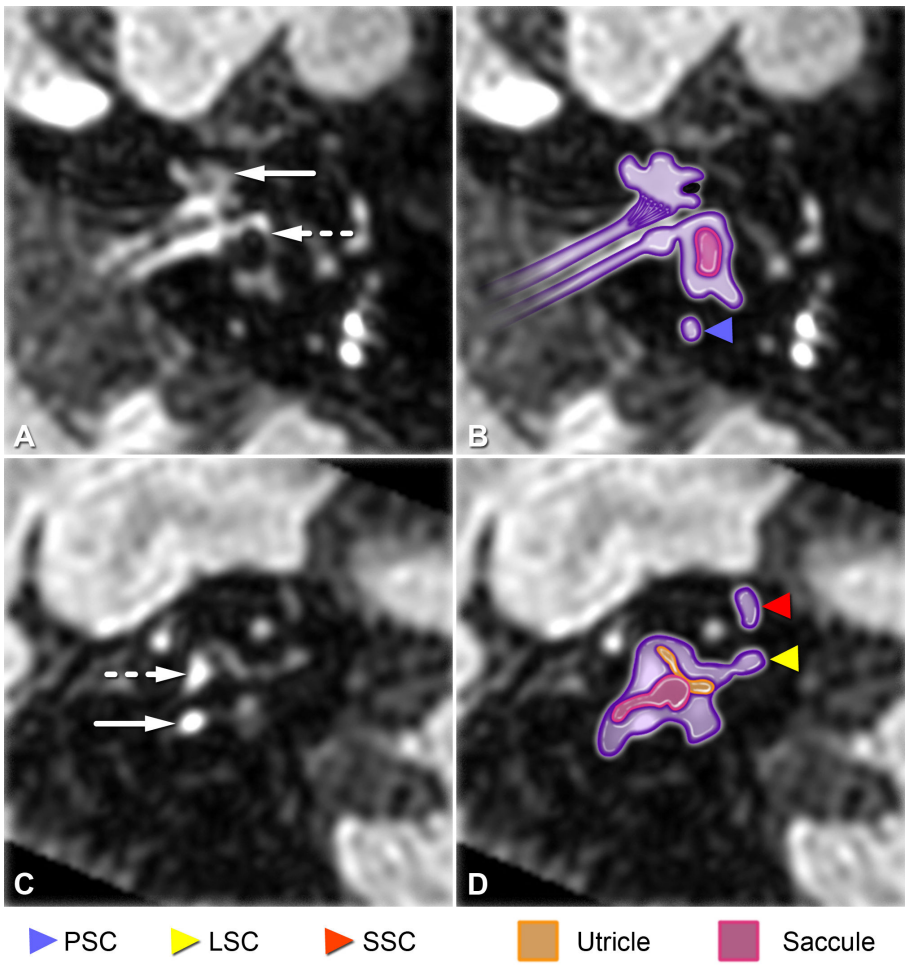

FIGURE 1.5 – **SURI ranking score illustrations on axial slice through the inferior part of the vestibule and sagittal reference slice in a MD patient with saccular hydrops**. PSC : Posterior semicircular canal. LSC : Lateral semicircular canal. SSC : Superior semicircular canal. White arrow : cochlea. Dotted arrow : vestibule.

Fourth study, published in Diagnostic and Interventional Imaging 2018 [21]

The quantitative evaluation of the inner ear contrast enhancement demonstrated similar Signal Intensity Ratio between Gadobutrol (median ratio : 1.58) and Gadoterate Meglumine (median ratio : 1.3) in the symptomatic ears of MD patients. The Signal Intensity Ratio of the contralateral ears was significantly greater with Gadobutrol (median : 1.62) than with Gadoterate Meglumine (median : 1.21, p= 0.009)(Figure 1.7).

Importantly, Gadobutrol provides better anatomical details (distinction between utricle and saccule) regarding endolymphatic space and semicircular canals of asymptomatic ear. We hypothesize that Gadobutrol is superior to gadoterate meglumine in the assessment of endolymphatic space because of different concentration and longitudinal relaxivity,

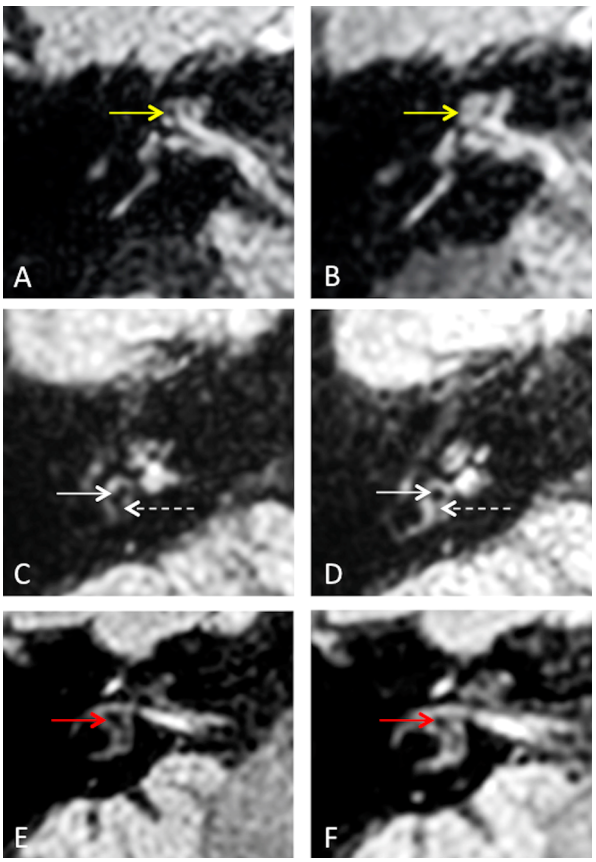

FIGURE 1.6 – **Inner ear structures with the 2300ms sequence (A, C and E) in comparison with the 2400ms sequence (B, D and F)**. A-B : Example of cochlear hydrops in a MD patient : nodular obstruction of the scala vestibuli was seen with the 2300ms sequence (A, yellow arrow). In the same patient and MRI session, the cochlear duct was no longer visible, with the 2400ms sequence (B, yellow arrow). C-D : Saccular hydrops in a right MD patient. Both endolymphatic structures decreased in terms of surface from the 2300ms sequence (C) to the 2400ms sequence (D). E-F : Right inner ear structures in a healthy volunteer. E : The utricle is large with the 2300ms sequence, and would correspond to vestibular hydrops, as defined by Nakashima et al. [5] On the 2400ms sequence, the endolymphatic fluid occupied less than one third of the vestibular surface.

which are determining factors to cross the blood-perilymph barrier.

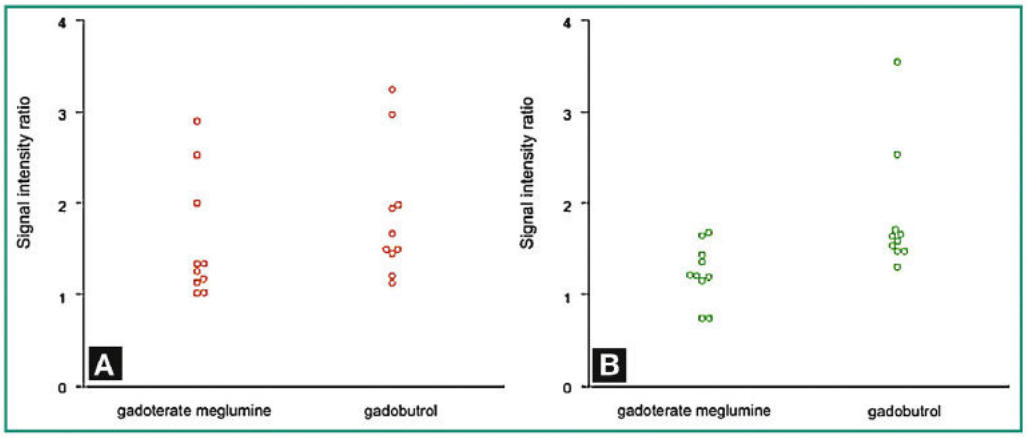

FIGURE 1.7 – **Diagrams show signal intensity ratio (SIR) in the symptomatic (A) and the asymptomatic ear (B) in 10 patients who received gadoterate meglumine and 10 patients who received gadobutrol**

.

Limitations

The main problem we encountered was the impossibility to correlate the presence of EH by imaging with pathological analysis in vivo. Therefore, we calculated the specificity and sensibility of MRI based on the presence of clinical MD instead of on a histopathological analysis of endolymph quantity and distribution. The absence of longitudinal studies or test-retest procedure is also problematic to confirm the reproducibility of 3D-FLAIR sequences acquisition and analysis. We could also mention that EH method of visualization was qualitative or semi-quantitative, rather than quantitative. The absence of scientific publication using T1 mapping and T2 mapping to provide measures of the relaxation time of both inner ear compartment was another limitation. For contrast media effect evaluation on the perilymph enhancement, we did not compare the two gadolinium-based contrast agents in the same patients for ethical consideration.

Further results, figures and details can be found in the following papers :

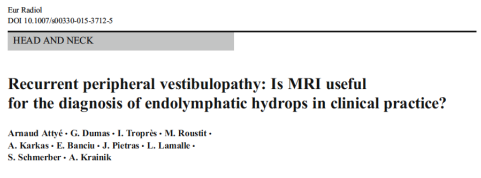
Eur Radiol
DOI 10.1007/s00330-015-3712-5

HEAD AND NECK

Recurrent peripheral vestibulopathy: Is MRI useful for the diagnosis of endolymphatic hydrops in clinical practice?

Arnaud Attyé · G. Dumas · I. Troprès · M. Roustit · A. Karkas · E. Banciu · J. Pietras · L. Lamalle · S. Schmerber · A. Krainik

FIGURE 1.8 – **European Radiology, Rank B, Impact Factor 4.027, Number of citations (Scopus, October the 1st 2018) : 19**

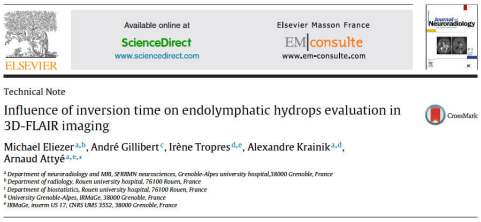
Available online at ScienceDirect www.sciencedirect.com

Elsevier Masson France EM|consulte www.em-consulte.com

Technical Note

Influence of inversion time on endolymphatic hydrops evaluation in 3D-FLAIR imaging

Michael Eliezer, André Gillibert, Irène Tropres, Alexandre Krainik, Arnaud Attyé

FIGURE 1.9 – **Journal of Neuroradiology, Rank C, Impact Factor 2.706, Number of citations (Scopus, October the 1st 2018) : 4**

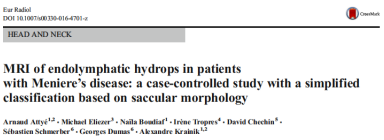
Eur Radiol
DOI 10.1007/s00330-016-4701-z

HEAD AND NECK

MRI of endolymphatic hydrops in patients with Meniere's disease: a case-controlled study with a simplified classification based on saccular morphology

Arnaud Attyé · Michael Eliezer · Naïla Boudiaf · Irène Tropres · David Chechin · Sébastien Schmerber · Georges Dumas · Alexandre Krainik

FIGURE 1.10 – **European Radiology, Rank B, Impact Factor 4.027, Number of citations (Scopus, October the 1st 2018) : 11**

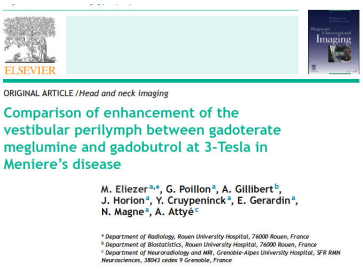
ELSEVIER

ORIGINAL ARTICLE / Head and neck imaging

Comparison of enhancement of the vestibular perilymph between gadoterate meglumine and gadobutrol at 3-Tesla in Meniere's disease

M. Eliezer, G. Poillon, A. Gillibert, J. Horion, Y. Cruypeninck, E. Gerardin, N. Magne, A. Attyé

FIGURE 1.11 – **Diagnostic and Interventional Imaging, Rank C, Impact Factor 2.115, Number of citations (Scopus, October the 1st 2018) : 0**

1.3 Saccular hydrops : the biomarker of low-tone sensorineural hearing loss

Rationale

In the semi-quantitative grading system for hydrops evaluation, the utricle and saccule were not individually assessed. However, 3D images of the membranous labyrinth directly reconstructed from temporal bone sections suggest that in EH changes in saccular morphology are more sensitive than those of the utricle [8]. As we have demonstrated the variation of the endolymph to perilymph ratio with TI parameters, we have decided to use an anatomical landmark to relatively characterize the presence of saccular hydrops. Indeed, we have defined the presence of saccular hydrops by using the utricle as an anatomical landmark with the SURI score. Thus, when the TI of the MRI sequence modify the endolymph to perilymph ratio, the saccule to utricle ratio remains stable.

Definite MD clinically associates recurrent vertigo with low-tone SNHL, and either tinnitus or aural fullness. Regardless of the involved molecular mechanisms, the episodes of vertigo have a higher frequency in the first 5 years of the disease, while the hearing loss usually progress during the first 5-10 years [24]. It is now crucial to understand whether saccular hydrops is linked to vertigo, hearing loss or both because for patients who continue to have frequent major episodes of dizziness despite adequate medical treatment, invasive endolymphatic sac surgery is used worldwide to shunt the excess of endolymph liquid in the saccule. We have tested the hypothesis that saccular hydrops is more specific to the degree of SNHL than to vertigo, which could explain why post-mortem studies overestimated the degree of hydrops in patients with MD, as it wasn't systematically explored until a late stage of the disease.

Over the past decades, different electrophysiological tests have been developed so as to improve MD diagnosis and therapeutic protocols. In addition to the clinical criteria, objective tests were needed to confirm this diagnosis. We can mention the electrocochleography (EcochG), which has been used for the diagnosis of EH since the 70s. It measures cochlear evoked potentials by acoustic stimulation. Cervical vestibular-evoked myogenic potential (cVEMP) corresponds to an inhibitory sacculo-collic reflex recorded in the ipsilateral sternocleidomastoid muscle in response to an acoustic stimulation. Distended saccule, with contact to stapes footplate, enhances the saccular macula sensitivity to loud sound, resulting in abnormal cVEMP. Finally, distortion product otoacoustic emissions (DPOAEs), generated by contractile outer hair cells of the cochlea, has been evaluated for the diagnosis of MD. Postural changes, from sitting upright (Fowler's position) to supine position, can increase intracranial pressure and therefore intracochlear pressure especially in MD patients.

We aimed at understanding whether saccular hydrops is linked to vertigo or low-tone SNHL, and to study the potential added value of MR examinations on electrophysiological tests in MD

patients.

Summarized methods

First study, published in European Radiology 2017 [25]

After having demonstrated that a SURI was present in a subset of MD patients, we have evaluated the presence of saccular hydrops using our grading method in three clinical presentations : a new cohort of 20 MD patients, 20 other patients with isolated low-tone SNHL and 20 patients with recurrent vestibulopathy. In the MD and SNHL groups, Standard pure-tone audiometry was obtained at frequencies of 125 to 8000 Hz. Pure-tone average was calculated using 500 to 4000 Hz frequencies. SNHL was ranging from normal (equal or less than 20dB), mild (21-40 dB), moderate (41-70 dB), severe (71-90 dB), and profound (more than 90 dB). Receivers operating characteristic (ROC) curves were then traced to determine the optimal hearing loss threshold to differentiate patients with saccular hydrops according to the best area under the curve (AUC).

Second study, published in Ear and Hearing 2018 [26]

Forty-one patients, with fifty affected ears including 9 bilateral cases, were included prospectively in this study, from April 2015 to April 2016, at the Otolaryngology department of Grenoble University Hospital. The purpose of the work was to compare four non-invasive methods (EcochG, shift-DPOAEs, cVEMP, MRI with the hydrops protocol) to assess MD groups, including patients with possible and Definite MD. To do this, we first prepared an “Ear” file of 50 affected ears in 41 patients including 9 bilateral cases. Chi square tests and concordance coefficient kappa were used to assess the association and the concordance, respectively, between the methods. The non-parametric test, Mann-Whitney U test was used to compare hearing loss in the group with the diagnosis of hydrops vs absence of hydrops for the different methods.

Main Results

First study, published in European Radiology 2017 [25]

We found that saccular hydrops correlates with sensorineural hearing loss level above 40 dB while vertigo patients without sensorineural hearing loss do not have saccular hydrops (Figures 1.12 and 1.13). Importantly, saccular hydrops was described in patients without clinical diagnosis of Meniere’s Disease, in subjects with isolated low-tone sensorineural hearing loss. We raise the hypothesis that the saccule plays the role of a buffer in endolymph reabsorption. When its compliance is overstretched, inner ear endolymph regulation fails, subsequently leading to cochlear lesions, as suggested by experimental animal models [2].

Second study, published in Ear and Hearing 2018 [26]

Abnormal EcochG and shift-DPOAEs in patients with Definite MD were found in 68% and 64.5%, respectively. In Definite MD group, 25.7% had a positive MRI. The correlation between MRI

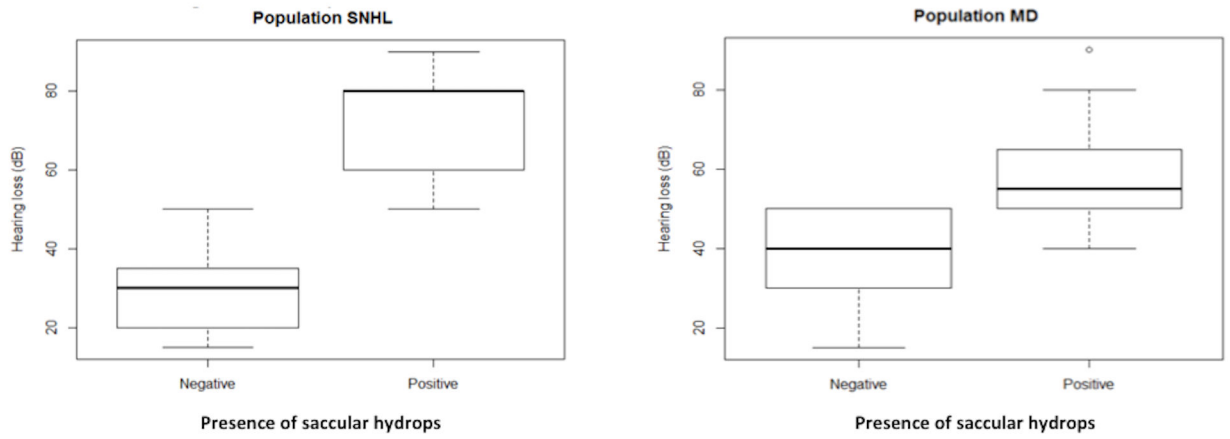

FIGURE 1.12 – **Charts with correlation between hearing loss (dB) and the presence by MRI of saccular hydrops, in SNHL patients and MD patients.**

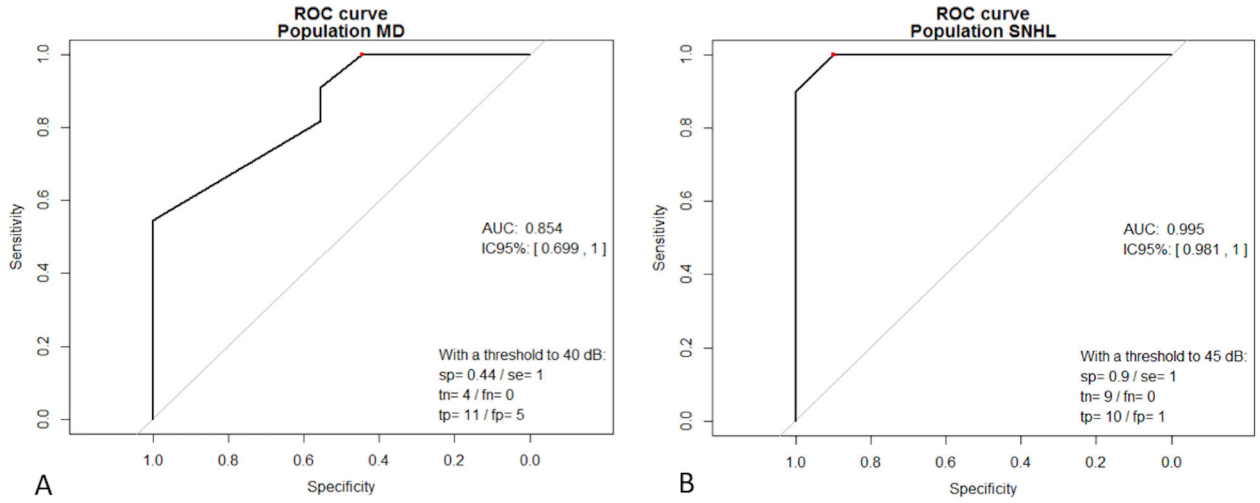

FIGURE 1.13 – **Receiver operating characteristic (ROC) curve analyses of hearing loss level**. It determine the optimal hearing loss threshold (independent variable) to differentiate patients with saccular hydrops (dependent variable).

versus EcochG and MRI versus shift-DPOAEs was not significant. 22.9% of Definite MD group had positive cVEMP. We concluded that EcochG and shift-DPOAEs were both well correlated with clinical criteria of Meniere's disease. while MRI hydrops detection was only correlated with a hearing loss loss level up to 35 dB. The shift-DPOAEs presented the advantage of a rapid and easy measurement if DPOAEs could be recorded (i.e. hearing threshold inferior to 60dB). In contrast, EcochG can be performed regardless of hearing loss. In combination with shift-DPOAEs, it enhances the chances to confirm the diagnosis with a better confidence.**The combination of**

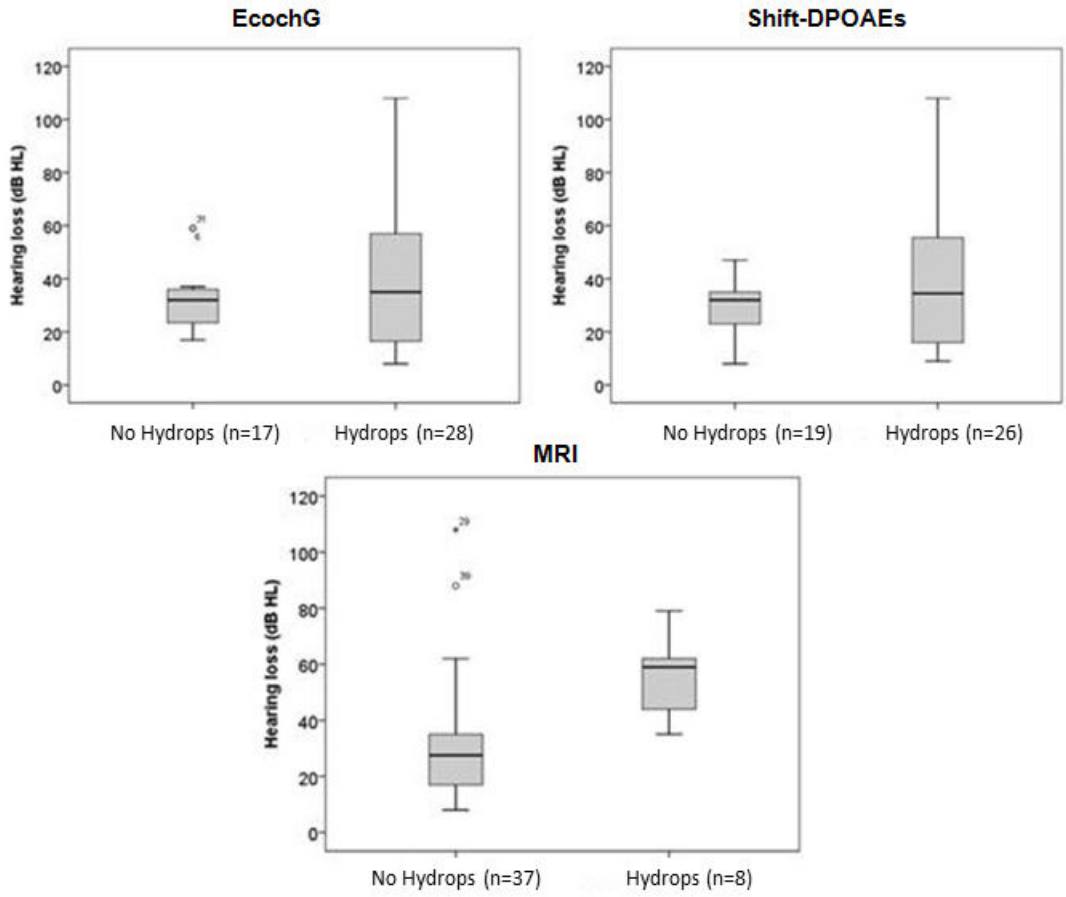

FIGURE 1.14 – **Boxplot of comparative methods depending on hearing loss.**

these methods improves the MD diagnosis (Figure 1.14).

Limitations

We have excluded the cochlear endolymphatic compartment from inner ear analysis because in contrast to saccular dilatation, imaging in healthy subjects often revealed cochlear duct dilatation, rendering it difficult to distinguish the pathological condition based on this criterion, especially without post processing method. It cannot be excluded that MD begins with only a subtle increase in the size of the endolymphatic cochlear compartment that may be impossible to distinguish with high specificity from a normal condition with 3D-FLAIR sequences. Since the hearing loss degree usually progress in the first 5 to 10 years of MD, further studies comparing the presence of saccular hydrops with the duration of the disease are important. We should mention that the distinction between utricle and saccule structures has only been described using a Philips 3T scanner and that controversies remain about the possibility to distinguish the two structures in more advanced cases of MD. In previous pathological and imaging studies, the

abnormal utricle expansion was mainly described into the lateral semicircular canal rather than into the inferior part of the vestibule, thus one can consider that a close contact between utricle and saccule in the vestibule is mainly due to saccular superior displacement.

Further results, figures and details can be found in the following papers :

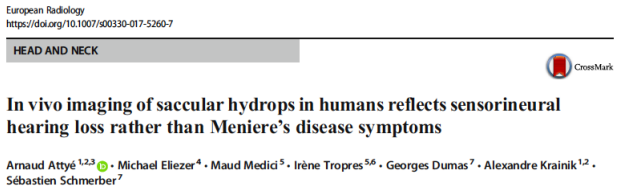
European Radiology
https://doi.org/10.1007/s00330-017-5260-7

HEAD AND NECK

In vivo imaging of saccular hydrops in humans reflects sensorineural hearing loss rather than Meniere's disease symptoms

Arnaud Attyé [1,2,3] · Michael Eliezer [4] · Maud Medici [5] · Irène Tropres [5,6] · Georges Dumas [7] · Alexandre Krainik [1,2] · Sébastien Schmerber [7]

FIGURE 1.15 – **European Radiology, Rank B, Impact Factor 4.027, Number of citations (Scopus, October the 1st 2018) : 2**

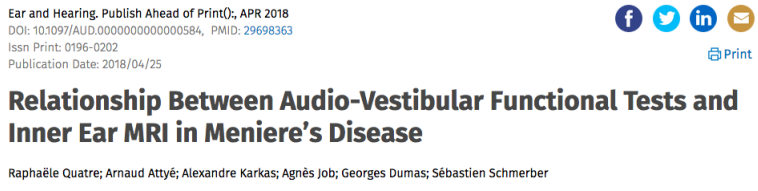
Ear and Hearing. Publish Ahead of Print(), APR 2018
DOI: 10.1097/AUD.0000000000000584, PMID: 29698363
Issn Print: 0196-0202
Publication Date: 2018/04/25

Print

Relationship Between Audio-Vestibular Functional Tests and Inner Ear MRI in Meniere's Disease

Raphaële Quatre; Arnaud Attyé; Alexandre Karkas; Agnès Job; Georges Dumas; Sébastien Schmerber

FIGURE 1.16 – **Ear and Hearing, Rank A, Impact Factor 3.12, Number of citations (Scopus, October the 1st 2018) : 1**

1.4 The bicompartmental model for endolymph circulation

1.4.1 The vestibular aqueduct sign : Magnetic Resonance Imaging can detect abnormalities in both ears of patients with unilateral Meniere's Disease.

Scientific article, in press in the *Journal of Neuroradiology*.

Authors : Arnaud Attyé, Marion Barma, Sébastien Schmerber, Georges Dumas, Michael Eliezer, Alexandre Krainik

Rationale

The inner ear pressure regulation relies on three communication routes between the intracranial space and the inner ear : the vestibular aqueduct, the cochlear aqueduct and the internal auditory canal. The endolymph is mainly produced from the cerebrospinal fluid [27]. Recently a new system, the "glymphatic system" was described which cleans up macroscopic waste produced by central nervous system activity [28]. The disruption of this system might be a marker of endolymphatic hydrops with endolymph fluid homeostasis and volume depending on the quality of CSF cleaning.

It has been suggested that no CSF transport occurs in the human cochlear aqueduct. By contrast, previous histological studies have demonstrated atrophy of the endolymphatic sac, hypoplasia of the vestibular aqueduct (VA) and narrowing of the lumen of the endolymphatic duct in MD patients [29, 30]. Waste accumulation for CSF cleaning could lead to ion transport disorders and favor [Ca2+] augmentation in the endolymph, leading to calcification and eventually ossification of the VA. Such findings have been highlighted with 2D computed tomography, 3D-Cone beam CT and with MRI [31, 32] describing a correlation between the lack of a visible endolymphatic duct and the clinical course of MD. One hypothesis to explain VA modification relies on calcium ion (Ca2+) augmentation in hydropic ears, as demonstrated in biological samples [33]. No previous study has assessed the relationship between VA abnormalities and EH findings in living humans.

We aimed at studying vestibular aqueduct alteration in MD patients using 3D-FLAIR sequences with delayed acquisitions.

Summarized methods

We have performed a case-controlled study to obtain an overview of the normal vestibular aqueduct appearance on 3D-FLAIR sequences in healthy subjects and also to compare saccular hydrops imaging with variations in VA morphology. We have raised the hypothesis that VA abnormalities can be detected in the inner ear of patients with MD in the absence of saccular hydrops. Twenty consecutive patients with a definite clinical diagnosis of unilateral MD based

on the latest AAO-HNS guidelines and twenty healthy volunteers with no history of inner ear disorders were recruited between August 2015 and April 2018. The presence of the vestibular aqueduct ; a linear duct starting from the posterior edge of the temporal bone to the vestibule, was visually evaluated on two 3D-FLAIR View sequences (non-enhanced and 4 hours after contrast media injection) with a three-level ranking system as illustrated on the provided Figure 1.17. Besides evaluating the VA, we determined the presence of saccular hydrops, defined as a ratio equal or up to 1 between the area of the saccule and the area of the utricle (SURI). We have evaluated the inter-reader agreement in evaluating both the VA appearance and Hydrops grading with the SURI method.

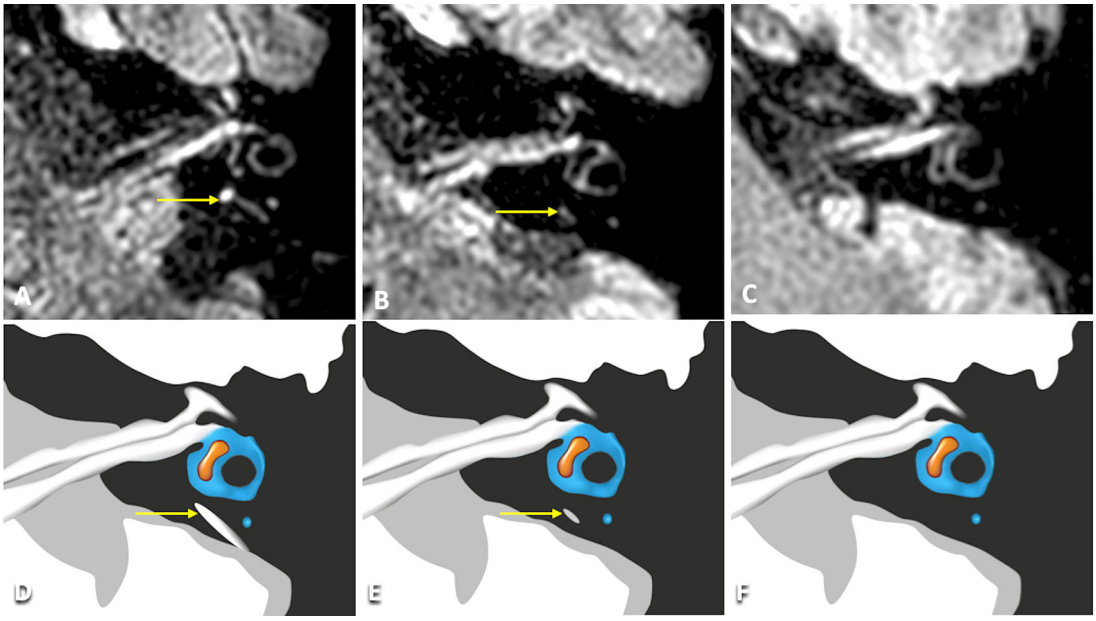

FIGURE 1.17 – **Vestibular Aqueduct Grading Score.** A-D : Grade 0 in a healthy volunteer with a normal VA (yellow arrow). The presence the vestibular aqueduct was confirmed with a linear duct starting from the posterior edge of the temporal bone to the vestibule. The absence of a visible VA just before the vestibule structure was not taken into account due to the perichondrial tissue. B-E : Grade 1 in a MD patient with a discontinuous VA (yellow arrow). It is interesting to mention that the presumed partial ossification was located at the posterior part of the VA, directly connected to the endolymphatic sac. C-F : Grade 2 in a MD patient with complete absence of visible VA.

Main Results

In controls and patients, VA modifications were symmetrical without significant difference between the symptomatic and asymptomatic ears. The presence of at least one ear with discontinuous VA showed a correlation with clinical MD ($p<0.001$) with a sensitivity of 90%. Ten patients had saccular hydrops, but only in the symptomatic ears. The evaluation of VA did not differ between MRI, both within MRI series or between the two radiologists (kappa without and

with contrast agent=0.9 and 0.92 respectively). **Analysis of the vestibular aqueduct by MRI detects abnormalities in both ears of patients with unilateral MD**. Due to the difference in negative predictive value between ossification of the VA and the presence of saccular hydrops, 23% of MD patients could have saccular hydrops with a VA of normal appearance. This could be explained either by a different physiopathological mechanism, or by calcification that is too subtle to be detected by the MRI procedure. Recent developments in CBCT and CT with iterative reconstructions are promising and less onerous techniques to display subtle variations in VA osseous morphology. An evaluation of the state of the VA could become a complimentary factor to support the diagnosis of MD because of its high sensitivity.

Limitations

We hypothesize that VA modifications occur earlier than saccular hydrops and more generally before the development of endolymphatic hydrops, yet because of the design of this study we cannot confirm this assumption. It should therefore be considered as a preliminary study, which should be followed by longitudinal studies. The absence of utricular and cochlear location description for hydrops is also a limitation of this study, particularly with regards to the previous theory of Pender [8], which has described a cochlear distribution of the hydrops disease, successively encompassing the cochlea, the saccule, the utricle and the semicircular canal ampullae.

1.4.2 Sensorineural hearing loss in patients with vestibular schwannoma relies on the presence of utricular hydrops, as diagnosed with heavily weighted T2 sequences

Scientific article, *under submission*

Authors : Michael Eliezer, Guillaume Poillon, André Gillibert, Charles Maquet, Julien Horion, Jean-Paul Marie, Adrien Trintignac, Nicolas Magne, Arnaud Attyé

The origin of cochlear and vestibular symptoms in patients with vestibular schwannoma (VS) is uncertain and various mechanisms related to cochlear dysfunction have been speculated including endolymphatic hydrops (EH) [10] Currently, MRI is the imaging technique of choice for the diagnosis of VS and EH using inversion recovery sequences [18, 34]. Previously, labyrinthine tap, an invasive method consisting in a platinotomy in order to obtain a sample of perilymphatic fluid, demonstrated that in patients with VS, protein levels were 5 to 15 times higher than in healthy subjects [35]. Nevertheless, two studies have also reported a precipitate in the endolymphatic space related to the high protein content [9].

3D-FLAIR sequences allow the visualization of subtle compositional changes of the inner ear fluids in various diseases related to hemorrhage and increased protein levels. Kim et al. have demonstrated that the increased cochlear signal on 3D-FLAIR images was correlated with the degree of hearing loss, as measured by the PTA [36]. Lee et al. were the first to suggest that

the high signal seen in the vestibule with 3D-FLAIR sequences in VS patients was related to the well-known high protein concentrations in the perilymph, while the endolymph (utricle and saccule) appeared as dark signal intensity. Based on this condition, Naganawa et al. [37] assessed the rate of EH in patients with VS on non-contrast 3D-FLAIR images and found no correlation between EH and vertigo. However, they did not assess the correlation between EH and the degree of sensorineural hearing loss. Recently, fast imaging employing steady-state acquisition with cycle phase (FIESTA-C, General Electrics®) sequence demonstrated a significant decrease of perilymphatic signal intensity in patients with vestibular VS compared to patients with cerebellopontine angle meningiomas [38]. It has also been reported that only the perilymphatic signal decreased on FIESTA-C sequence, due to the elevated perilymphatic protein content caused by the internal auditory canal tumor, allowing recognition of the utricle and saccule in the inner ear. The aim of this study was to assess whether the volume of the vestibular endolymphatic space is related to the degree of hearing loss.

Methods

Patients

Thirty-two patients were recruited between December 2015 and May 2017. The study protocol was approved by our institutional review board (IRB E2017-23). All of the patients were recruited on the basis of typical imaging findings for VS : “ice cream cone” shape tumor centered on the internal auditory canal on the cochleovestibular nerve, presenting with a relatively high-signal on T2-weighted sequence, a hypointense filling defect on steady-state free precession and a homogenous enhancement on post-contrast T1-weighted sequence. VS was defined as non-obstructive when cerebrospinal fluid was present between the tumor and the internal auditory canal. It was defined as obstructive when the tumor completely obstructed the internal auditory canal without cerebrospinal fluid around. Patients with a history of gamma knife radiosurgery or surgery were excluded based on the supplemental risk of post-treatment hearing loss. Nine patients (28%) were excluded from the analysis : 6 patients had no significant decrease in perilymphatic signal on FIESTA-C, hence not allowing differentiation between the high signal of the endolymph and the low signal of the perilymph (Fig. 1.18). The 3 other excluded patients had both perilymphatic and endolymphatic signal decrease, thus the volume of the endolymphatic space could not be performed.

Audiometric tests

The pure-tone average (PTA) hearing levels of bone conduction were calculated as the mean of the hearing levels measured at 500, 1000, 2000, and 4000 Hz. Patients’ hearing was classified as mild (26-40 dB), moderate (41-60 dB), severe (61-80 dB) and profound (over 81 dB). Speech Recognition Threshold (SRT) was defined as the minimum hearing level for speech at which an individual can recognize 50% of the speech material [18]. For the purpose of data analysis, complete

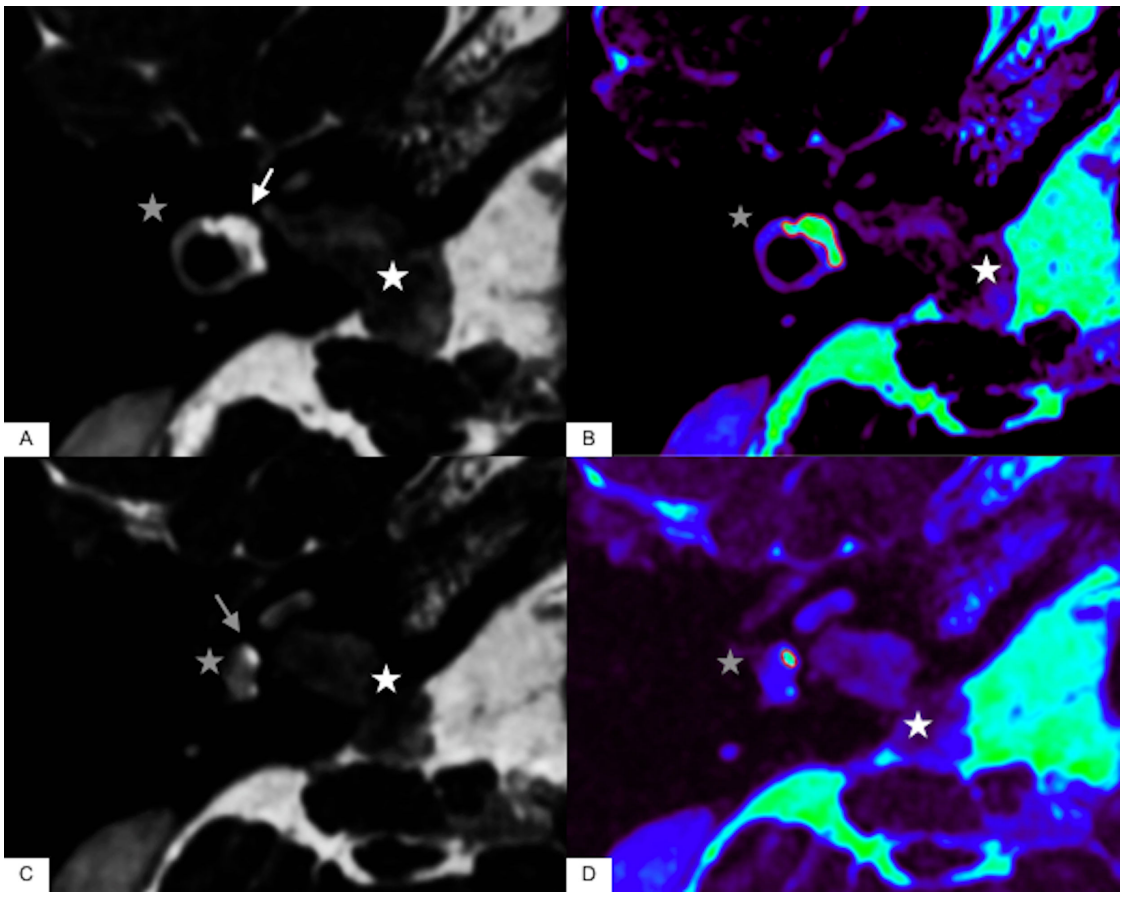

FIGURE 1.18 – **Differentiation between the high signal of the endolymph and the low signal of the perilymph on heavily-weighted T2 sequences** A-B : axial slices at the level of the utricle. (A) FIESTA-C sequence showing a patient with a right intracanalicular schwannoma (white asterisk) and the utricle as a high signal (white arrow) while the perilymph from the vestibule and the lateral semicircular canal remains as a low signal (gray asterisk). (B) FIESTA-C sequence with the rainbow-scale on color map showing the utricle as a green signal and the perilymph (gray asterisk) as a blue signal and demonstrating the manual segmentation for the utricle in order to measure the volume. C-D : axial slices at the level of the saccule. (C) FIESTA-C sequence on the same patient showing the saccule (gray arrow) as a high signal contrasting with the low signal of the perilymph from the vestibule (gray asterisk). (D) FIESTA-C sequence with the rainbow-scale on color map showing the saccule as a green signal and the perilymph (gray asterisk) as a blue signal and demonstrating the manual segmentation for the saccule in order to measure the volume.

absence of response was assigned a value of 120 dB for PTA and for speech discrimination.

Imaging

All patients had an MRI scan before and after intravenous administration of contrast media. Imaging examinations were carried out on a General Electric Discovery MRI 750® (2012, General Electric Medical Systems, Milwaukee, USA) with a 16-channel head-neck-spine coil. We performed

FIESTA-C sequences before contrast administration. Axial spin-echo T1-weighted images were acquired after a single intravenous dose of Gadobutrol, Gadovist® (Bayer Healthcare, Gd-BT-DO3A, 0.1 mmol/kg). Steady-state free procession sequence such as FIESTA-C sequence is a refocused steady-state gradient echo sequence that provides high signals from tissues with elevated T2/T1 ratios and an excellent spatial resolution. The FIESTA-C sequence was performed in the plane of the lateral semicircular canal with the following parameters : TR : 7 ms, TE : 2.8 ms, NEX : 1, matrix : 484x484, flip angle : 60°, bandwidth : 83.3 kHz, 0.3 mm slice thickness covering the labyrinth with a 20 cm field of view. We employed the ARC parallel imaging technique with an acceleration factor of 2 and a scan time of 4 minutes and 40 seconds. The Axial spin-echo T1-weighted sequence was performed with the following parameters : TR : 580 ms, TE : 19 ms, NEX : 2, spacing between slices : 1.7 mm, matrix : 416x288, 1.5 mm slice thickness covering the labyrinth with a 16.5 cm field of view.

Visualization of the vestibular endolymphatic space The presence of the following structures was verified on the FIESTA-C sequence : - The saccule : The saccule appears as a high signal area located on the medial and anterior wall of the vestibule, underneath the level of the lateral semicircular canal. - The utricle : The utricle appears as a high signal elliptical zone that occupies the superior part of the vestibule, at the level of the lateral semicircular canal.

Tumor volume and vestibular endolymphatic space volume measurements

The images for each patient were evaluated independently by two radiologists specialized in head and neck imaging (ME and GP) with 6 years and 2 years of experience in hydrops imaging respectively, blinded to the clinical data, both with added certification in head and neck imaging, blinded to the clinical data. The imaging data of inner ears were analyzed with General Electric workstation® (ADW 4.6). We used the region of interest method with manual segmentation, drawing the surface of the utricle and saccule on axial FIESTA-C slices using the color map with the rainbow scale providing a high-contrast between the endolymph, the perilymph and the surrounding bone. The software then calculated the volume of the utricule, the saccule and of the entire vestibular endolymphatic spaces. We applied the same method to measure the schwannoma volume. We also recorded whether each schwannoma obstructed the inner auditory canal. Volumetric analysis was expressed in cubic centimeters for the schwannoma and in cubic millimeters for the vestibular endolymphatic space.

Statistical analysis

Data were analyzed using SPSS software v22.0 (IBM, New York, USA). To evaluate the reproducibility of the volume by the two observers the Intraclass Coefficient Correlation (ICC) was used. ICC values less than 0.5 are indicative of poor reliability, values between 0.5 and 0.75 indicate moderate reliability, values between 0.75 and 0.9 indicate good reliability, and values greater than 0.90 indicate excellent reliability. The mean absolute deviations between the two radiologists for the saccular, utricular and vestibular endolymphatic volumes were estimated.

We consider as adequate for volume estimations a range of deviation of 10% between measures. A paired Student's t test was used to compare the degree of hearing loss in symptomatic and asymptomatic ears in patients with VS. Pearson test, Spearman test and Brunner-Munzel test were used for categorical data to explore the correlation between the volume of the schwannoma, the volume of the vestibular endolymphatic space and the degree of hearing loss. For the purpose of the study, the volumes evaluated by the most experienced radiologist were taken as reference values in order to explore the correlation with the audiometric results. We set the significance threshold (p-values) at 0.05.

Results

Population

Twenty-three patients were included in this study (13 women, 10 men) with a median age of 63.5 ranging from 49 to 88 years. The patients had unilateral schwannoma, which was confirmed by MRI : 13 patients had a tumor on the right side and 10 on the left side.

MRI data

The tumor volume average of the included patients (n=23) wasestimated as being 1.74± 2.5 cm3 (0.1 to 11.6 cm3). All these patients presented with obstructive schwannoma. The tumor volume average of the excluded patients wasestimated as being 0.14± 0.22cm3 for the patients with no perilymphatic signal decrease (n=6). These 6 patients referred with non-obstructive inner auditory canal tumors.

The 3 patients who were excluded due to the endolymphatic signal decrease (added to perilymphatic signal decrease, thus rendering impossible the distinction between endolymph and perilymph fluids) presented with tumor volume average estimated as 2.30± 1.9cm3, all with obstructive schwannomas. In the included patients, the mean saccular volume was 3.17± 1.1 mm3 (ranging from 1.45 to 5.7 mm3) while the mean utricular volume was 14.4± 5 mm3 (6.6 to 23.9 mm3). The mean volume of the vestibular endolymphatic space was 17.45± 5.5 mm3 (8.3 to 25.4 mm3). The ICC (Fig. 1.19) for the saccular, utricular and vestibular endolymphatic volumes were estimated respectively at 0.867, 0.966 and 0.967. The mean absolute deviations between the two radiologists for the saccular, utricular and vestibular endolymphatic volumes were 0.42 mm3 (10.5%), 1.10 mm3 (8%) and 1.03 mm3 (5.1%) respectively.

Correlation between the volume of the vestibular endolymphatic space and audiometric findings. The mean PTA level was 57.9 dB (SD±26.5 dB) on the tumor side and was significantly higher in comparison with contralateral ears 25,7 dB (SD±13.7 dB) ($p< 0.0001$). There were 5 patients with mild sensorineural hearing loss, 11 patients with moderate sensorineural hearing loss, 6 patients with severe sensorineural hearing loss and 3 patients with profound sensorineural hearing loss. SRT was available for all patients except one, ranging from 10 to 120 dB with a mean of 60.2 (SD±31) dB on the tumor side. The SRT average on contralateral side was significantly

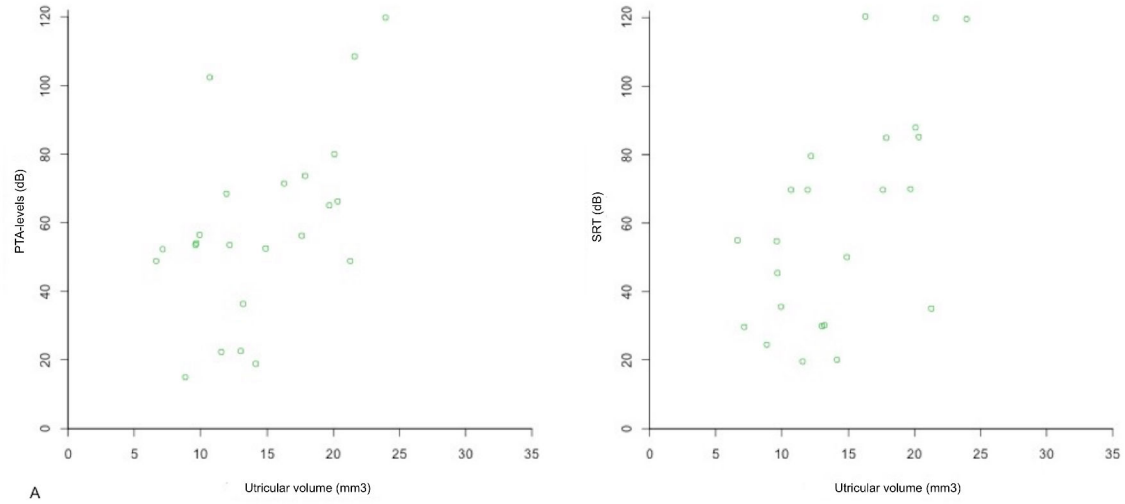

FIGURE 1.19 – **Correlation between the utricular endolymphatic space volumes and the hearing thresholds, as evaluated by PTA and SRT.** There is a significant correlation between the utricular (PTA : rho=0.5, p=0.015 ; SRT : rho=0.58, p=0.004) and the degree of hearing loss.

lower 23.7 dB (SD±13.3 dB) (p< 0.0001).

In the 6 patients excluded that presented no perilymphatic and endolymphatic signal decreased, the PTA and the SRT average were estimated as being 23.3 dB (SD±7.6 dB) and 42.5 dB (SD±25.6 dB) respectively on the symptomatic ear. In the 3 patients excluded that presented both with endolymph and perilymph signal decreased, the mean PTA and SRT averages were 38.75 dB (SD±35.7 dB) and 45 dB (SD±40.9 dB) respectively on the symptomatic ear. There was a significant correlation between the utricular volume and the degree of hearing loss (Fig. 1.20)) as evaluated with the levels of PTA (rho=0.5, CI95 0.11 ; 0.76, p=0.015) and SRT (rho=0.58, CI95 0.21 ; 0.8, p=0.004), but not significant between the saccular volume and the levels of PTA (p= 0.71) and SRT (p=0.38). There was also a significant correlation between the volume of the vestibular endolymphatic space and the degree of hearing loss as evaluated with the levels of PTA (rho=0.42, CI95 : 0.04 ; 0.70, p=0.032) and SRT (rho=0.55, CI95 : 0.20 ; 0.77, p=0.004).

Correlation between the tumor volume and audiometric findings No significant correlation was observed between tumor volumes and PTA levels (Rho= 0.20, CI95 -0.20 ; 0.54, p=0.33) and SRT (Rho= 0.22 CI95 -0.18 ; 0.56, p=0.28).

Discussion

We demonstrated that the volume of the vestibular endolymphatic space could be assessed with high reliability in patients with obstructive VS and that it is significantly correlated with the degree of hearing loss as evaluated with the levels of PTA

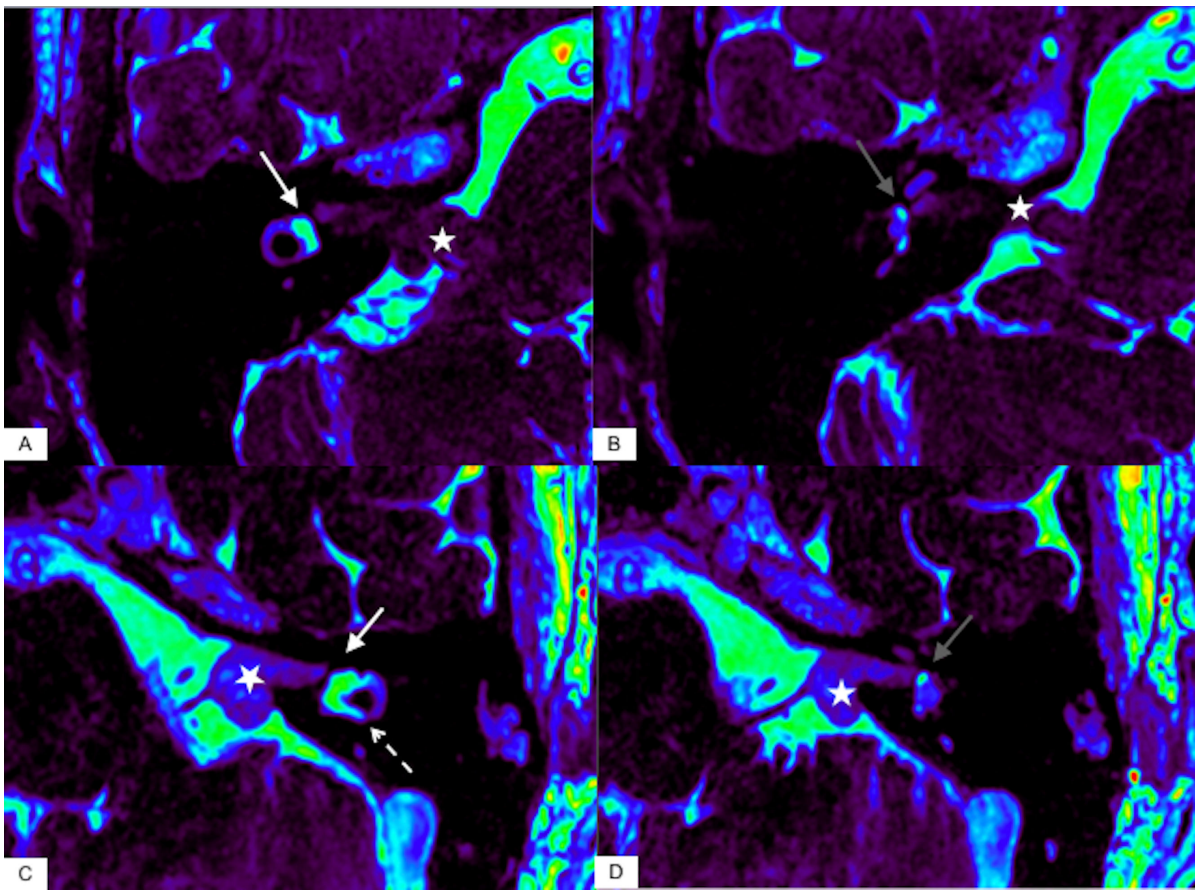

FIGURE 1.20 – **Example of the added values of T2 sequences on Schwannoma patients.** A-B : Axial FIESTA-C sequence with the rainbow-scale on color map at the level of the utricle (A, white arrow) and the saccule (B, gray arrow) in a patient with a right vestibular schwannoma 1.19 cm3 (white asterisk). The volume of the vestibular endolymphatic space is 16.5 mm3 and the levels of PTA and SRT are conserved, measured at 22.5 and 30 dB respectively. C-D : Patient 8. Axial FIESTA-C sequence with the rainbow-scale on color map at the level of the utricle (C, white arrow) and the saccule (D, gray arrow)) in a patient with a left 0.76 cm3 vestibular schwannoma (white asterisk). The utricle is dilated (21.6 mm3), protruding in the lateral semicircular canal (white dotted arrow) and the volume of the vestibular endolymphatic space is 26.1 mm3. The levels of PTA and SRT are 108.75 and 120 dB respectively.

(p=0.032) and SRT (p=0.004) . The volume of the utricle is correlated with the degree of hearing loss evaluated with the levels of PTA (p=0.015) and SRT (p=0.004). On the other hand, the saccule volume was not related to the levels of PTA (p=0.71) and SRT (p=0.38).

The FIESTA-C contrast is based on T2/T1 ratios. Thus, it is conceivable that the elevated protein content in the perilymphatic space decreases the perilymphatic signal by shortening both the T1 and T2 of the perilymphatic fluid. Venkatasamy et al. [38] showed significant decrease in perilymphatic signal on FIESTA-C sequence, depending on the degree of obstruction of the internal auditory canal, potentially responsible for the failure of perilymphatic drainage. In this

study there was no perilymphatic signal decrease in patients with non-obstructive schwannomas (17% of cases). We also support this theory, since 6 patients with non-obstructive schwannomas were excluded in our study due to the absence of a significant perilymphatic signal decreased on FIESTA-C. They presented with lower PTA (23.3 dB vs 57.9 dB) and SRT (42.5 dB vs 60.2 dB) levels than patients with obstructive schwannomas. Here, we demonstrate that FIESTA-C sequences enable the assessment of the utricle and the saccule in 72% of cases in patients with an obstructive schwannoma and with a high spatial resolution and a reasonable acquisition time (4 minutes 40 seconds).

We can mention that we also excluded 3 patients with obstructive tumors because they presented with both endolymphatic and perilymphatic signal decrease. We raise the hypothesis that in these patients the endolymphatic signal decrease was related to the proteinaceous precipitates involving the endolymphatic space, as it has been observed in histopathological study [9].

Interestingly, these 3 patients presented with lower PTA (38.75 dB vs 57.9 dB) and SRT (45 dB vs 60.2 dB) levels than patients with obstructive schwannomas with isolated perilymphatic signal decrease but this difference was probably related to the small number of patients. Patients with VS mostly complain of progressive sensorineural hearing loss, low speech discrimination, tinnitus and balance disorders. The neural degeneration induced by compression of the nerve is not sufficient to explain sensorineural hearing loss. Nadol et al. [39] reported that hearing loss level does not correlate with the size of the tumor and that some schwannoma patients presented a relative preservation of speech discrimination with pure-tone sensorineural hearing loss.

It has been demonstrated that the elevated perilymphatic protein content is caused by obstruction of the cochlear aperture [17] rather than by blockage of the neuroaxonal transport, breakdown of the blood-perilymph barrier and immune response to the tumor. Hizli et al. [9] observed with histopathological examination EH involving the saccule in 50% of cases and involving the utricle in 40% of cases, while Mahmud et al. [10] never reported EH in non-operated schwannoma when speech discrimination was greater than 50%. Naganawa et al. [37] assessed the rate of EH in patients with VS on non-contrast 3D-FLAIR images due to the high-signal of the perilymph causing by the increased protein content. However, study of correlation between the presence of EH and the hearing threshold was not performed.

To our knowledge, our study is the first to measure the volume of the saccule and utricle in vivo without contrast media injection in schwannoma patients. Morita et al. [40] measured the volume of each part of the membranous labyrinth on 31 normal temporal bones, with mean volumes and upper normal volume limits of the saccule and the utricle of 2.42 and 3.68 mm3 and 10.65 and 16.45 mm3 respectively. The mean volume of the saccule and the utricle in our study were 3.17 and 14.4 mm3 respectively, which is higher than the volumes found by Morita et al. and close to their upper normal volume limits, suggesting EH in some patients with schwannoma. ‘

Therapeutic implications

It has been reported that 75% of VS show no growth, leading to a "wait and scan" attitude. In cases of growing tumors, the mean rate varies between 2 and 4 mm per year. The decision of surgery (destructive or conservative) or gamma knife therapy is based on the experience of the surgical team, the degree of hearing loss, the growth rate and the patient's morbidities. Gamma knife radiosurgery is the first-line treatment in patients with small- to medium-size tumors and functional hearing while surgery is usually considered for large-size tumors.

Imaging can provide knowledge on EH associated with schwannoma in patients on conservative treatment to preserve hearing thus allowing the implementation of therapies such as diuretics to reduce EH. Indeed, it has been demonstrated on MRI that some patients with Meniere's Disease show improvement of symptoms and resolution of EH after having been treated with acetazolamide [41]. Recently, patients with schwannoma and disabling vertigo were treated with intratympanic gentamicin, which is presumed to reduce the production of endolymph and consequently EH.

Limitations

The vestibular endolymphatic space could not be evaluated in 28% of patients with VS on non-contrast FIESTA-C sequences either because of a lack of significant decrease in perilymphatic signal in cases with non-obstructive schwannoma or the decreased endolymphatic signal related to the high endolymphatic protein content. The volume of the utricle and the saccule on the contralateral side of the schwannoma could not be evaluated since there was no perilymphatic signal decreased thus we could not compare the volume of the endolymphatic space between both sides. The main problem we encountered was the impossibility of confirming the tumor type and the volume of the vestibular endolymphatic space with pathological analysis in vivo. While these results are encouraging in a small number of patients, further multicenter studies are needed in a larger population to assess the feasibility of T2-weighted echo-gradient sequences with other manufacturers such as Philips® (bFFE sequence, ie. Balance Fast Field Echo sequence) and Siemens® (CISS sequence, ie. Constructive Interference in Steady State sequence).

To conclude, FIESTA-C sequence enables the assessment of the vestibular endolymphatic space in 72% of cases with a high reliability and its size is correlated with the degree of hearing loss as evaluated with the levels of PTA and SRT. As most patients with schwannoma benefit a "wait and scan" attitude or a conservative treatment, based on the MRI results, therapies to reduce EH in order to improve hearing could be administrate.

1.5 Robustness of endolymphatic hydrops evaluation with MRI

1.5.1 Open the database : The Hydrops initiative


European Radiology
https://doi.org/10.1007/s00330-018-5759-6

EDITORIAL

CrossMark

Data sharing improves scientific publication: example of the "hydrops initiative"

Arnaud Attyé [1,2]

Received: 30 July 2018 / Revised: 21 August 2018 / Accepted: 13 September 2018
© European Society of Radiology 2018

FIGURE 1.21 – **European Radiology Editorial presentation**

Major roles of scientific articles are to improve public-health practice, to make scientific advances and/or to share with colleagues the new technology that could help them to improve patient management. Based on data scientists' expertise in Machine Learning algorithms and Artificial Intelligence, there is a growing implication of private companies in research, and a real risk of the exclusion of radiologists from the next major findings in our domain.

With this regard, efforts to improve the reproducibility and integrity of science are crucial to ensure persistent academic interest in this specialty. A first step towards preventing False Science or Fake News and to mitigate irreproducibility, is to provide access to raw data codes used [42]. Sharing Dicom Files valorizes the contribution of radiologists in the research pipeline :

1/The availability of Dicom Files not only allows other researchers to judge the representativity of reports and the discernment of authors in selecting images for publication, but also promotes better understanding of the proposed new method and improves the relevance of questions from other radiologists and/or reviewers.

2/Opening our databases for further analyses, meta-analyses or method validation is an excellent way to address deeply fundamental questions about human diseases. The Human Connectome Project (http ://www.humanconnectomeproject.org/), the ADNI database for Alzheimer's Diseases (http ://adni.loni.usc.edu/) or the Michael J. Fox Foundation Experimental data for Parkinson's Research (https ://www.michaeljfox.org/) are leading examples of public access to data which have led to major advances in knowledge and numerous publications in top-ranked journals.

A practical marker of the usefulness of this approach could be the number of citations of papers with a link to downloadable data. Citations remain a recognized measure of academic influence, indicating the value of a work for later studies ; however, they have some limitations. There is a trend towards a decrease in the number of uncited papers in scientific research [43]

A recent example of such an initiative is Hydrops evaluation using Magnetic Resonance Imaging (MRI). In the last decade, numerous imaging papers from various research teams have shown the feasibility of in vivo visualization of excess endolymph liquid by MRI and its pathological consequences on the auditory or vestibular systems. This new imaging application is mainly due to the efforts of Prof Naganawa's team in Nagoya (Japan) who developed all the steps needed for the scientific validation in humans, including technical development of the acquisition sequences and application to various disease models using a semi-quantitative evaluation [16].

We have recently challenged this classification in European Radiology [18, 25] with a new grading method that relies on the anatomical distinction between two structures of the inner ear : the saccule, which plays a role in balance during vertical movements, and the utricle, a key structure involved in static equilibrium during horizontal movements, such as when driving a car.

Both classification methods have advantages and drawbacks in terms of reproducibility and feasibility in various pathological conditions and depend on the MRI scan technique. In view of the currently somewhat heated debate around the clinical application and interpretation of hydrops images [44], we have proposed to share our raw data (Dicom Files) [45]. Because we obtained approval for a research protocol involving the injection of contrast media in healthy volunteers from the French Agency for Food, Environmental and Occupational Health, we feel essential to share this opportunity with the wider research community.

The MRI acquisitions in healthy volunteers may provide other researchers a control group for their studies and enable them to avoid new injections in asymptomatic adults. The MRI acquisitions in patients come from various manufacturers (Philips, Siemens, General Electric) with different magnetic fields (1.5 and 3 Tesla) for helping radiologists to set their own sequences and for the subsequent reports. Our first sample of data is restricted due to the new recommendations coming from the EU's General Data Protection Regulation (GDPR), which makes it obligatory for radiologists to obtain the explicit consent of subjects before placing their anonymized data in online databases, including databases for research purposes. We hope that other research teams will partake in this initiative by uploading radiological data online, so as to allow us to collectively improve and compare methods of acquisition and grading in the field of Hydrops imaging, with the goal of improving patient management based on MRI information.

Within the first weeks after online publication of the database, we have already received numerous requests for download authorizations from all over the world, sharing our enthusiasm on this fascinating topic.

These data can be downloaded for both research and/or educational purposes. Requests should be submitted via the online form available at :

https ://shanoir.irisa.fr/shanoir-ng/accountRequest with the following indications : Concerned Study : Hydrops ; My Contact in Shanoir : Arnaud Attye ; Role in the study : PI.

1.5.2 Systematic review of magnetic resonance imaging for diagnosis of Meniere disease

Review, *under submission*

Authors : Jose A. Lopez-Escamez, Arnaud Attyé

Meniere disease (MD) is a clinical syndrome defined by episodes of spontaneous vertigo usually accompanied by tinnitus, pressure within the ear and fluctuating sensorineural hearing loss [3]. The syndrome is a heterogeneous condition and several comorbidities have been consistently associated such as autoimmune arthritis [46, 47], psoriasis [48] or migraine [49]. The molecular pathophysiology is starting to be deciphered and different mechanisms including rare allelic variations in autosomal dominant familial MD [50–52] common allelic variants, which regulates the expression of TNF receptors and NFKB-mediated inflammation in mononuclear cells or alterations in the innate response with elevated levels of pro-inflammatory cytokines IL1, IL6 and TNF alpha.

Regardless of the involved molecular mechanisms, the episodes of vertigo have a higher frequency in the first 5 years of the disease [53], but the hearing loss usually progress during the first 5-10 years [24], leading to an accumulation of endolymph (termed endolymphatic hydrops, EH) in the cochlear duct and the vestibular organs (saccule, utricle, ampullae), that has been demonstrated in human histopathological studies. In the last decade, numerous imaging papers from various research teams have shown the feasibility of in vivo visualization of excess endolymph by Magnetic Resonance Imaging (MRI) and its pathological consequences on the auditory or vestibular systems. This new imaging application is mainly due to the efforts of Prof Naganawa's team in Nagoya (Japan) who developed all the steps needed for the scientific validation in humans, including technical development of the acquisition sequences and application to various disease models [34].

However, the reproducibility of MRI sequences to evaluate the amount of endolymphatic fluid as well the system of hydrops classification have been recently challenged [18, 20, 22] in case-controlled studies, and the usefulness of the MRI hydrops protocol remains debatable in clinical practice. In this systematic review, we will discuss the observation of endolymph accumulation with MRI. We will start by briefly outlining the physical basis of MRI sequences for the hydrops protocol including the pitfalls and quality criteria, before discussing findings from case-controlled diagnostic trials testing its usefulness in MD patients and future directions of research.

Methods

This review has been conducted using the criteria recommended by Preferred Reporting Items for Systematic Reviews and Meta-Analyses (PRISMA).

Selection of studies

The assessment and selection of the studies was performed according to the following aspects : Participants definition, Intervention, Control studies, main and secondary Outcome measure and Study design (PICOS) :

(1) Participants : individuals with diagnosis of MD according to 1995 or 2015 diagnostic criteria, sensorineural hearing loss without vestibular symptoms and vestibular migraine according to Barany Society 2012 diagnostic criteria.

(2) Intervention : MRI acquisition with different sequences using either IT or IV GBCA (Gadolinium-based contrast agent), both or no GBCA

(3) Control group : control and non-control studies

(4) Outcome measures : EH visualization in the cochlea or vestibule

(5) Secondary outcomes : other data related to main diagnosis such as duration of disease or hearing threshold.

(6) Study design : randomized case control studies, cases series or cross sectional or studies.

Search Strategy

A structured search using PubMed was performed on the 25th of July 2018, and included all relevant articles published. The search used the following key word combinations : “MRI” AND “Endolymphatic Hydrops” (n=389). Two reviewers have then selected articles published in and after 2013 (n=146). Moreover, references of the retrieved articles were also inspected to extract any further relevant publications. After title and abstract review, the search resulted in 52 individual articles from which additional relevant articles were identified upon examination of the cited references. After having eliminated 3 articles on the basis of non-English language and 35 articles, which consist in letters, reviews and uncontrolled studies, 13 articles were assessed and included in the review for a total of 833 individuals. Importantly, we have excluded studies where the contralateral ears of unilateral MD were used as reference, since bilateral involvement may occur in 10-50% of cases [54]. Others reviewed studies were only focused on methodological development of the hydrops sequence and knowledge coming from temporal bone analysis, both for understanding purpose. The findings coming from the 13 selected studies are separately discussed. However, non-controlled studies were also revised in a dedicated part to analyze the differences in the methodology.

Outcome measures and associated variables

The main objective of this review is to determine if visualization of EH on MRI can be used as diagnostic criteria for MD. For this, information was retrieved from each selected publication regarding patient inclusion criteria, number of patients, duration of disease, use of gadolinium-based contrasts, image acquisition technique and other technical aspects such as inversion time with FLAIR, and location of EH (cochlea, vestibule, semicircular canals).

Data Extraction, Synthesis and Quality Evaluation

From each study the following information was extracted : first author, year of publication, journal, type of study (controlled/ case series), sample size, patient inclusion criteria and the clinical and technical variables described above. The Cochrane Collaboration Tool was used to assess the quality of each study and the risk of bias.

Results

Knowledge from non-controlled studies and methodological pitfalls

MRI sequence physical basis

Hydrops MRI currently relies either on Inversion Recovery (IR) sequences in the vast majority of publications [18, 26, 55–57], or Heavily-Weighted T2 Gradient Echo sequences in few other scientific articles [58, 59]. Using IR sequences, the method of MRI EH evaluation requires contrast media injection and delayed acquisition, in order to selectively enhance the perilymphatic fluid. The signal from one of the two inner ear liquids, the endolymph, is cancelled out. The two inner ear liquids have very close T1 and T2 relaxation times, such that, the proposed contrast to assess endolymphatic filled spaces (ie. hyposignal for endolymphatic spaces and hypersignal for perilymphatic spaces) relies on very slight variations in sequence parameters.

To increase the difficulty in hydrops image interpretation, some research teams obtain the inner ear contrast by subtracting two IR sequences with different Inversion Time [15, 60] or by merging 3D-FLAIR sequence with T2-Weighted sequence [17, 61]. Clinicians should interpret these images with caution to exclude description of endolymph in non-physiologic compartment due to geometric coregistration problem between the two sequences [62]. In addition, it is now possible to acquire one 3D-FLAIR sequence to estimate the distribution of endolymphatic fluid with good inter-reader reproducibility [18].

The 3D-FLAIR sequences are now widely available with all MRI manufacturers without requiring post-processing technique, yet the signal of the endolymph is similar to those of temporal bone, requiring training for interpretation. Finally, other publications [58, 59] proposed MRI analysis through heavily T2 weighted-sequences. It is important to mention that only Gradient-echo sequences (FIESTA sequence for General Electric manufacturer, balanced FFE for Philips and CISS for Siemens) can be used for this purpose because of the low Repetition Time and Echo Time, rendering the sequence sensitive to the presence of inner ear membrane such as those of the saccule. The main problem encountering for clinical practice is movements' artifacts with B0 field inhomogeneities, and it is often difficult to confirm that the "black band" effect which is presumed to be the lateral wall of the saccule is not artefactual.

We can add that it is very difficult to map the utricle and the cochlear duct membranes with T2-weighted sequences with 3T or 1.5T MRI scans due to the low spatial resolution while these sequences are much more efficient in evaluating the cranial nerves size in the internal auditory canal by measuring its diameter.

Contrast media diffusion

Two alternative routes for contrast media administration have been assessed : intratympanic (IT) and intravenous (IV). The main advantage of an IT injection is a higher perilymphatic contrast, particularly in the basal turn if the cochlea, although previous studies suggest this method can cause local toxicity in animal models [13]. In addition, cases of bilateral disease require a double IT injection and an MR scan waiting time of 24 h before imaging acquisition. Partial or complete obstruction of the round window and enlargement of the endolymphatic space could also complicate inner ear analysis after IT injection [35]. One research team has also proposed to inject the contrast media through the Eustachian tube [63], without significant differences with classic IT injection. In contrast, the intravenous method requires a shorter waiting time, which has been evaluated as optimal in the 4-6 hours interval [12].

More recently, effect of varying the contrast media molecule on normal inner ear structures enhancement has been assessed [20] and the use of 3D-FLAIR sequences with constant flip angle proposed are more sensitive that those with variable flip angle for exploring MD patients.

Knowledge from controlled studies

Thirteen case-controlled studies were selected. Ten of them have stated the inclusion criteria for MD (5 used the 1995 AAO-HNS criteria and 5 with the 2015 Barany Society criteria), and 3 of them did not mentioned any criteria (Table 1). The 3D-FLAIR sequence was used in 6 control studies (inversion time range 2100-2400 ms), but it was not described in 9 studies. Seven studies used IV Gadolinium-based contrast agents and 4 studies did not used contrast. Remarkable, the duration of disease was only reported in 3 studies, and this variable probably may explain the large variability observed among studies.

Semi-quantitative grading system

Two grading methods for the EH degree classification have been proposed. The first grading system, proposed by Nakashima et al. [16] with application in a recent case-controlled study [55], divided endolymphatic hydrops grades into three categories : none, mild and significant, both in the cochlea and the vestibule. This semi-quantitative grading system was initially based on the histopathology of the dilated endolymphatic spaces, with separate evaluations for the vestibule and the cochlea. Interestingly, authors found that the presence or absence and degree of vestibular EH were significantly different between ears with MD and control ears. EH in the vestibule might be a specific predictor of definite MD, but the utricle and saccule were not individually assessed.

Another limitation for the three-stage grading of Nakashima et al. is that it is easy to shift from the normal condition to endolymphatic hydrops disease simply by varying the Inversion Time sequence by 100 ms [20, 22]. The use of an anatomical landmark such as utricle to do a relative qualitative diagnosis of saccular expansion has proven to be less sensitive to acquisition

condition, yet not perfect for saccular hydrops diagnosis. The semi-quantitative classification has the advantage of encompassing the cochlear duct for hydrops disease diagnosis, however some studies have suggested a lower specificity in MD patients [18, 55]. A recent meta-analysis of temporal bone studies also proposed a cochleocentric distribution of the endolymph fluid with constant cochlear duct dilatation in healthy subjects [7], rendering probable the frequent visualization of endolymph in normal cochlear duct with MRI.

Saccular and Utricular grading system

In temporal bone studies, EH typically involves the pars inferior of the labyrinth, mainly the saccule [4] Saccular hydrops, can range from mild to severe, based on the degree of membrane distension toward the stapes footplate, as seen in post-mortem studies [5]. Furthermore, the degree of distension of the inner ear structures appears to be related to their mechanical compliance, which is high in the case of the saccule, but lower for the utricle and semi-circular canals [8]. Case-controlled studies have proposed a new measure based on the size and morphology of the saccule obtained using a 3D-FLAIR sequence, the saccule to utricle ratio inversion (SURI) (Figure 1.22).

The current limitations of this classification are the absence of cochlear duct evaluation and difficulties to distinguish utricle from saccule in most extensive cases of saccular hydrops [44]. The inclusion of grading for utricular protrusion into the lateral semicircular canal, following IT contrast media injection [64], could significantly ameliorated this classification usefulness.

The role of saccular hydrops in Meniere's Disease diagnosis

Three different research groups have demonstrated saccular expansion in MD patients : Venkatasamy et al. have compared high-resolution T2-weighted images of the saccule in normal subjects with histological sections from cadavers and to identify its changes in MD, compared to healthy volunteers. They have found no correlation between the presence of saccular hydrops and the duration of the disease or the hearing loss degree, while saccular abnormalities were found in 84% of the cases of MD patients with bilateral location in 30% of MD cases. A global correlation was found with the presence of hearing loss, unilateral hypovalence on vestibular test or time of completion of the MRI after the last crisis.

Simon et al. [59] have used the same method to measure saccular height and width in a coronal plane for MD patients. The estimated sensitivity and specificity was 63% and 95% for height, and 41% and 95% for width, respectively, for the symptomatic ear The inter-rater reliability was 0.76 for height and 0.51 for width measurements.

Finally, Attyé et al. have investigated the relationship between the presence of saccular hydrops and clinical presentations in three prior publications. In the first article, which corresponds to the first mention of the SURI method, they found that half of 30 MD patients presented saccular hydrops in the symptomatic ear [18]. They have further studied the role of saccular

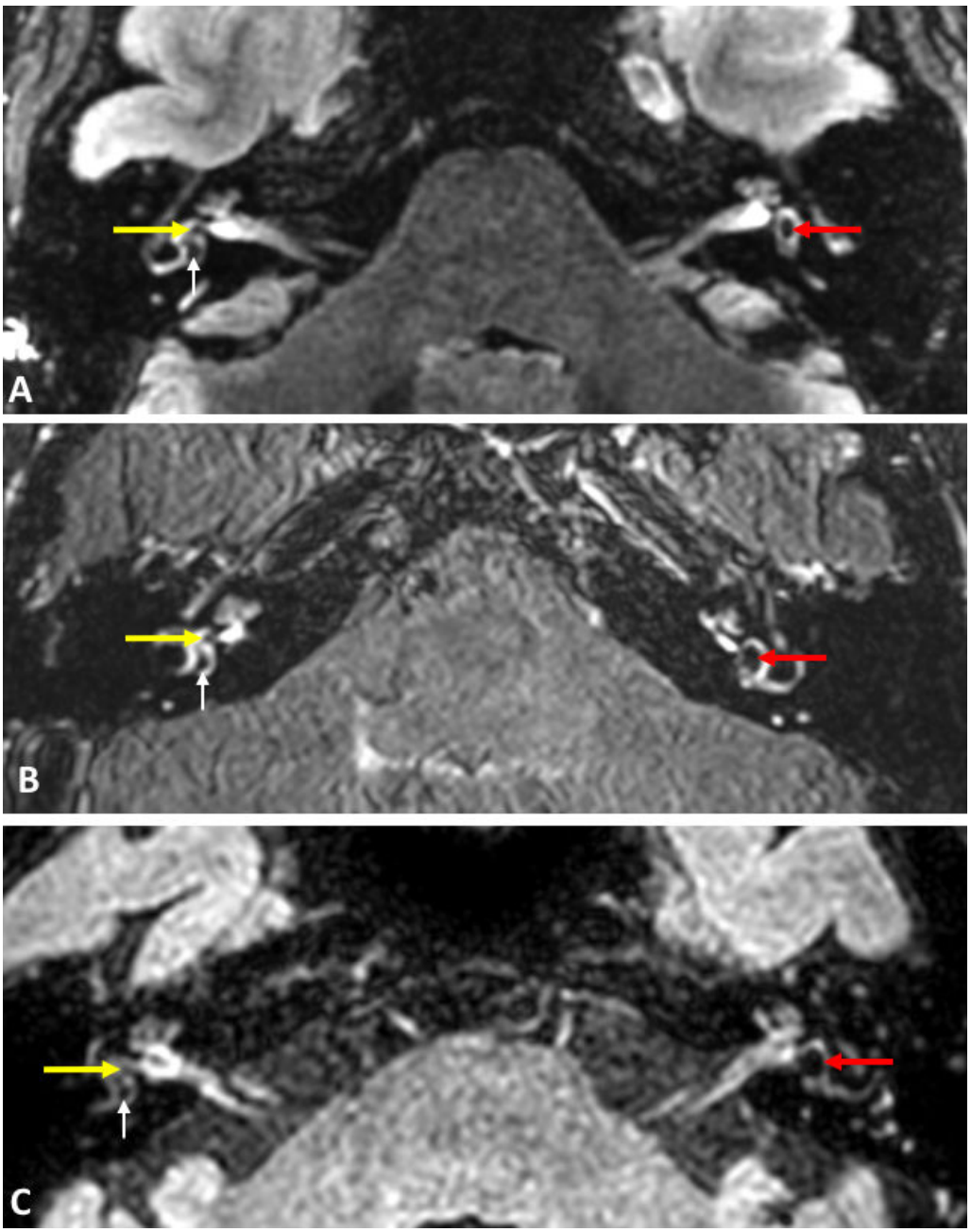

FIGURE 1.22 – **3D-FLAIR sequences in the axial slice of reference in 3 different MD patients with left saccular hydrops, as assessed with the SURI method.** Patient A was explored with General Electric MRI scan, patient B with Siemens MRI scan and patient C with Philips MRI scan. On the right inner ears, the saccules (dotted arrows) appear smaller than the utricle (white arrows). No saccular hydrops is detected. On the left inner ears, the utricle was not visible, the saccules (white stars) was the only displayed endolymphatic structure at the inferior part of the vestibule. A saccular hydrops is detected. These pictures are extracted from the online database available for researchers

hydrops by comparing subsets of 20 patients with isolated SNHL, recurrent vestibulopathy and Definite MD, and a control group, demonstrating that saccular hydrops correlates with SNHL level above 40 dB while vertigo patients without SNHL do not have saccular hydrops. Furthermore, saccular hydrops was described in patients without clinical diagnosis of MD, and in subjects with isolated low-tone sensorineural hearing loss [62]. In another publication, the same group further confirmed that inner ear MRI showed hydrops when hearing loss was higher than 35 dB [26].

We have not found any MRI studies to visualize hydrops in patients with familial MD or according to clinical variants of MD, and there are no longitudinal follow-up studies.

Differential diagnoses for MD

A large retrospective case-controlled study including 200 patients with MD has shown that besides saccular hydrops, radiologists must to be vigilant to other inner ear disorders, such as perilymphatic fistulae, inner ear malformations or brain lesion along central cochleovestibular pathways, which may mimic MD symptoms. Interestingly, there was a correlation between the presence of perilymphatic fistula and past history of intratympanic gentamicin administration, and some MD patients presented with semicircular canal enhancement, which has to be further investigated with regards to the potential presence of associated benign positional vertigo. The presence of perilymphatic fistulae in patients with MD symptoms was not associated with saccular hydrops.

Associated MRI study of Internal Auditory Canal cranial nerves

The principal central pathway for audition and equilibrium leading to the cerebral cortex passes from the labyrinth, via the cochlea-vestibular nerve (VIII) to the brainstem nuclei. Sensorineural degeneration of cochlear and vestibular nerves has been proposed as involved in MD [65, 66] while EH should be considered as a histologic marker for MD rather than being directly responsible for its symptoms [67].

Henneberger et al. and Flatz et al. [68, 69] have then proposed to measure both VIII nerve and VII nerve via their diameters in MD patients compared with controls using MRI. **They have demonstrated swelling of these nerves in the MD group, raising the hypothesis that although cellular death would theoretically be expected to lead to a decreased nerve thickness, the increase of VII and VIII nerves diameter will support a mechanism of neuroinflammation in MD pathophysiology.**

Conclusions

1/ Conclusions on methods for MRI studies in MD

Although there is some variability in the method to visualize EH, the most common sequence is 3D-FLAIR combined with IV GBCA. For 3D FLAIR based studies, the inversion time is critical

to discriminate perilymph versus endolymph and it is not described in most of the studies.

2/ Conclusions on MRI findings in MD

A. MRI EH can be reliable measured in the saccule using the SURI method.

B. EH in the saccule is associated with hearing loss and probably with the duration of disease.

C. Uncontrolled studies have described EH in patients with vestibular migraine, acute low tone SNHL (without vertigo), tinnitus regardless of hearing loss and autoimmune inner ear disease.

Table: MRI case control studies in MD (N=13)

Author	Year	Inclusion criteria	Patients (N)	Ears (N)	Intervention	Imaging	Inversion time	Duration of disease
Attyé	2018	2015	60		IV GBCA	3D FLAIR		Not reported
Flatz	2018	Non stated	60		IT+IV GBCA	3D CISS		Not reported
Yoshida	2018	Non stated	63	94	IV GBCA	3D FLAIR		99 mo
Simon	2017	2015	72		IV GBCA	CISS		Not reported
Eliezer	2017	2015	12		IV GBCA	3D FLAIR	2300/ 2400	Not reported
Henneberger	2017	1995	60		IT GBCA	3D CISS		Not reported
Keller	2017	Non stated	85		No	T2w		Not reported
Tawfik	2017	1995	112		No	T1w/T2w		18 mo
Venkatasamy	2017	2015	128		No	T2w, FIESTA-C		37 mo
Attyé	2017	1995	60	120	IV GBCA	3D FLAIR	2300	Not reported
Van den Burg	2017	2015	53		No	T2w		Not reported
Ito	2016	1995	46		IV GBCA	3D FLAIR	2250	Not reported
Sepahdari	2015	1995	22	41	IV GBCA	3D FLAIR	2100	Not reported

FIGURE 1.23 – **MRI case-controlled studies in Meniere's Disease**

CHAPITRE 2

CENTRAL AUDITORY PATHWAYS MRI EXPLORATION

2.1 Streamline tractography for cranial nerve exploration : state of the art

2.1.1 Cranial Nerves Tractography : Overview

Scientific article published in *Neurosurgery* [70] , summarized for the introduction of the thesis part two.

Authors : Timothee Jacquesson, Carole Frindel, Gabriel Kocevar, Moncef Berhouma, Emmanuel Jouanneau, Arnaud Attyé, Francois Cotton

Rationale

Based on the study of extracellular water motions diffusion [71], the diffusion weighted imaging allows to assess any condition influenced by intra and extracellular environments. Diffusion Tensor Imaging (DTI) [72] is now a well-documented technique for assessing cranial nerve integrity, since in nerve fibers, the water diffusion parallel to the direction of the nerve is assumed to be unrestricted while that occurring perpendicularly to this is constrained by membranes. The post-processing method that consists in reconstructing the fibers is called the tractographic method [73], which has benefited from methodological improvements allowing to display nerve or white matter fascicle with probabilistic algorithms. The DTI technique allows extracting quantitative biomarkers ; the most commonly used is the fractional anisotropy (FA), a scalar value that describes the anisotropy of water diffusion. This anisotropic behavior is based on a Gaussian distribution of the water molecule motion in tissue. However, some drawbacks exist with the DTI technique, as it is known to potentially yield misleading information regarding the actual pathways of white matter in the brain [74] mainly owing to the “fiber crossing

problem". Indeed, the DTI model can't properly estimate the orientation of fibers when voxels contain at least two white matter population. Thus, changes in the FA metrics are often only driven by different degrees of fiber coherence in the brain, which is problematic given recent estimation suggesting that between 70% and 90% of the entire white matter in the human brain is characterized by at least two or more fiber populations [75].

The technique of Constrained Spherical Deconvolution (CSD) was introduced in two influential publications (2004 and 2007) by Tournier et al. to solve limitation of the DTI model [76, 77]. The CSD method allows the estimation of fiber orientation distribution (FOD), directly from diffusion-weighted MRI data, without the need for prior assumptions regarding the number of fiber populations present. Using this diffusion model, the signal measured within a voxel is assumed to correspond to the sum of the DW signals that would have been measured for each fiber population in isolation. It aims at directly estimating the fiber Orientation Density Function (fODF, also known as Fiber Orientation Distribution -FOD-), which is critical to further perform tractography. Cranial nerve anatomy has long been described from post mortem brain dissections by eminent anatomists. Tracking of small-scaled structures, such as cranial nerves, remains an ongoing challenge because of their small size, an intricate anatomical environment sensitive to susceptibility artifacts, and a limited MRI resolution.

To introduce the second part of the thesis, we propose a targeted review collecting all technical details and pointing out challenges and solutions in cranial nerve tractography. We compare parameters and aim to provide a better understanding of this imaging tool for future routine clinical use.

Summarized methods

A "targeted" review of the scientific literature was carried out using the MEDLINE database. We selected studies that reported how to perform the tractography of cranial nerves, and extracted the following : clinical context ; imaging acquisition settings ; tractography parameters ; regions of interest (ROIs) design ; and filtering methods. For all studies selected, we extracted all parameters used along the whole tractography processing pipeline (Figure 2.1), including clinical context (number of patients ; pathological condition or type of tumor ; cranial nerve studied ; visualization rate, see Figure 2.2), MRI acquisition setup (magnetic field ; number of gradient directions ; slice thickness ; b-value ; voxel size ; sequence of reference), software and computational parameters (fractional anisotropy threshold ; maximal curvature angle ; minimal length), region of interest (ROI) design strategy, and filtering and validation methods.

Main Results

Twenty-one published articles were included. These studies focused on the optic nerves in supra-sellar tumors, trigeminal nerve in neuro-vascular conflicts, the facial nerve position around vestibular schwannomas, or all cranial nerves. Over time, the number of MRI diffusion gradient directions increased from 6 to 101. Nine tracking software packages were used which offered

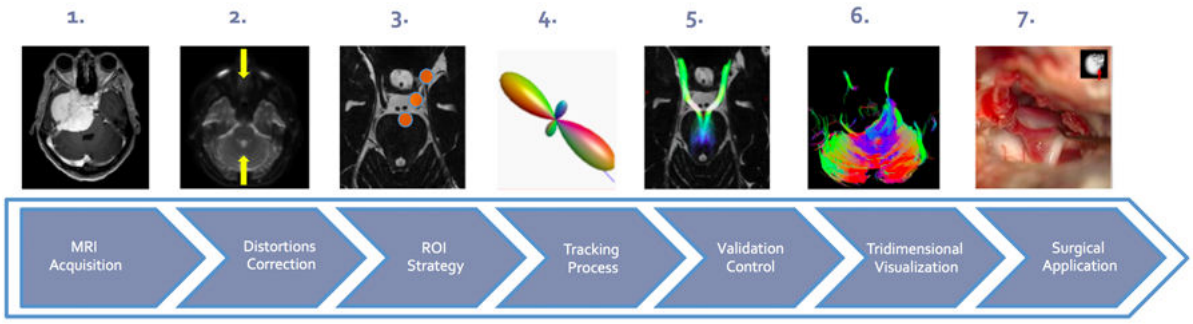

FIGURE 2.1 – **Visual summary of the tractography processing pipeline.** The tracts corresponding to the white fibers are reconstructed following seven steps : 1 – dedicated cerebral MRI acquisition with a diffusion sequence, 2 – geometric distortions correction, 3 – region of interest (ROI) design, 4 – tractography with specific parameters, 5 – anatomical control and filtering of spurious tracts, 6 – appropriate tridimensional visualization, 7 – surgical application and ground truth correlation.

various types of tridimensional display. Tracking parameters were disparately detailed except for fractional anisotropy, which ranged from 0.06 to 0.5, and curvature angle, which was set between 20 and 90°. ROI design has evolved towards a multi-ROI strategy. Furthermore, new algorithms are being developed to avoid spurious tracts and improve resolution.

MRI machine constructors were General Electric (General Electric Healthcare, Milwaukee, WI, USA), Philips (Philips Medical System, Best, Netherland), and Siemens (Siemens Medical Solutions, Erlangen, Germany) ; machines had a permanent magnetic field of 3 Tesla (T) with the exception of two earlier studies that used a 1.5T magnetic field.20,31 MRI diffusion parameters varied and the spatial resolution increased over time. The number of gradient directions ranged from 6 to 101, and most of the studies (n=11) reported between 20 to 32 gradient directions. The b-value was almost always 1000 s.mm-2 except for two studies for which the b-value was 800 s.mm-2.4,32 Slice thickness ranged from 3 to 1.2 mm and voxel size from 2.5 to 0.6 mm.

The main finding of this targeted review is that the result of tracking strongly depends on the anatomy of the cranial nerve tracked, its environment, and the post-processing steps (Figure 2.3). From this we identified two challenges, one related to the anatomy of cranial nerves and the other to the tractography technique, and we provide suggestions for best strategies to overcome them in routine neurosurgical practice.

Tractography has already caught the attention of the scientific community since it allows the non-invasive in vivo description of brain white matter connections. This technology is still difficult to apply to small neurological structures such as cranial nerves. In the present paper, we review technical details of the whole tractography pipeline and we demonstrate the paramount importance of the tracking parameters that depend on the features of each cranial nerves,

Date	Authors	Patients	Pathology	CN studied	Visualization rate
2006	*Taoka et al.*	8	Vestibular schwannomas	VII/VIII	62.5%
2007	*Kabasawa et al.*	4	Healthy subjects	V, VIII	100%
2009	*Salmela et al.*	2 +10 HS	Supra sellar tumor	II	100%
2010	*Hodaie et al.*	4	"Neurosurgical patients"	II, III, V, VI, VII/VIII, X	63.6%
2011	*Chen et al.*	3	Vestibular schwannomas	VII/VIII	100%
2011	*Fujiwara et al.*	13 + 14HS	Trigeminal neuralgia	V	100%
2011	*Gerganov et al.*	22	Vestibular schwannomas	VII/VIII	90.9%
2012	*Hodaie et al.*	5	Trigeminal neuralgia	V	100%
2012	*Roundy et al.*	5 +1HS	Cerebellopontine angle tumors	VII/VIII	100%
2013	*Zhang et al.*	8	Vestibular schwannomas	VII/VIII	87.5%
2014	*Choi et al.*	11	Vestibular schwannomas	VII/VIII	100%
2015	*Vos et al.*	5 + 5HS	Deafness	VIII	100%
2015	*Wei et al.*	23	Vestibular schwannomas	VII/VIII	91.3%
2015	*Yoshino et al.*	22	Vestibular schwannomas	VII/VIII	81.8%
2016	*Borkar et al.*	20	Vestibular schwannomas	VII/VIII	95%
2016	*Song et al.*	15	Vestibular schwannomas	VII/VIII	100%
2016	*Hilly et al.*	28 + 13HS	Cerebellopontine angle tumors	VII/VIII	95,20%
2016	*Zhang et al.*	30	Vestibular schwannomas	VII/VIII	96.7%
2016	*Yoshino et al.*	3 + 4HS	« Brain tumors », HCP atlas	All CNs I to XII	100%
2017	*Zolal et al.*	5 + 30HS	Skull base tumors	II, III, V VII/VIII	30-70%
2017	*Behan et al.*	10	Cerebellopontine angle tumors	V, VII/VIII	100%

NR = not reported, HS = healthy subjects

FIGURE 2.2 – Clinical context : number of patients, pathology, studied cranial nerves and visualization rate.

anatomical environment and tumor morphology, and above all a tailored design of ROI. As this targeted review points out, applying tractography to cranial nerves demands advanced anatomical, radiological, and computational skills to achieve correct fiber tracking and to avoid spurious tracts. Nevertheless, advances such as faster imaging acquisition, high resolution post-processing, and multi-ROI tracking may help to overcome challenges, address the reconstruction of all cranial nerve trajectories, and promise new perspectives in neuroradiology, skull base surgery, and neuroanatomy.

Year	Author	Machine	Field (T)	Gradient Directions	Slice thickness (mm)	b-value (s/mm2)	Anatomical Ref.	Acquisition Voxel size
2006	*Taoka et al.*	Siemens	1.5	6	NR	1000	T2 CISS	NR
2007	*Kabasawa et al.*	General Electric	3	6	3	800	T2 FLAIR	NR
2009	*Salmela et al.*	Philips	3	6	2	1000	T2	1.9x2x2
2010	*Hodaie et al.*	General Electric	3	25	3	1000	T1 and T2 Fiesta	NR
2011	*Chen et al.*	General Electric	3	25	3	1000	T1 and T2 Fiesta	NR
2011	*Fujiwara et al.*	General Electric	3	6	1.2	1000	3D-bSSFP	1,6x1,6x1,2
2011	*Gerganov et al.*	Siemens	3	12	1.6	1000	T2 CISS	NR
2012	*Hodaie et al.*	General Electric	3	25	3	1000	T2 and T1W	NR
2012	*Roundy et al.*	Philips	3	32	1.2	1000	T2 FIESTA	0.78x0.78x1.2
2013	*Zhang et al.*	Siemens	3	NR	3	1000	NR	NR
2014	*Choi et al.*	Philips	1.5	32	2.5	1000	NR	2,5x2,5x2,5
2015	*Vos et al.*	Philips	3	22	1.8	1000	T2 DRIVE	NR
2015	*Wei et al.*	Siemens	3	30	2	NR	T2 CISS	0.6x0.6x0.6
2015	*Yoshino et al.*	General Electric	3	30	2.5	1000	T2 FIESTA	NR
2016	*Borkar et al.*	Philips	3	15	1.5	800	T1W	0.78x0.78x1,5
2016	*Song et al.*	General Electric	3	30	1.2	1000	FIESTA	NR
2016	*Hilly et al.*	Philips	3	32	2	NR	T2 CISS	2x2x2
2016	*Zhang et al.*	General Electric	3	64	2	1000	T2 FIESTA	NR
2016	*Yoshino et al.*	Siemens	3	101	2.4	12 B-values	T1W	2,4x2,4x2,4
2017	*Zolal et al.*	Siemens	3	20	2	800	2x2x2	T1 or T2 CISS
2017	*Behan et al.*	General Electric	3	60	3	1000	0.9375x0.9375x3	T1

NR = not reported

FIGURE 2.3 – MRI Acquisition setups : MRI machine, permanent field strength, number of gradient directions, slice thickness, b-value, anatomical reference and acquisition voxel size.

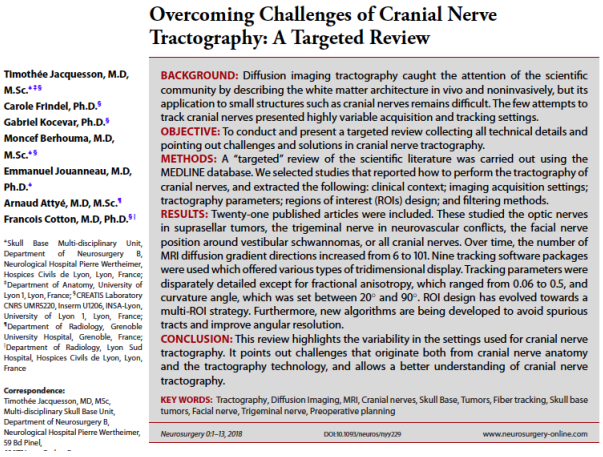

Overcoming Challenges of Cranial Nerve Tractography: A Targeted Review

Timothée Jacquesson, M.D, M.Sc.[*†§] **Carole Frindel, Ph.D.**[§] **Gabriel Kocevar, Ph.D.**[§] **Moncef Berhouma, M.D, M.Sc.**[*¶] **Emmanuel Jouanneau, M.D, Ph.D.**[*] **Arnaud Attyé, M.D, M.Sc.**[¶] **Francois Cotton, M.D, Ph.D.**[‖¶]

[*]Skull Base Multi-disciplinary Unit, Department of Neurosurgery B, Neurological Hospital Pierre Wertheimer, Hospices Civils de Lyon, Lyon, France; [†]Department of Anatomy, University of Lyon 1, Lyon, France; [§]CREATIS Laboratory CNRS UMRS220, Inserm U1206, INSA-Lyon, University of Lyon 1, Lyon, France; [¶]Department of Radiology, Grenoble University Hospital, Grenoble, France; [‖]Department of Radiology, Lyon Sud Hospital, Hospices Civils de Lyon, Lyon, France

Correspondence: Timothée Jacquesson, MD, MSc, Multi-disciplinary Skull Base Unit, Department of Neurosurgery B, Neurological Hospital Pierre Wertheimer, 59 Bd Pinel,

BACKGROUND: Diffusion imaging tractography caught the attention of the scientific community by describing the white matter architecture in vivo and noninvasively, but its application to small structures such as cranial nerves remains difficult. The few attempts to track cranial nerves presented highly variable acquisition and tracking settings.

OBJECTIVE: To conduct and present a targeted review collecting all technical details and pointing out challenges and solutions in cranial nerve tractography.

METHODS: A "targeted" review of the scientific literature was carried out using the MEDLINE database. We selected studies that reported how to perform the tractography of cranial nerves, and extracted the following: clinical context; imaging acquisition settings; tractography parameters; regions of interest (ROIs) design; and filtering methods.

RESULTS: Twenty-one published articles were included. These studied the optic nerves in suprasellar tumors, the trigeminal nerve in neurovascular conflicts, the facial nerve position around vestibular schwannomas, or all cranial nerves. Over time, the number of MRI diffusion gradient directions increased from 6 to 101. Nine tracking software packages were used which offered various types of tridimensional display. Tracking parameters were disparately detailed except for fractional anisotropy, which ranged from 0.06 to 0.5, and curvature angle, which was set between 20° and 90°. ROI design has evolved towards a multi-ROI strategy. Furthermore, new algorithms are being developed to avoid spurious tracts and improve angular resolution.

CONCLUSION: This review highlights the variability in the settings used for cranial nerve tractography. It points out challenges that originate both from cranial nerve anatomy and the tractography technology, and allows a better understanding of cranial nerve tractography.

KEY WORDS: Tractography, Diffusion Imaging, MRI, Cranial nerves, Skull Base, Tumors, Fiber tracking, Skull base tumors, Facial nerve, Trigeminal nerve, Preoperative planning

Neurosurgery 0:1–13, 2018 DOI:10.1093/neuros/nyy229 www.neurosurgery-online.com

FIGURE 2.4 – **Further results, figures and details can be found in the following paper : Neurosurgery, Rank A, Impact Factor 4.47, Number of citations (Scopus, October the 1st 2018) : 0**

2.1.2 Probabilistic tractography to predict the position of cranial nerves displaced by skull base tumors : value for surgical strategy through a case series of 62 patients.

Scientific article, in press in *Neurosurgery*

Authors : Timothee Jacquesson, Francois Cotton, Arnaud Attyé, Sandra Zaouche, Stéphane Tringali, Justine Bosc, Philip Robinson, Emmanuel Jouanneau, Carole Frindel

Skull base tumor surgery remains a challenge since it requires complex surgical approaches sparing the brain and reaching deep-seated tumors within a dense anatomical environment that includes many cranial nerves and vessels. Even though the cerebral vascular supply or drainage is assessed adequately by cerebral magnetic resonance imaging (MRI) or angiography, depicting the whole cranial nerve trajectory from the brainstem to their target through the skull base and around tumors is not yet achievable in the routine clinical practice ; high-resolution T1 or T2 classical MRI sequences can describe only the cisternal segment of the largest cranial nerves in normal conditions.

Advances in diffusion magnetic resonance imaging (MRI) have used the unequal movement of water molecules along axons to reconstruct white matter fibers through a new post-processing called “fiber tracking” or “tractography”. This technique has gained the enthusiasm of the scientific community as it has brought a novel way to explore the in vivo brain white matter architecture. Nonetheless, tractography involves a complex multi-step processing pipeline and is still difficult to apply in fiber crossing areas[78] or to small-scale structures such as cranial nerves. These aspects have been overcome by progress made both in imaging acquisition and computational post-processing. Beyond the initial deterministic methods using a single diffusion tensor,[72] fiber tracking is evolving towards a fiber orientation distribution function (ODF) method that can detect several orientations of fibers in the same voxel.[76, 77] Furthermore, probabilistic algorithms with a constrained spherical deconvolution method provide a better depiction of crossing or small white matter tracts.[74, 79].

Predicting cranial nerve trajectories that are displaced by skull base tumors could be of help for surgery, as attested by recent studies focusing on the facial nerve course in vestibular schwannomas surgery using tractography. However, most cranial nerve tractography studies have focused on a single cranial nerve and a particular type of tumor, and have used a deterministic algorithm.[70] We report herein our experience through this large series of various skull base tumors for which all displaced cranial nerves were depicted using a probabilistic tractography algorithm. We describe how this technique can help the surgical management of such tumors and we detail the whole tractography processing pipeline, including MRI acquisition settings, tracking parameters, and the crucial placement of regions of interest (ROIs).

METHODS

Population and Data acquisition

The study was carried out in the skull base surgery department of Lyon University Hospital between December 2015 and December 2017. Patients were consecutively included if they had a history of skull base tumor displacing one or multiple cranial nerves. In the case of vestibular schwannomas, the classification described by Koos et al.[80] was used. The follow-up after surgery was at least six months and concerned mostly cranial nerve palsy. MRI images were acquired using a 3-Tesla Ingenia machine (Philips Medical Systems, Best, The Netherlands) with a 32-channel head coil. Diffusion images were acquired with following settings : b-value 1000s/mm2 ; 32 directions ; TE/TR 102/3956ms, voxel size 2mm isotropic ; slice thickness 2mm ; no slice gap ; 26 slices ; single-shot spin-echo sequence ; and scan time 9min52s. The limits of the acquisition box were the optic tracts superiorly and the foramen magnum inferiorly. According to Andersson et al. [81], two sequences with two images for each diffusion gradient and opposed polarities of the phase encoding direction were used for distortion correction : posterior-to-anterior (PA) and anterior-to-posterior (AP).

Tractography

A brain mask defined the processing workspace for tractography and included the whole brainstem, the cerebrospinal fluid cisterns and the skull base foramina in which cranial nerves course. Subsequently, supra-tentorial structures were excluded. 'Eddy' and 'topup' FSL (FMRIB software library) functions, as implemented in the MRtrix software, were used for susceptibility and Eddy's current artifacts' correction. The ROIs design involved a superimposition of the FOD map onto anatomical T2 pictures. ROIs were placed on the best identifiable aspect of the cranial nerve in its cisternal segment in the three dimensions : axial, sagittal, and coronal (Figure 2.5). For each cranial nerve, a single ROI was used ; ROIs were volumes (cube or sphere) and tailored to the anatomical features of each cranial nerve before initiating the tracking. A region of exclusion (ROE) was drawn at the roof of the fourth ventricle in the coronal plane. Sometimes, another ROE was used within the tumor.

The tractography process used the MRtrix3 software. For each voxel of the brain mask, the fiber population was estimated by a response function using the *fa* algorithm, and then we have computed the FOD map by setting the Spherical Harmonics term to 6. A probabilistic streamline tracking was performed with the optimized parameters (summarized in the table 2.1), including minimum length of 10 mm and Curvature angle of 45°. Cranial nerves were considered displaced by tumors when they were in contact with or pushed/encased by the tumor. The tracking parameters were adjusted using data collected from the first ten included patients to improve the tractographic aspect even if the predicted position was not modified. Thereafter, data were collected and analyzed prospectively.

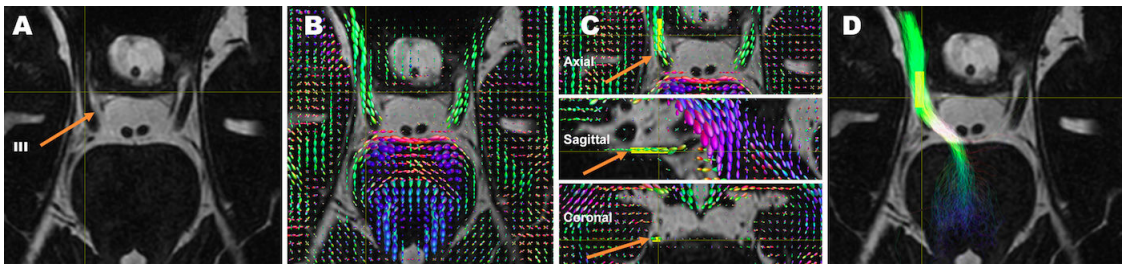

FIGURE 2.5 – **Strategy of the region of interest placement.** To overcome the residual distortion between anatomical and diffusion images at the skull base, the orientation distribution function (ODF) map was superimposed onto anatomical T2 sequence (A-B). For example, to track the right oculomotor nerve (orange arrow, A), a single ROI (in yellow) was used here with a volumic (cubic) shape. Its position was adjusted at the *best aspect* of the cranial nerve cisternal segment in the three dimensions : axial, sagittal, and coronal (orange arrows, C). The final reconstructed tracts show the cranial nerve trajectory from the brainstem to the skull base foramen (D).

Group	Nerve	ROI placement	FOD threshold	Number of fibers
1	Optic nerve	Whole Optic Chiasma	0,3	1000
2	Oculomotor nerve	Cisternal Segment	0,3	500
3	Trigeminal Nerve	Mid-Cisternal point	0,3	700
4	Abducens Nerve	Dorello canal entrance	0,2	100
5	Acoustic facial bundle	Internal Acoustic Canal	0,3	300
6	Lower nerves	Cisternal segment	0,2	200

TABLE 2.1 – Strategy of ROI placement and tracking parameters

Control and surgical validation

The reliability of tractography was assessed by comparing the healthy-side reconstructed tracts and cranial nerve cisternal trajectories on anatomical T2 images. The 'radiological' position of the displaced cranial nerve was compared to its ground-truth 'operative' position through direct visualization on the surgical microscope. The position of the acoustic facial bundle around the tumor used the six divisions described by Sampath et al. [82]. The concordance between the 'radiological' and the 'surgical' position of cranial nerves was determined using Cohen's Kappa coefficient and interpreted according to the Landis and Koch criteria ; the facial nerve was assessed alone since its positioning was more precise.

RESULTS

Patients

Sixty-two patients were included ; 36 were female, and the mean age was 51 years (SD : 15, range : 19 to 79). They presented various types of tumors : vestibular schwannomas (n=33) ; cerebellopontine angle meningiomas (n=15) ; arachnoid or epidermoid cysts (n=6) ; cavernous

sinus or lower nerves schwannomas (n=4) ; one chondrosarcoma ; one nasopharyngeal carcinoma ; one choroid papilloma, and one melanoma metastasis. The mean tumor size was 30 mm (SD : 12) while vestibular schwannomas were most frequently classified as Koos III (n=10) or IV (n=14). In view of operative risks, non-invalidating symptoms and the lack of radiological growth, 11 patients did not undergo surgery but were subjected to a “wait-and-see” attitude.

Tractograms

A total of 744 cranial nerves were tracked on both sides in the 62 patients. On the contralateral healthy side, all 372 cranial nerves were tracked. For each patient, at least one ‘displaced’ cranial nerve was not clearly identified on classical anatomical MRI images. Among the 175 displaced cranial nerves, 152 (87%) were successfully tracked, i.e. 23 of these nerves were not tracked. On the tumor side, the all cranial nerves not displaced were successfully tracked. Conditions that led to tractography failure (n=23) were : nerve encasement (n=11), cystic tumor (n=6), large tumor (n=4), and very small-sized nerve (n=2). Because of their thinness, the abducens nerve and the acoustic facial bundle were the more difficult to track contrary to the optic, the oculomotor, and the trigeminal nerves. Reconstructed fibers of cranial nerves always stopped at the entry of skull base foramina owing to a diffusion signal drop. No nuclei or segments were clearly identified in the brainstem either. Regarding the 52 acoustic-facial bundles displaced around tumors, the facial nerve was often distinguished and its most frequent position was anterior (n=17 ; 33%) or anterior-superior (n=14 ; 27%) according to Sampath et al.[82]

The posterior position was rare (n=4 ; 8%) and never concerned vestibular schwannomas. The facial nerve coursed within the tumor in one case and was unidentified in 7 cases. For cases of trigeminal nerve displacement (n=45), its most frequent positions were superior (n=25 ; 56%) and lateral (n=10 ; 22%) along the tentorium, while the lower nerves were mostly pushed inferiorly by tumors.

On the tumor side, the all cranial nerves not displaced were successfully tracked. Conditions that led to tractography failure (n=23) were : nerve encasement (n=11), cystic tumor (n=6), large tumor (n=4), and very small-sized nerve (n=2). Because of their thinness, the abducens nerve and the acoustic facial bundle were the more difficult to track contrary to the optic, the oculomotor, and the trigeminal nerves. Regarding the 52 acoustic-facial bundles displaced around tumors, the facial nerve was often distinguished and its most frequent position was anterior (n=17 ; 33%) or anterior-superior (n=14 ; 27%). The posterior position was rare (n=4 ; 8%) and never concerned vestibular schwannomas. The facial nerve coursed within the tumor in one case and was unidentified in 7 cases (Figure 2.6).

Surgical Strategy

On the basis of tractography, the surgical strategy was adjusted for 71% of the patients (n=44). The value of tractography was illustrated through several cases of the series (Figure 2.7).

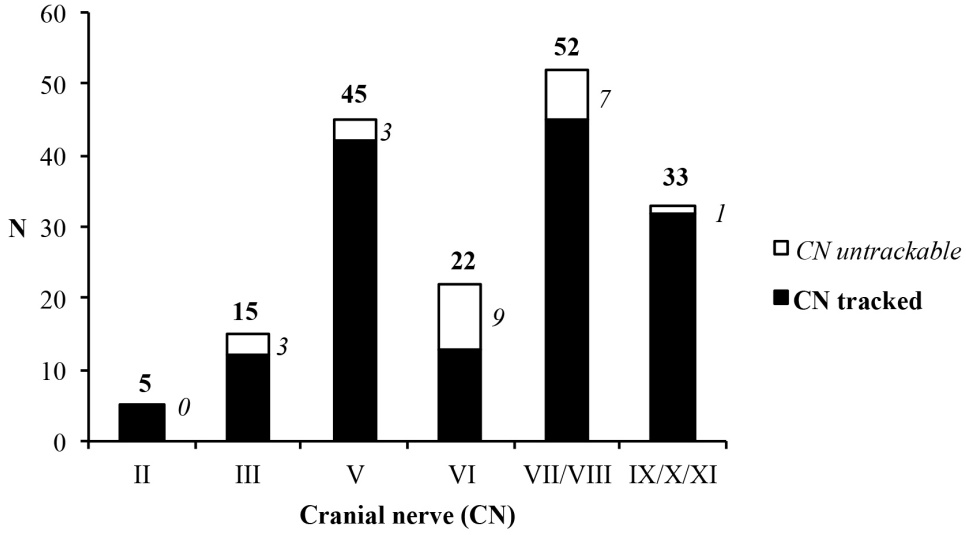

FIGURE 2.6 – The cranial nerves most frequently displaced around tumors were the acoustic-facial bundle, the trigeminal, and the lower nerves followed to a lesser extent by the abducens, the oculomotor, and the optic nerves. Regarding the 54 facial nerves displaced, their most frequent position was anterior-superior (n=17) and anterior (n=11), while seven facial nerves were unidentifiable.

The operative risk was considered too high and surgery was not performed for 7 patients. In these cases, tractography depicted one or more cranial nerves severely distorted or completely encased by solid tumors while tumor growth was no evident and poor symptoms. For example, an asymptomatic young man with a lower nerve schwannoma was directed to a radiologic follow-up. The same decision was taken for a 70-years old woman that presented a giant bilateral clival meningioma with multiple cranial nerve encasement and minimal clinic impact. A different surgical approach was chosen for 10 patients for which tractography revealed cranial nerve crossed the surgical path selected. This corridor was tailored not to cross cranial nerves, or as less as possible. As such, the tracked position of the trigeminal nerve within a petroclival chondrosarcoma led to prefer a lateral subtemporal approach rather than an anterior endoscopic transnasal one. In another case of choroid papilloma of the right cerebellopontine angle, tractography identified the lower nerves pushed superiorly against the acoustic-facial bundle, which helped both the craniotomy and the release of cranial nerves from the tumor capsule. In addition to most patients in which the approached was tailored, 27 patients had their tumor resection steps optimized thanks to tractographic inputs. For any type of tumor, to know the position of cranial nerves before operating allowed the surgeon to create a mental map of the patient's specific anatomy (tumor, cranial nerves, and environment) and then alternating fast safe debulking and high-precision dissecting of the cranial nerves attached to the tumor. The advantage of tractography was found

for almost all meningiomas (n=14), all cystic tumors (n=6), and all cavernous sinus or lower nerve schwannomas (n=4). Though, tractography helped the surgical strategy for only 19 of vestibular schwannomas (58%).

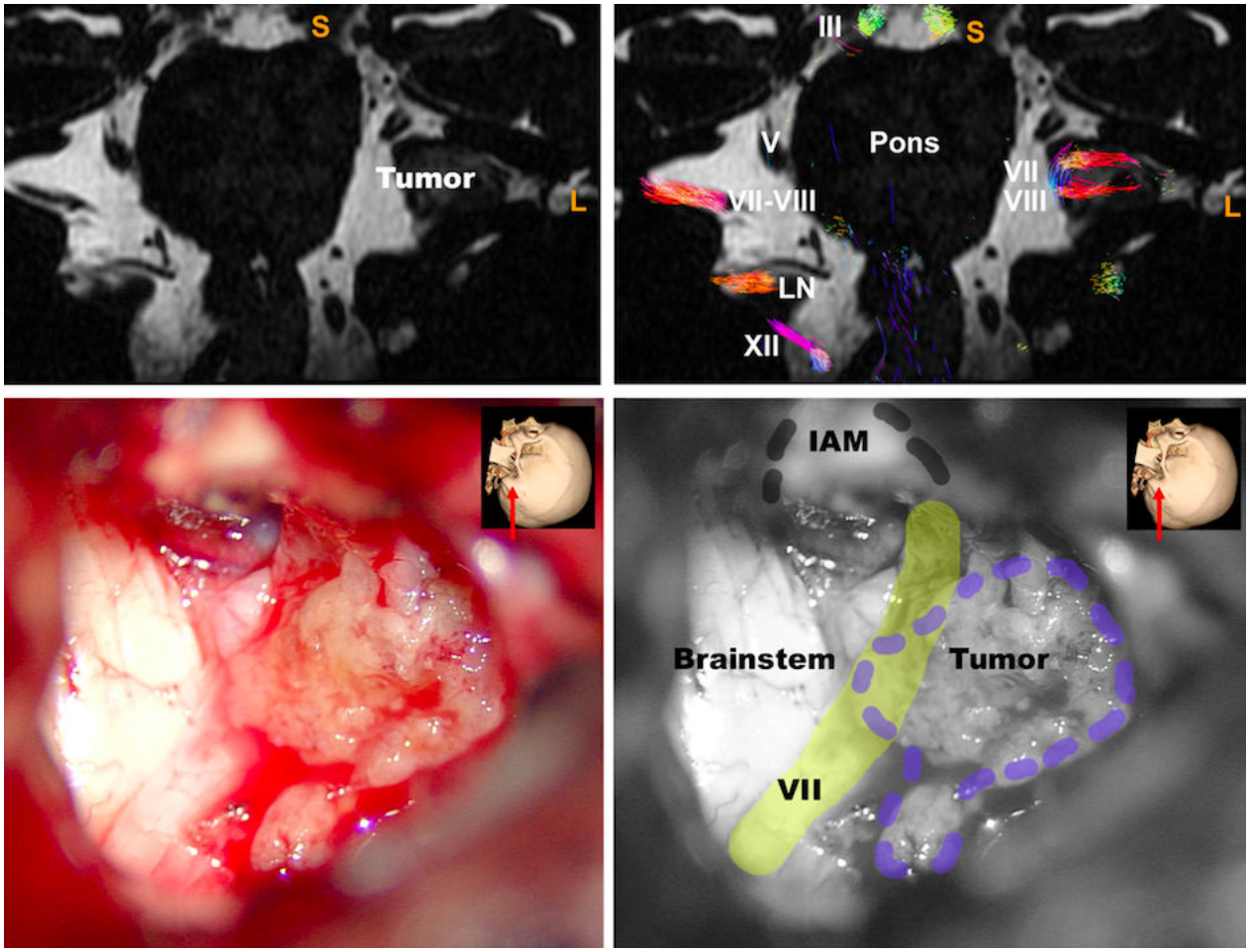

FIGURE 2.7 – A 42-year-old man presented with a left-sided hearing loss and tinnitus. The cerebral MRI found a large right Koos-3 vestibular schwannoma with significant brainstem contact. The acoustic facial bundle was not identified on classical T2 images while the trigeminal nerve was pushed superiorly and the lower nerves were in close contact inferiorly (axial view, A). Tractography depicted the acoustic facial bundle flattened at the anterior-superior tumor surface and confirmed the position of cranial nerves V and IX/X/XI (tractography overlaid on T2 sagittal views, B). Cranial nerves II to XII were correctly tracked on the contralateral healthy side except for the trochlear nerve. Because of the volume and the hearing status, a translabyrinthine approach was performed resulting in a gross total resection with perioperative confirmation of the anterior-superior position of the facial nerve by both visualization and electromyographic monitoring (microscopic view of the translabyrinthine approach and anatomical landmarks, C-D)

DISCUSSION

A new cranial nerve tractography insight

We designed an original study based on a large series of various skull base tumors using a probabilistic tractography algorithm to depict the elective position of cranial nerves 'displaced' by tumors and report how tractography helped the surgical strategy. Although 14 cranial nerve tractography case series were published between 2011 and 2017, they included little samples of patients (from 3 to 30) or healthy subjects. Among these studies, 10 attempted to predict the position of the single facial nerve in a single type of tumor : vestibular schwannomas. The remaining four tracked several cranial nerves in "skull base" or "cerebellopontine angle" tumors. Nine different tractography software packages were used. Most studies used a deterministic algorithm (n=11), however Zolal et al. and Behan et al. recently compared deterministic and probabilistic algorithms in case series of 5, 10, and 21 patients.[83, 84]. They concluded that probabilistic tractography yielded more accurate depictions of cranial nerves than deterministic methods[83] by avoiding the manual elimination of spurious fibers while conceding an increased calculation time.[84]. Despite a user-related and multi-step tracking process, the authors demonstrated the most accurate tracking of each cranial nerve detailing tracking parameters and ROI placement amidst anatomical landmarks in healthy patients. In addition, they successfully applied their method in 3 "skull base tumor" cases for which they were the only ones detailing the impact of tractography on the surgical strategy.

Optimization of the ROI design

We faced and overcame several challenges during the development of the tractography pipeline. For instance, distortions were frequent at the skull base because of the interface of different magnetic susceptibility tissues, eddy currents, and movement of the subjects' head. Even though a correction was performed thanks to "eddy" and "topup" tools of FSL® (FMRIB software library), a slight shift often persists between anatomical and diffusion images. Consequently, a ROI placed in the anatomical image could, in some instances, not correspond to the same area on the diffusion image. The tract reconstruction could thus provide false continuations or misleading information. We used the T2 anatomical map superimposed on the ODF map to visualize both anatomical landmarks and local fiber orientations (ODF) on which the tracking was initiated. Our strategy was then to draw ROIs at the point where each nerve can be best seen regarding its cisternal segment in the three dimensions. The ROI shape was a volume (cube) and its size was tailored to the anatomical feature of each nerve : not too small as to avoid missing fibers and not too big so as to prevent recruitment of other cranial nerves or pontocerebellar tracts. Likewise, the ROI placement should not be too medial or too lateral to avoid either recruitment of brainstem fibers or a drop of the diffusion signal.

To conclude, **probabilistic tractography showed a promising ability to predict the position of displaced cranial nerves around skull base tumors.** Along with advances in imaging acquisition, reconstruction methods, and tridimensional rendering of the anatomical environment, this technique could be an effective tool in routine surgical practice.

2.2 Spectral Clustering-based Tractography

2.2.1 Introduction : General concept in Diffusion-Weighted Imaging

The main advantage of streamlines tractography is the possibility to evaluate the whole fiber bundle, as opposed to just one of its segments as is the case with voxel-based analysis (VBA). However, we have the feeling that relevant anatomical information for fiber pathways were always present by direct visual study of the Fiber Orientation Distribution (FOD); which describes the orientation dependence of the diffusion-weighted MR signal. In addition, we have shown that tractography process presented with technical limitations both in normal and diseased condition for mapping cranial nerves.

The constrained spherical deconvolution (CSD) method can reconstruct the FOD in a robust way with MRI protocols that can be used in clinical practice [76, 77]. The diffusion signal S(θ, ϕ) is modeled by the convolution of the FOD with a kernel that represents the DW signal corresponding to a single fiber orientation. The FOD is then "deconvolved" from the DW signal using this kernel, coined the response function (RF). This can be expressed as the convolution over the unit sphere of the RF (θ) with a FOD $F(\theta, \phi)$.

$$S(\theta, \phi) = F(\theta, \phi) * RF(\theta)$$

This diffusion model assumes prior hypotheses such as a negligible effect of exchange between compartments during the MRI acquisition, or an isotropic signal for tissues such as the cerebrospinal fluid (CSF) or the grey matter. CSD enables estimation of the apparent fiber density (AFD), a scalar value which reflect the intra-axonal volume fraction [85, 86]. AFD is a quantitative measure related to fiber density derived from FOD images computed from single-shell or multi-shell DWI. It has the advantages of being proportional to the intra-axonal volume of axons aligned in that direction under certain conditions, such as DWI sequence b-value, factor typical diffusion pulse duration, typical axon diameters, global intensity normalization, and a group average spherical deconvolution response function. With this regard, extracting FOD along nervous structures may help to better characterize neuronal injury by estimating the fiber orientations and their volume fractions directly.

Machine learning algorithms have the potential to capture or mimic the reduced embedding space of FOD for performing robust clustering methods. Previous studies have proposed to characterize the brain white matter architecture extracted from DWI data using fingerprint building at the level of fiber trajectories [87]. Yet it still relies on tractography postprocessing with related effects, such as fiber tracking or registration errors. We propose to alternatively map the white matter architecture using spectral clustering (SC) algorithms on FOD maps. SC has become one of the most popular modern clustering algorithm. It outperforms traditional clustering algorithms such as the k-means algorithm. SC represents the observations as an

undirected similarity graph. The clustering problem becomes a graph partition problem that can be solved with the estimation of the Laplacian matrix and using the spectral graph theory. The underlying idea is to construct similarity graphs that represent the local neighborhood relationship between observations. SC algorithm has been applied to DTI major eigenvector of the diffusion tensor [88] and more recently for parcellation of Human Amygdala Subfields using spherical harmonics estimation of the Diffusion-Weighted signal [89].

2.2.2 Preliminary study : Test-Retest of Spectral Clustering-based Tractography for corpus callosum study

Machine Learning application in clinical imaging requires robust and reproducible metrics extraction. Within the field of brain connectivity, there is growing interest in corpus callosum (CC) analysis. Fascicles that emanate from cortical area into the white matter comprises two major elements. One segment is destined for subcortical structures, and the other for the commissural fibers directed toward the opposite hemisphere. A distinct topography is present within the CC that connects most of the neocortical areas. Elucidation of the topographical location of the callosal fibers in the mid-sagittal plane is important for understanding the organization of this preeminent interhemispheric system. It is directly relevant also in a number of clinical situations, including epilepsia, trauma or brain malformation.

The intra- and inter-subject reproducibility of the AFD coefficient, as extracted from VBA, have been shown as reliable in a small subset of patients with single-shell DWI acquisition, because it does not require tracking, opposite to Track-Weighted Imaging techniques [90]. Parameters related to fiber density can also be extracted for individual fiber populations within each voxel, named "fixel based analysis" in the literature [85, 86]. However, fiber pathways generation requires streamline tractography, which is highly dependent on setting parameters such as the curvature angle or the FOD amplitude threshold for initiating/terminating the tracking process. Since probabilistic streamline tractography is the only available method to extract anatomically meaningful structural information, new methods could be proposed to benefit from the reproducibility of the AFD coefficient.

Here we intend to characterize the reproducibility of the CC spectral clustering-based tractography, in order to investigate the within-subject and between-subject variability. In particular, both intra- and inter-subject AFD values extracted from the CC are considered, in order to investigate the within-subject and between-subject variability.

METHODS

Population and Data acquisition

MRI data were acquired on a Siemens 3T Prisma system (Erlangen, Germany). Two different experiments were carried out. In the intra-subject experiment 1, 45 DWI datasets were acquired

in 15 healthy subjects (mean age 20,1 years old, +/- 2,95 (Standard Deviation) over three sessions, two in the same day one 12 months after. In the inter-subject experiment 2, a DWI dataset was acquired for each of 15 healthy subjects. Informed written consent was obtained in accordance with ethical approval from the local Human Research Ethics Committee.

In addition to 10 non-DWI volumes (which were averaged), 3 DWI shells were acquired, each with a different diffusion weighting and a unique set of diffusion-weighted directions. The set of directions was independently generated for each shell by electrostatic repulsion, as follow : A°/ 60 directions, b = 2000 s/mm^2 B°/ 15 directions, b = 800 s/mm^2 C°/ 10 directions, b = 300 s/mm^2

Other parameters of the diffusion sequence were : single-shot spin-echo sequence ; TE/TR= 80/4700 ms ; voxel size : 1,5 mm3 ; x 99 slices (1,5 mm slice thickness, no gap) ; Scan Time= 7'31", Multiband factor= 3.

Preprocessing

Preprocessing of diffusion-weighted images included denoising of data [91], Gibbs artifacts' corrections, eddy-current correction and motion correction [81] bias field [92], and up-sampling DWI spatial resolution by a factor in all three dimensions using cubic b-spline interpolation, to a voxel size of 1.3 mm3 [93]. We have estimated fiber orientation distributions using the Constrained Spherical Deconvolution model [77] using a group average response function (RF). We have computed using multi-tissue 3-tissue CSD variants [94]. All preprocessing steps were conducted using commands either implemented within MRtrix3 (www.mrtrix.org), or using MRtrix3 scripts that interfaced with external software packages. Spatial correspondence was achieved by first generating a group-specific population template with an iterative registration and averaging approach using FOD (Fiber Orientation Distribution) images from all the controls. Each subject's FOD image was then registered to the template via a FOD-guided non-linear registration [93].

Postprocessing

We derived the AFD metric from the FOD maps [85] with the spectral clustering method. The voxel-wise mean AFD is given by the mean of the FOD. Our proposed strategy was to firstly extract FOD amplitudes along a sample of 100 spatial directions per voxel. The directions were generated using a set of uniformly distributed directions using a bipolar electrostatic repulsion model, as provided by MRtrix. The energy of the system is determined based on the Coulomb repulsion. FOD amplitudes are physically meaningful metrics, sensitive to the rotation of FOD shape and can be easily extracted without manual supervision. FOD amplitudes S in the $\vec{g}_i$ direction can be estimated with the different spherical harmonics $Y_{l,m}$ of degree l, and order m and its corresponding $c_{l,m}$ coefficients :

$$S(\vec{g}_i) = \sum_{l \leq N, |m| \leq l}^{N} c_{l,m} Y_{l,m}(\vec{g}_i)$$

SC-based Tractography procedure follows these steps : firstly ; a NxN matrix of pairwise similarities (i.e. the Euclidean distance) between N observations with M dimensions was calculated. Indeed, we consider a graph where the vertices's are the observations and the edges are weighted by the similarity values. Then a Laplacian matrix L is estimated. Spectral clustering finds the m eigenvectors N×m corresponding to the m smallest eigenvalues of L (ignoring the trivial constant eigenvector) with m ≪ M. These eigenvectors define the feature vectors for each object. Using a standard method like K-means, we have then clustered these low dimensional eigenvectors to yield a clustering of the original data points.

Since SC requires the number of clusters to be specified, we have firstly drawn a large mask on anatomical region of the CC before the specification of two clusters based on the provided amplitudes. We have systematically obtained one cluster for the background, automatically selected as having the lower mean AFD value ; and one for the CC, with the higher value for mean AFD in the cluster. We have then extracted AFD from the Cluster of this anatomical structure at each session (Figure 2.8).

Statistical analysis

We have firstly studied the visual representation of the CC cluster in comparison with T1-weighted imaging. To test the efficiency of the clustering, we evaluate the reproducibility of the obtained clusters in terms of shape and homogeneity. For the shape comparison, we use the classic Dice metric for the patient j defined as $Dice(j) = \frac{2|ROI_1^j \cap ROI_2^j|}{|ROI_1^j| + |ROI_2^j|}$ where || represent the cardinal of the set of voxels, and ROI_i^j represent the obtained clusters for the acquisition i and the patient j. We further consider the CC cluster for the homogeneity evaluation, and evaluate the mean of the AFD over the ROI. The considered metrics are the Intra Class Correlation (ICC) coefficient and the Bland-Altman plot. The ICC measure corresponds to the ICC(3,1), as extracted from the reference article [95].

Results

The CC cluster includes 633 voxels. The SC algorithm has a processing time between one and ten seconds per subject, systematically producing a cluster for the CC structure on the mid-plan that can be overlaid on the CC representation on T1-weighted images.

Space reproducibility for sessions 1 and 2 : the mean of the $Dice(j)$ over the control group is $0.95 +/- 0.04$. This score displays a very good reproducibility. Only one patient has CC two clusters slightly different in term of shape. Homogeneity reproducibility for sessions 1 and 2 : The ICC of the AFD mean values over the CC ROI is 0.98, which corresponds to a very high reproducibility.

Space reproducibility for sessions 1 and 3 : the mean of the $Dice(j)$ over the control group is $0.88 +/- 0.07$. This score displays a very good reproducibility in term of shape. Only one patient has two clusterings slightly different. Homogeneity reproducibility for sessions 1 and 3 : The ICC

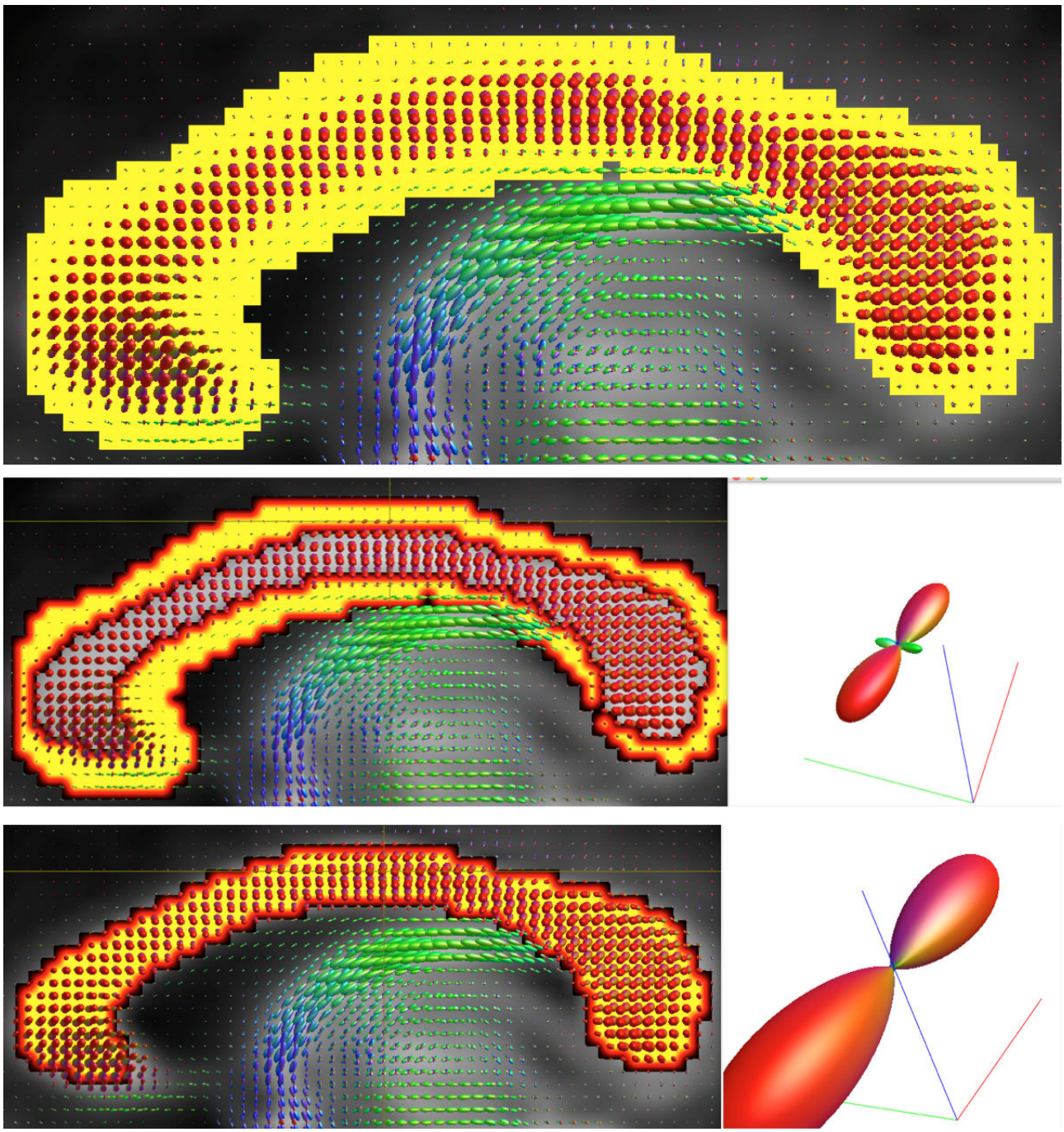

FIGURE 2.8 – Illustration of Corpus Callosum Spectral Clustering process (A : Mask of interest, B : Background cluster, C : CC cluster). The initial mask is divided into two clusters, the first one includes background voxels with smaller FOD amplitudes while the second one CC clusters with more important FOD amplitudes.

of the AFD mean values over the CC ROI is 0.76 which corresponds to a high reproducibility.

However, a high correlation score does not necessarily imply a good agreement between

the two acquisitions [96]. Consequently, we have displayed the Bland-Altman plots, where we calculated the difference of the two measurements against the mean of them. The Bland-Altman plots show a good reproducibility with no proportional bias in the measure. This indicates that the method do not agree equally through the range of measurements (Figures 2.9 and 2.10).

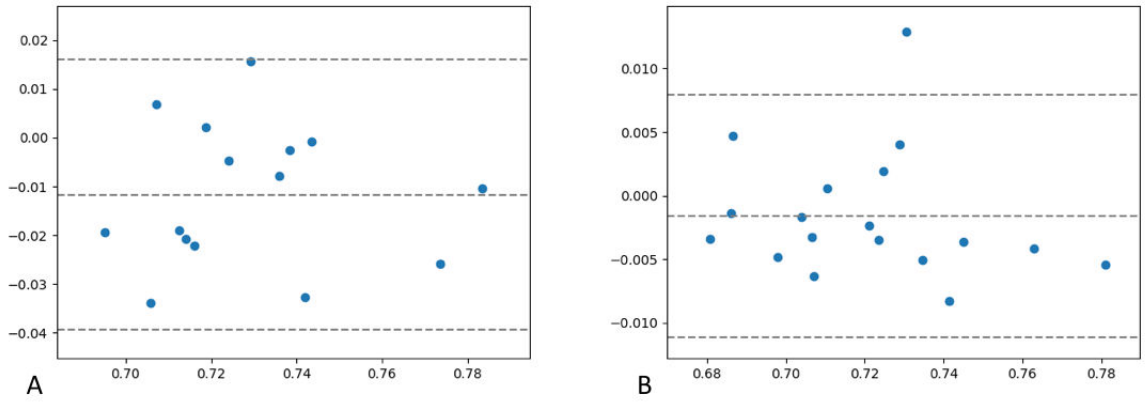

FIGURE 2.9 – Bland-Altman diagram showing high reproducibility between AFD values extracted from Spectral-Clustering of the Corpus Callosum between Session 1 and Session 2 (same day). The abscissa (x-axis) value and the ordinate (y-axis) value respectively correspond to the mean of the two measurements and the difference between the two values.

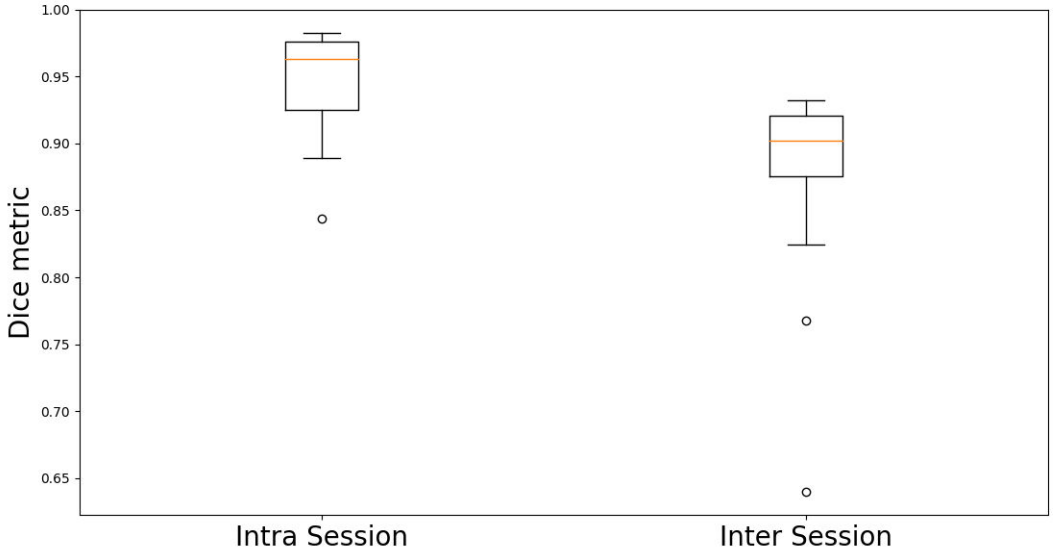

FIGURE 2.10 – Intrasession and Intersession DICE metrics for spectral-clustering based extraction of the corpus callosum.

Discussion

Here we have evaluated the robustness of the SC to extract the CC structure (ie. commissural fibers) in the brain mid-plane using a test-retest procedure, based on the total AFD metric quantitative longitudinal evaluation. SC tries to capture the intrinsic structure of the data by focusing on the local neighboring to estimate new geodesic distances between observations. In mathematics, this is a rough approximation of the Riemannian space of FODs in a large white matter fascicle. However, the true estimation of Riemannian space is complex and need to design specific metric [97], not adapted for further application in clinical studies. A major strength of the presented algorithms is the ability to deal with various metrics extracted from the diffusion signal. Here the high reproducibility of quantitative values between sessions in healthy controls is promising for application in diseased condition such as for example mild traumatic brain injury. We raise the hypothesis that in cases with trauma, ischemia or demyelination of the CC, either visual analysis of the CC clusters or quantitative extraction will ease automatic detection of commissural injuries.

Metrics describe distances in a parameter space and are characterized by their sensitivity and specificity towards the differences in the physical quantities that they are meant to reflect. Spherical deconvolution translates, for each voxel, the direction-dependent signal attenuation into FOD [77]. Here the AFD metric is derived from FOD images computed from multi-shell DWI and refers to the mean of the fODF, expressed as a scalar value. The use of a dedicated response function for the white matter improves the role of AFD as a quantitative biomarker with an amplitude proportional to the intra-axonal volume of axons aligned in that direction [85].

However, scalar values voxel-based analysis to distinguish voxels with tissue mainly composed of CC from other tissues can be limited with an unique coefficient, and extracting the geometrical structure of FODs from 100 directions with optimal distribution seems efficient to characterize tissue-based clusters. Spectral clustering has a broad range of applications including 3D image analysis [98]. In the absence of training data with labeled clusters, help from a human analyst is required to decide the number of clusters.

We propose to simplify this process by only keeping two clusters. We determined the cluster including the CC commissural fibers by selecting those with the higher AFD value. We support the hypothesis that voxels with CC fibers have more consistent intracellular compartment than surrounding tissues that can contain CSF in the ventricle for example. Visual analysis of the cluster location provides immediate feedback to support the required decisions. Parcellation of human amygdala subfields Using spherical harmonics representation of the Diffusion Signal and Spectral Clustering method has already been tested [89]. In that study, the spherical harmonics coefficients were used instead of amplitudes in our work. Here we group together voxels within the CC according to the similarity of their amplitude to increase the robustness with the 100 coefficients per FOD, opposite to SH coefficients where the first one has a relative important

weight in comparison with the 44 others, given that we have performed CSD estimation with a degree lmax=8.

The SC reproducibility results in term of shape and homogeneity is high for both intra and inter-session. In addition, our results confirm the robustness of the AFD coefficient over time, as previously published [99]. We have included twice the number of subjects for the AFD measures using multi-shell acquisition. This is useful for further clinical research with quantitative application.

The reproducibility of the AFD quantitative values over the 3 MRI sessions in a population of young controls hold promise for the Spectral Clustering method, before application to brain and/or cranial nerve disease process. As a limitation, in the lack of disease model, we have difficulties in evaluating the potential added value over classic streamline tractography analysis to extract anatomical region of interest.

2.2.3 Meniere's Disease cranial nerves' alteration : a Spectral Clustering-based Tractography study

Cranial nerves streamline tractography has captured the imagination of radiologists and clinicians because it has the ability to generate visual information from living subjects noninvasively. Although tractography is often used to investigate brain anatomical connectivity, its application for cranial nerves has specific challenges owing to the following factors :

— The small diameter of the cranial nerves structures (between 0.1 mm and 5 mm [100, 101]), in the context of limited acquisition voxel size of the DWI sequence, often set between 1.5 mm and 3 mm isotropic for clinical application.

— The tendency of probabilistic algorithms (although they are more reliable [83, 84] than deterministic algorithms) to overestimate the cranial nerve size. In cases of physiological vicinity between two nerves, such erroneous estimation of the nerves' size can hinder the quality of the visual information for presurgical planning [70]. The necessity to set track parameters for each session (including regions of inclusion/exclusion, the curvature angle and the FOD amplitude threshold for initiating the tracking process) has been demonstrated to be a major cause of inter-subjects variability for cranial nerves tractography [70, 102]).

— Cranial nerves run through an intricate anatomical environment sensitive to susceptibility and movements' artifacts. The use of robust processing tools to manage such artifacts increases the quality of DWI data, yet local area of signal-to-noise ratio (SNR) loss may theoretically lead to incorrect estimation of the FOD shape. Susceptibility artifacts at the air/bone interface may produce spurious FOD lobes, making difficult the acquisition of multi-shell MRI sequences with adapted correction of such artifacts.

— The close contact between brain and cranial nerves' voxels can be problematic in terms of performing a tractogram on the whole volume. In the particular case of the Constrained Spherical Deconvolution (CSD), the need to infer the FOD from the measured DWI signal given a suitably calibrated response for a fiber population poses problems for cranial nerves exploration. All spherical deconvolution methods require an estimate of the single-fibre response function (RF). Given the potential differences in the DWI signal between large white matter fascicles and small cranial nerves, one can consider that using algorithms specifically dedicated to the brain would lead to a poorly adapted fixed RF for tracking the nerves, particularly at low b-values.

The necessity of setting various parameters with probabilistic tractography is crucial in the context of cranial nerves exploration since there is no algorithm other than streamline tractography to map their intracranial course with DWI data. When studying normal cranial nerves in the skull base, particularly cisternal segments, there are reasons to believe that

assuming the absence of perpendicular secondary branches, the voxels will contain a single fiber population. This could enable adjacent voxels to be merged after extraction of adapted metrics from the FOD. Spatially distant voxels along the acoustic-facial bundle can share the same underlying anatomy, yet adjacent voxels may share no anatomy (for example cerebro-spinal fluid (CSF) of the inner auditory canal and temporal bone). The objective of a new tractographic approach would be to cluster voxels along a fiber tract, without all voxel neighbors isotropically. The spectral clustering (SC) algorithm has been used for automatic tractography segmentation, allowing to identify white matter regions across hemispheres and across subjects [103]. To the best of our knowledge, SC has never been used for mapping cranial nerves.

We have written a scientific article to compare classic streamline tractography with spectral clustering-based tractography, to assess the robustness of each method in mapping the acoustic-facial bundle in volunteers. We then applied our algorithm in a study of patients with Meniere's disease, in which immune modification of the nerves is presumed to affect the fiber density.

METHODS

Healthy subjects and Patients

This was a single center parallel-group imaging study that was registered with the ClinicalTrials.gov registry (38RC14.428 for healthy subjects / 38RC15.173 for patients). Signed informed consent was obtained from all subjects. Eighteen patients and 21 healthy volunteers were recruited between August 2015 and May 2018. Healthy subjects were aged 40 or over, with no history of inner ear disorders were consecutively included in this study. Patients were aged 40, with a definite clinical diagnosis of MD based on the latest American Academy of Otolaryngology – Head and Neck Surgery guidelines [3]. All patients presented with Probable or Definite Meniere's Disease, which was explored using delayed acquisition 3D-FLAIR sequence to look for saccular endolymphatic hydrops [18].

MRI acquisition

Imaging examinations were carried out on a 3T Philips Achieva® TX MRI scanner equipped with Quasar Dual gradients and with a 32-channel SENSE head coil. For the diffusion-weighted acquisition, we used a b-value of 1000 s/mm2 and 60 diffusion-weighting non-collinear directions distributed over four scans, each with 15 directions and one b=0 s/mm2 acquisition. Each 15 directions-subset used a method for generating orientation acquisition schemes that yielded an optimal spatial distribution of the orientations [104].

Other parameters of the diffusion sequence were : single-shot spin-echo sequence ; echo time/repetition time TE/TR= 89/3300 ms ; acquired field of view of 224x224 mm2, voxel size : 2x2 mm2 ; 26 slices (2 mm slice thickness, no gap) ; SENSE factor= 1.9 ; NSA (number of signal averages) =2 ; nominal matrix 112x111 ; A-P ; water-fat shift of 15 pixels ; scan duration of 2'21" per 15 direction scan (a total of 9'24"). To minimize movement, subjects were instructed to sight a

fixed reference point using the head coil mirror.

Preprocessing

For each subject, a single multiplicative bias field was estimated using the b=0 s/mm2 images. Intra-scan and inter-scans movements of the subjects were estimated and corrected. Preprocessing of diffusion-weighted images included denoising of data [91], correction of Gibbs artifacts' [92], eddy-current correction and motion correction [81] bias field correction and and up-sampling of DWI spatial resolution by a factor in all three dimensions using cubic b-spline interpolation, to a voxel size of 1.3 mm3 [93]. All preprocessing steps were conducted using commands either implemented within MRtrix3 (www.mrtrix.org), or that use MRtrix3 scripts that interfaced with external software packages. Spatial correspondence was achieved by first generating a group-specific population template with an iterative registration and averaging approach using FOD images from all the healthy subjects (controls). Each subject's FOD image was then registered to the template via a FOD-guided non-linear registration [93].

We have estimated FODs using the Constrained Spherical Deconvolution (CSD) model [77] using a group average RF as estimated with the *FA* algorithm. As a reminder, the signal S(θ,ϕ) that would be measured from a sample containing several distinct fiber populations is given by the sum of the RF R(θ) of each population, weighted by their respective volume fractions, and rotated such that they are aligned along their respective orientations. In terms of the bipolar electrostatic repulsion model, the DWI gradient directions had average nearest-neighbour angles of 12°, supporting a number of spherical harmonic terms with lmax=6. We have previously computed in the template an adapted skull base mask encompassing the inner auditory canal. In a preliminary study, we have compared recently developed *Tournier* algorithm with the *FA* algorithm in the control population (21 volunteers). These algorithms were adapted for single shell diffusion modelling. The same voxels mask was used to estimate the RF (Figure 2.11).

Postprocessing

We have evaluated whether it was possible to reconstruct the acoustic-facial bundle using seed region of interest (ROI) streamline tractography with previously published parameters, including FOD amplitude set to 0.3 and 300 selected fibers [70] for both RF. However, The FOD amplitude along the nerve, as estimated with the *Tournier* RF algorithm, did not allow such a tractography process to be performed to the high FOD amplitude cutoff being to high. In addition, when setting similar FOD scaling amplitudes for each RF (for the purposes of comparison), we noticed abnormal estimation of the acoustic-facial bundle FOD shapes in the fundus of the inner auditory canal with this algorithm (Figure 2.12). We confirmed that this was not possible to perform the tractographic process with the *Tournier* algorithm by decreasing the FOD amplitude cutoff in the *tckgen* command. The results were spurious tracks without anatomical consistency.

The difference between the *FA* and *Tournier* algorithms centers on the selection of the best

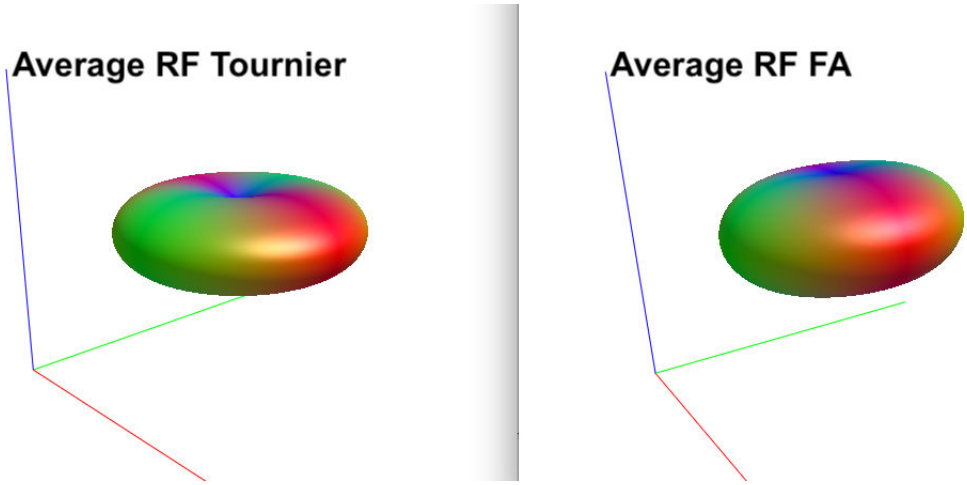

FIGURE 2.11 – **Comparison of the group average response function, as estimated from the *FA* and *Tournier* algorithms.** The 3D view is theoretically more suitable for performing spherical deconvolution with the *Tournier* algorithm.

voxels to estimate the RF. The former estimates the RF from the 300 voxels with the highest Fractional Anisotropy value in an eroded brain mask whereas the second algorithm is initialized by a sharp lmax=4 RF [105]. The *Tournier* algorithm has a bias towards FODs with a larger tallest peak, to avoid favouring low SNR FODs. In the context of cranial nerves, it appears that this algorithm is not adapted to estimate the smallest FOD peaks.

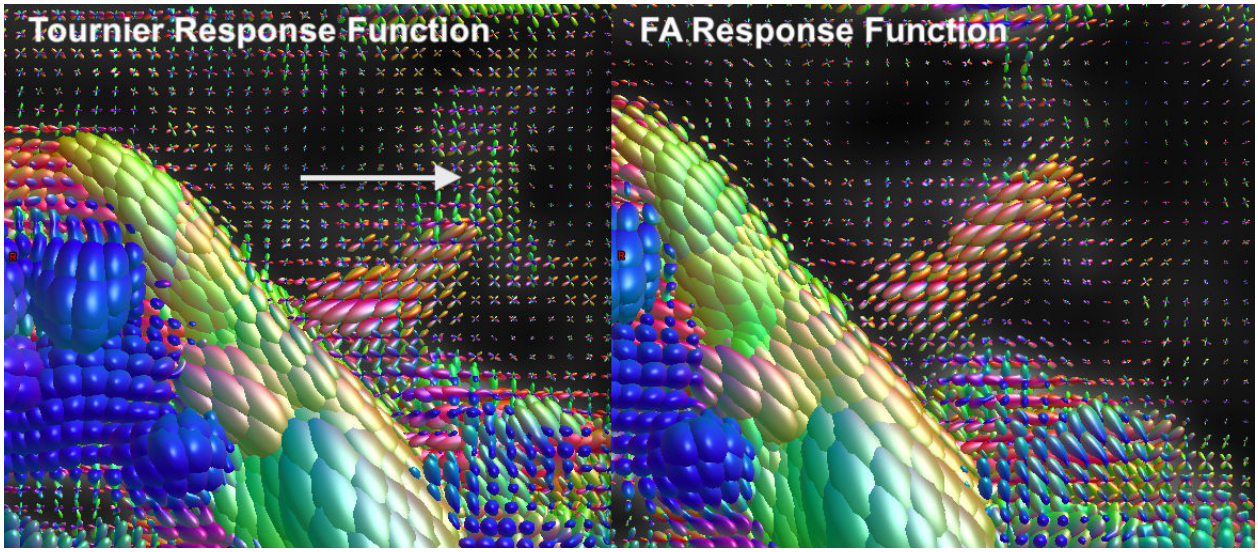

FIGURE 2.12 – **FOD estimation along the acoustico-facial bundles using 2 different RF estimation.** The spherical deconvolution process, as estimated using *Tournier* algorithm, failed to estimate the Fiber Distribution of the acoustic-facial bundle in the fundus of the auditory canal. By contrast, the *FA* algorithm produces an adapted estimation of single fiber voxels.

(Figure 2.13)

The *FA* algorithm will be used for subsequent group average estimation and analysis.

Extraction of FOD metrics

We calculate the mean apparent fiber density (AFD) [85] from the FOD maps over the ROI obtained with the SC. The considered voxel-wise AFD metric is the mean of the FOD and refers to the volume of the intra-axonal compartment per unit volume of tissue and was recently demonstrated to be feasible at relatively low b-values [106]. According to this framework, a quantitative measure of AFD can be derived from FOD images, given that the integral of the FOD along a particular direction is proportional to the intra-axonal volume of axons aligned in that direction. In the particular case of the acoustic-facial bundle, we assume that the directional AFD is equivalent to the total AFD, given the single fiber population. We have also combined the AFD with the number of tracks to obtain another measure of AFD weighted by the number of streamlines in all acoustic-facial bundle voxels (AFDw). AFDw is similar to the AFD coefficient except that voxels with the high numbers of fibers, as estimated using the local tractography process, contribute more than others. This enables correction of the classic dispersion of tracks in these regions of low SNR, in the absence of exclusion ROIs and at the template level.

Spectral Clustering-based Tractography

Firstly ; a NxN matrix of pairwise similarities (that is, the Euclidean distance) between all observations in dimension M was calculated. This is analogous to consider a graph in which the vertices's are the observations and the edges are weighted by the similarity values. Then a Laplacian matrix L was estimated. Spectral clustering algorithm finds the m eigenvectors N×m corresponding to the m smallest eigenvalues of L with m « M (ignoring the trivial constant eigenvector). Using a standard method like K-means, we have then clustered the eigenvectors as the new feature vector for each N observations of dimension m to yield a clustering of the original data points.

We next generated vectors of noise-free DW signals using the amplitudes of the full set of SH coefficients as estimated below :

$$S(\vec{g}_i) = \sum_{l \leq N, |m| \leq l}^{N} c_{l,m} Y_{l,m}(\vec{g}_i)$$

We have evaluated the amplitude of images of spherical harmonic functions along 100 specified directions. Uniformly distributed directions were generated using a set of using a bipolar electrostatic repulsion model, as provided by MRtrix. The energy of the system was determined based on the Coulomb repulsion. As SC requires the number of clusters to be specified, we drew a mask on the inner auditory canal before the specification of two clusters based on the provided amplitudes. We systematically selected one cluster for the background (the lower mean AFD value was automatically selected), and one cluster for the nerve (the higher mean AFD value) (Figures 2.13 and 2.14).

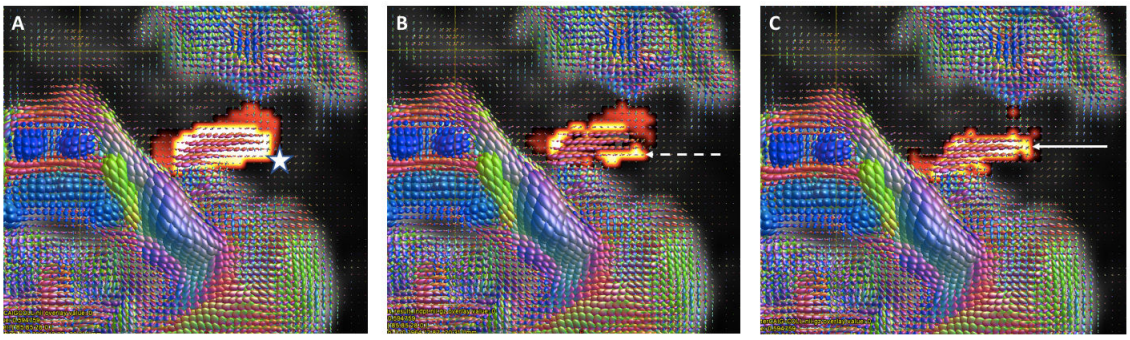

FIGURE 2.13 – **Method of Spectral-Clustering based tractography for the acoustico-facial bundle.** A : After spatial registration, we have drawn an unique region of interest on the inner auditory canal around the nerve's FOD in the template (white Star). B : For each subject, we have obtained two clusters. The first one (B) represents the background, here the temporal bone (dotted arrow). The second cluster (C) represents the acoustico-facial bundle (white arrow).

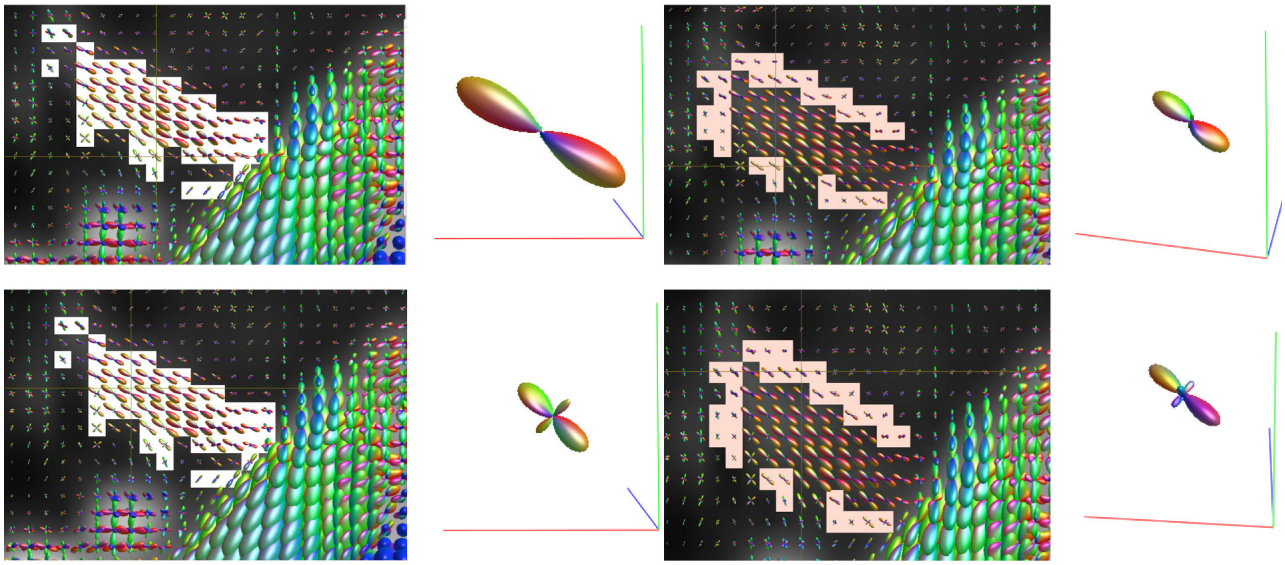

FIGURE 2.14 – **Illustrative example of the two spectral clusters.** The white cluster is presumed to include FODs along the acoustico-facial bundle while the pink cluster include peripheral FODs of the background. In some cases the former cluster may also include voxels with crossing fiber population (bottom left) and the later cluster voxels with single fiber population (upper right)

Streamlines tractography process

An acoustic-facial bundle tractogram was generated using probabilistic tractography for each individual after spatial registration. The coordinates for local tractography were defined at the template level and one local tractography process was performed per subject. One thousand streamline were generated using the 'unidirectional' function, between the brainstem and the

inner auditory canal fundus with spherical ROIs of 3 millimeters. We have subsequently filtered to 100 streamlines using the SIFT (spherical-deconvolution informed filtering of tractograms) algorithm [107] to reduce reconstruction biases (Figure 2.15). We have then used the track-weighted imaging framework [108] to produce images of the tracks at original resolution. Finally, we have extracted from the track masks the total AFD value per voxel using the l=0 term of the CSD estimation.

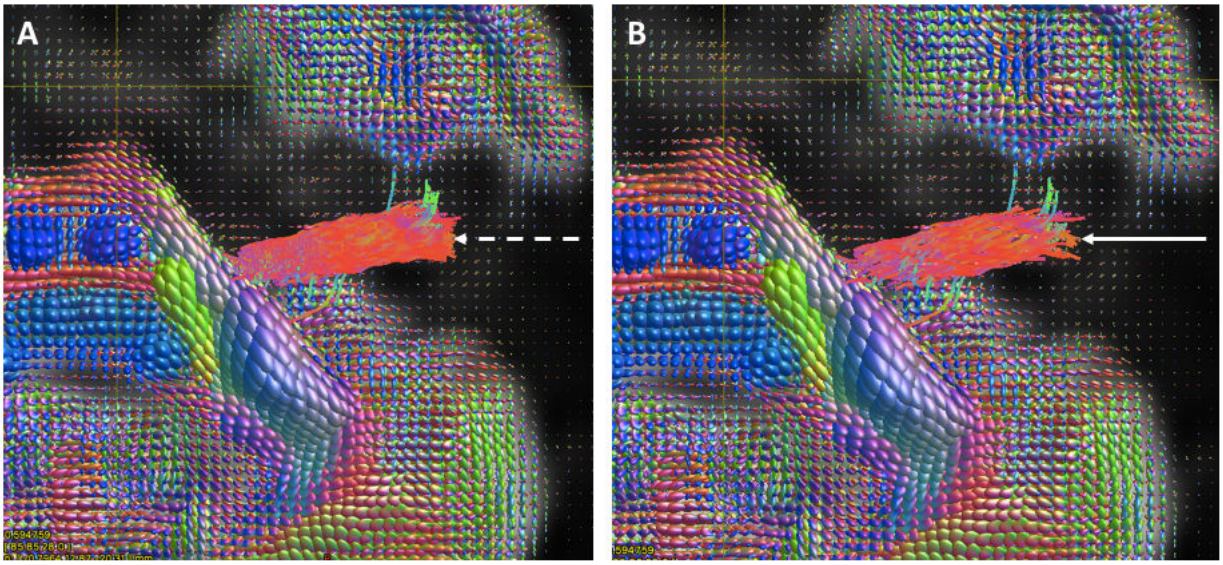

FIGURE 2.15 – **Method of streamline tractography for the acoustico-facial bundle.** A : We have selected 1,000 tracks using two regions of interest : in the root entry zone of the acoustic-facial bundle near the brainstem and in the fundus of the inner auditory canal (dotted arrow). B : We have selected 100 of these fibers using a filtering process (white arrow).

Statistical analysis

We performed tract of interest analyses to investigate potential alteration of acoustico-facial bundle in patients with Meniere's Disease, who were potentially at risk of later developing sensorineural hearing loss in one or both ears. Two tracts of interest analyses were performed :

(i) comparing the spatial distribution of tracks' masks extracted from the SIFT algorithm with those extracted from the SC-based tractography. The reference was the anatomy of the acoustic-facial bundle, which is known to run from the brainstem to the inner ear labyrinth for the cochleo-vestibular nerve and to continue through the temporal bone for the second portion of the facial nerve.

(ii) comparing the quantitative distribution of AFD and AFDw values of the acoustic-facial bundles extracted from the two methods in both patients and controls.

Between-group comparisons were analyzed with the Student's t-test to assess significant

differences in the average AFD and AFDw values between controls and patients and between left and right sides. The difference in mean age between healthy participants and patients was tested using a t-test. We calculated correlation between the age and the AFD values between groups and within subjects using Pearson correlation. We set a significance threshold (p-values) of $p<0.05$.

Results

Twenty-one healthy subjects (13 of whom were women) were included in this study, with a mean age of 58.7 ± 10.86 years. Eighteen patients were included (15 of whom were women), with a mean age of 54.23 ± 12.86 years. Patients referred with unilateral Meniere's disease, 13 on the left side and 5 on the right side, and the diagnosis was confirmed using criteria from the AAO-HNS guidelines. 3 healthy volunteers were excluded because of susceptibility artifacts in the internal auditory canal making impossible to draw ROIs of interest on the FOD maps. 10 patients presented with saccular hydrops, always on the symptomatic sides. There was no significant difference in the mean ages of the healthy and patient groups. Ten out of the 18 patients were found to have endolymphatic hydrops on investigation using delayed acquisition FLAIR, as described above [18].

Visual analysis

Using streamline tractography, the bundle always occupied the whole auditory canal and 8 subjects (out of 39, including both volunteers and patients) presented with dispersion of the tracks after the anatomical end of the nerve, located in the brain temporal lobe. In 5 subjects out of 39, the setting of the initial ROI led to dispersion of the tracks in the brainstem or in the cerebellum. Using the SC algorithm, the selected voxels were always located in the internal auditory canal. In 35 subjects out of 39, the obtained masks were continuous while in 4 subjects (3 volunteers), no voxel were included in the acoustico-facial bundle cluster at the porus of the canal (ie. at the CSF/temporal bone interface) with the SC-based tractography (figure 2.16).

SC-based tractography versus streamline Tractography in volunteers

The AFD values extracted from the streamline tractography masks range from 0.45 to 1.47 for the right acoustic-facial bundle and from 0.48 to 1.32 for the left acoustic-facial bundle. The mean AFD was estimated as 0.82 (standard deviation (SD) 0.29) on the right side and 0.86 (SD 0.23) on the left side. The AFD values extracted from the SC-based tractography masks range from 0.5 to 1.84 for the right acoustic-facial bundle and from 0.43 to 1.82 for the left acoustic-facial bundle. The mean AFD was estimated as 0.60 (SD 0.09) on the right side and 0.56 (SD 0.09) on the left side.

The figure 2.17 illustrates the differences in FOD distribution along the acoustic-facial bundle between the two algorithms.

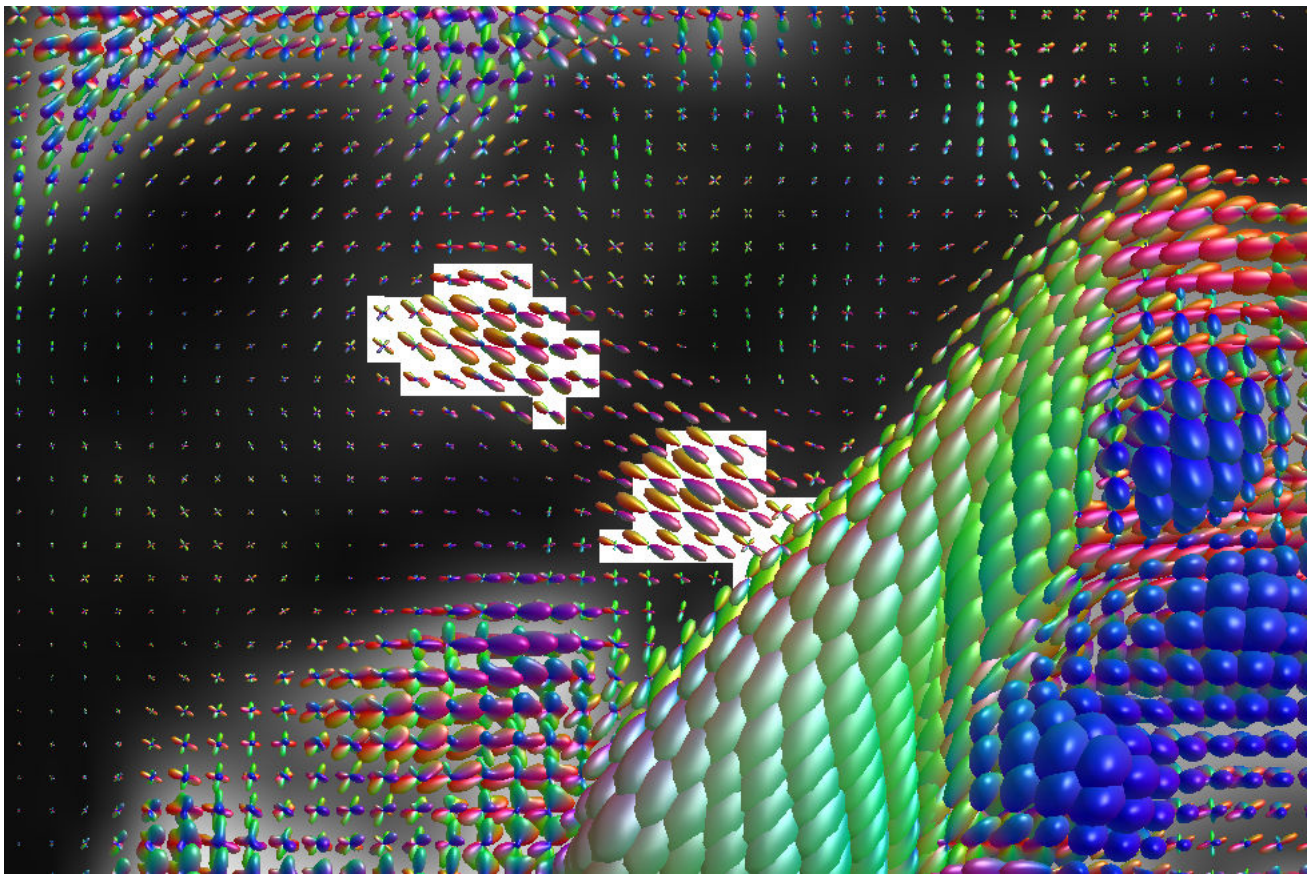

FIGURE 2.16 – **Example of discontinuous spectral cluster in a healthy volunteer.** In this case, the spectral cluster algorithm has failed to reconstruct a continuous cluster including all the FODs along the acoustico-facial bundles. We raise the hypothesize that susceptibility artifacts at the temporal bone interface hinder the FOD estimation quality, owing to low Signal-to-Noise Ratio area

The AFDw values extracted from the streamline tractography masks range from 0.3 to 1.32 for the right acoustic-facial bundle and from 0.21 to 1.14 for the left acoustic-facial bundle. The mean AFDw was estimated as 0.63 (SD 0.25) on the right side and 0.61 (SD 0.21) on the left side. The AFDw values extracted from the SC-based tractography masks range from 0.27 to 0.84 for the right acoustic-facial bundle and from 0.20 to 0.82 for the left acoustic-facial bundle. The mean AFD was estimated as 0.58 (SD 0.11) on the right side and 0.56 (SD 0.12) on the left side (Figure 2.18).

SC-based tractography versus streamline tractography in patients

The AFD values extracted from the streamline tractography masks range from 0.56 to 1.35 for the right acoustic-facial bundle and from 0.46 to 1.17 for the left acoustic-facial bundle. The mean AFD was estimated as 0.84 (SD 0.25) on the right side and 0.91 (SD 0.21) on the left side.

The AFD values extracted from the SC-based tractography masks range from 0.5 to 0.79 for

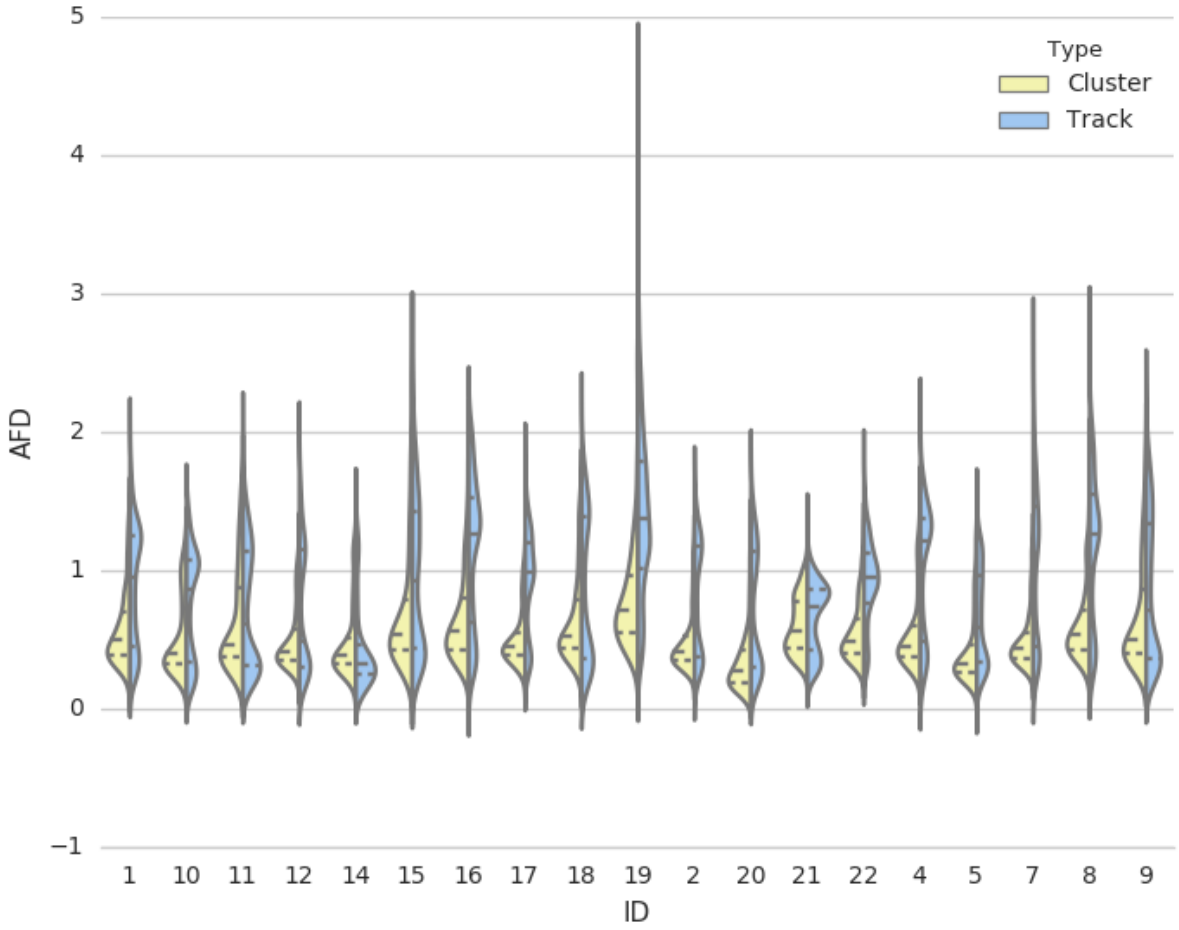

FIGURE 2.17 – **AFD distribution comparing the two method of tractography in volunteers.** The distribution of AFD values is distributed around 0.6 with the SC method and 0.8 with the streamline tractography method, implying larger selection of voxels with high AFD values using the latter process. In addition, we can see a second cluster of AFD values with the streamline tractography algorithm, which is presumed to represent the background.

the right acoustic-facial bundle and from 0.48 to 0.73 for the left acoustic-facial bundle. The mean AFD was estimated as 0.64 (SD 0.08) for the right side and 0.63 (SD 0.08) on the left side.

The AFDw values extracted from the streamline tractography masks range from 0.39 to 1.17 for the right acoustic-facial bundle and from 0.39 to 1.02 for the left acoustic-facial bundle. The mean AFD was estimated as 0.62 (SD 0.23) on the right side and 0.62 (SD 0.18) on the left side.

The AFDw values extracted from the SC-based tractography masks range from 0.3 to 0.79 for the right acoustic-facial bundle and from 0.27 to 0.73 for the left acoustic-facial bundle. The mean AFD was estimated as 0.62 (SD 0.11) on the right side and 0.61 (SD 0.11) on the left side.

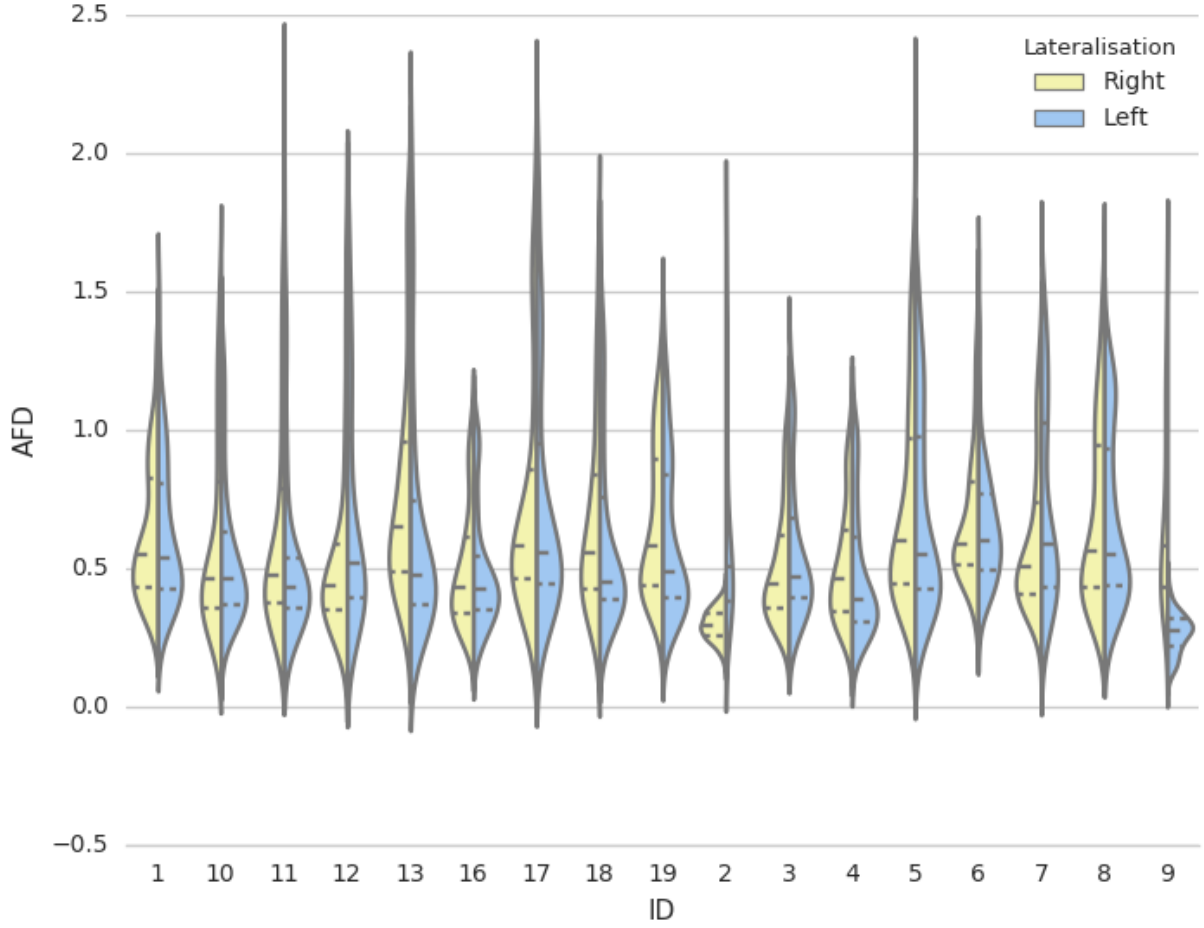

FIGURE 2.18 – **AFD distribution comparing left and right-sided clusters with SC-based Tractography.** The distribution of AFD values is globally symmetrical with the SC method between left and right-sided acoustic-facial bundles.

Using AFD values extracted from SC-based tractography, we found a significant difference (p=0.007) between the acoustic-facial bundles of patients with Meniere's disease and those of healthy volunteers. We have also found a correlation between the age of patients and AFD values extracted from SC-based Tractography, only in the symptomatic sides (Figure 2.19, Pearson Correlation, p=0.005).

The nerves of patients had a higher AFD value than those of healthy volunteers. The streamline tractography method did not show significant differences (p=0.55) between diseased and healthy acoustico-facial bundles.

Using AFDw values, no tractography method showed significant differences between patients

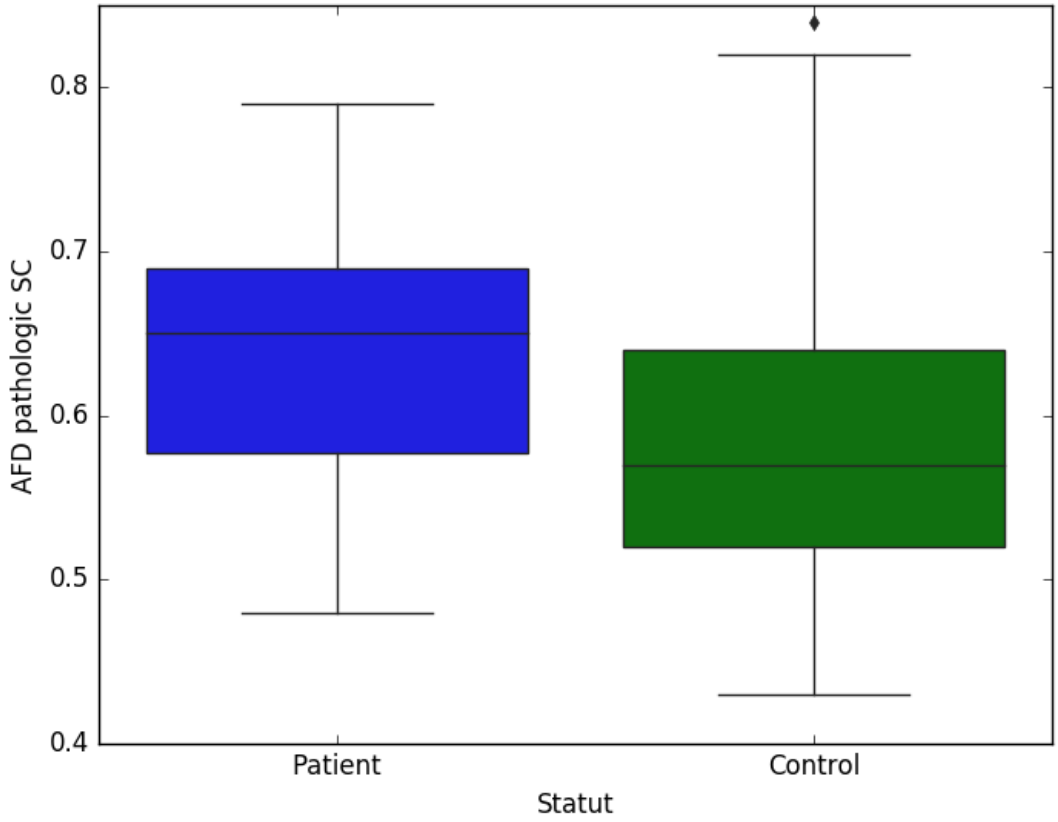

FIGURE 2.19 – **Mean AFD values extracted from SC-based Tractography acoustico-facial bundles in patients and volunteers.**

and controls (p=0.09 with the SC-based tractography, p=0.93 with the streamline tractography). In patients, we did not find a significant difference between the symptomatic and asymptomatic side using different quantitative analyses.

Discussion

Streamline tractography : a state of the art method for cranial nerves exploration ?

Although Diffusion Tensor Imaging-based tractography remains the most widely used tractography method for mapping cranial nerves, CSD-based tractography has started to draw attention in the field of clinical investigation to address the problems that affect the tensor model in estimating the FOD [70, 102, 109, 110]. In contrast to the brain for which the vast majority of voxels contains several fiber populations, the cranial nerves are thought to include mainly single-fiber voxels, particularly in their intracranial segment. Despite this apparent simplicity in modeling the diffusion signal, a recent study has shown that using CSD can improve the

reliability and feasibility of cranial nerve tractography [70]. We can propose the hypothesis that in pathological condition, such as tumor compression with axonal loss or edematous tissues surrounding the nerves ; the precision of the FOD reconstruction with spherical harmonics tend to provide more accurate fiber reconstructions than the classic tensor model [83, 84].

Tractography post-processing classically involve three steps : the correct estimation of fiber orientations ; the application of an appropriate tracking algorithm and the extraction of quantitative information. The reliability of tractography results is dependent on all 3 steps. Two postprocessing approaches currently make reference for extraction of quantitative information from anatomical regions using DWI : Voxel-based analysis (VBA) and streamline tractography. Voxel-based analysis (VBA) is an image analysis technique for performing statistical tests across and within groups of subjects, with the ability to localize group differences or correlations without any prior spatial hypothesis. Prior to smoothing images to boost the SNR, VBA usually starts by transforming all subject images to a common template using an image registration algorithm. The subsequent step is to perform statistical analysis at each voxel, depending on the disease model. If we raise the hypothesize that cranial nerves are likely to be affected by fiber density variation along their entire length, which has been demonstrated in head and neck cancers, for example [102], the use of the classic VBA approach appears problematic. Indeed, VBA with classic method of clustering could potentially merge voxels with osseous tissue or meningeal spaces adjacent to acoustic-facial bundle, rendering difficult further statistical tests. In addition ,the smoothing process can potentially hinder the visualization of cranial nerves with small FOD amplitudes.

On the other hand, the result of streamline tracking strongly depends on the anatomy of the cranial nerve tracked, its environment, and the post-processing steps [70]. Each cranial nerve has anatomical specificities to be taken into account before setting parameters for tracking the nerve, such as initiation and termination condition, curvature angle or number of fibers. In addition, small fibers of cranial nerves arising from the pons cross tangentially large brainstem tracts and the tractography can provide spurious fibers if these brainstem tracts are recruited, as illustrated below (figure 2.20).

Diffusion imaging is associated with geometric distortions either caused by the magnetic susceptibility distribution of the subjects' head, Eddy currents from the rapid switching of the diffusion weighting gradients, or the slight movements of the subject's head during the long MRI acquisition protocol. Furthermore, these distortions are frequent at the skull base because of the close interface of air, bone, and soft tissues. Here, we have used the optimal process to correct for artifacts, yet local areas of SNR loss can potentially occur with modification of the FOD. The use of probabilistic algorithms for streamline algorithms, even with filtering of tractograms, results in a tendency to overestimate the nerves' diameters, thus leading to incorrect quantitative extraction of the AFD values along the nerves. This is illustrated by the high variability of the

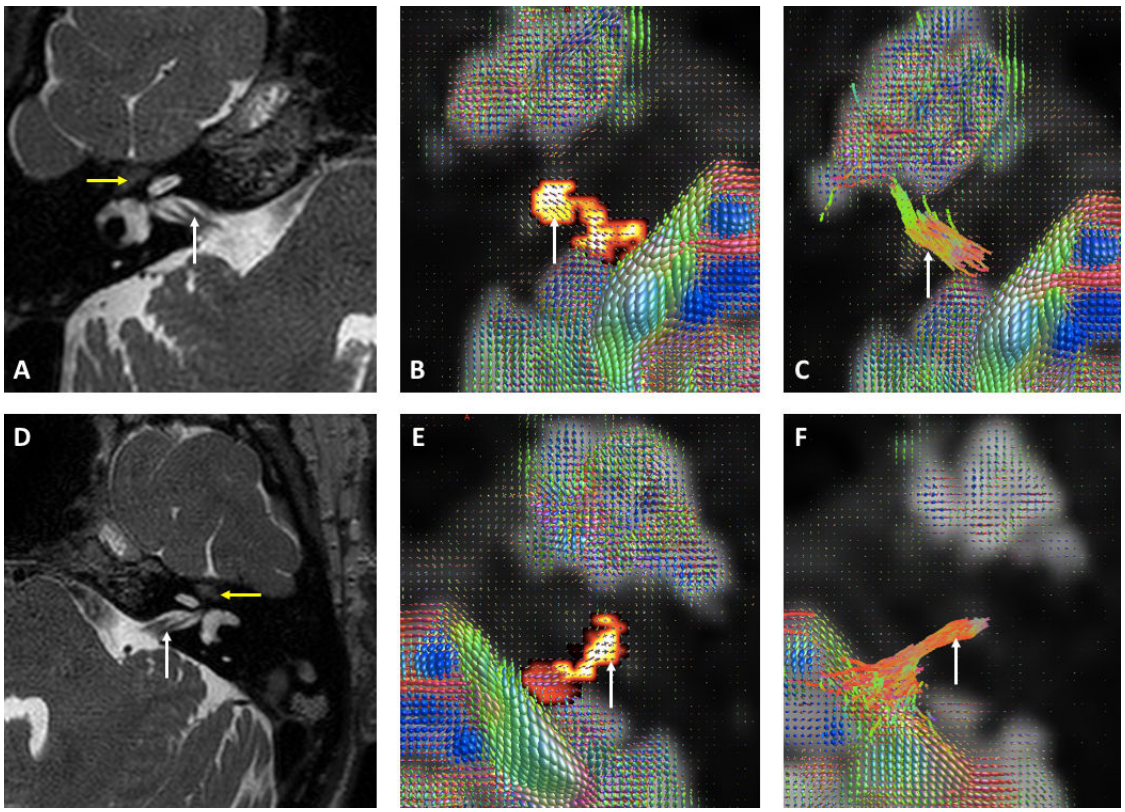

FIGURE 2.20 – Comparison between T2-Weighted Sequences (A and D), SC-based Tractography (B and E) and streamline tractography (C and F) in volunteers. A and D : The cochleovestibular nerve (white arrows) is located at the posterior and inferior part of the acoustico-facial bundle. The facial nerve runs through the superior and anterior part of the canal before curvature of 90° in the tympanic segment (yellow arrow). B and E : SC-based Tractography reveals irregular cluster shape, depending on the FOD amplitudes and stopping at the fundus of the canal in all cases (white arrows). C and E : two example of typical streamline tractography (white arrows). In image C, the bundle runs to the brain temporal lobe, whereas in image F, the bundle starts with dispersion of tracks at the brainstem. Streamline tractography was performed with the same parameters in each individual after spatial registration of the images to define the same spatial coordinates.

AFD along the acoustic-facial bundles of healthy individuals, added to difficulties in streamlines initiation or termination, in comparison with anatomical landmarks. To note, we weighted the AFD values by the number of tracks to limit the weight of voxels with low number of spurious tracks, but we did not find that this coefficient added value. By contrast, SC-based Tractography provides low variability of AFD values extracted from acoustico-facial bundle masks in controls, allowing to confirm the AFD modification in the MD model. As we have previously demonstrated the reliability of this method to study the corpus callosum, we are confident in the added value of spectral clustering to assess cranial nerve modification in other disease models or other cranial nerves' disorders.

Clinical Impact

Meniere's disease that results in severe to profound bilateral hearing loss is now an indication for cochlear implantation. It is controversial whether the patients benefit from cochlear implantation that is similar to that for other deafness etiologies [111, 112] or for hearing outcomes worse than for the general population [113]. With respects to the acoustico-facial bundle density augmentation that we have demonstrated with the SC-based tractography, our work supports the theoretical efficiency of such procedure. Previous cranial nerve study with morphological MRI sequences support our findings, showing a swelling of cranial nerves VII and VIII within patients compared to a control group with normal hearing. The similar reaction of the facial nerve supports 'mediator'-based theories of MD pathophysiology [68], in contrast to pathological studies, which have described loss of neural structures in MD [65] after the death of patients. The absence of correlation between the hearing loss level and the AFD values potentially exclude neural plasticity phenomenon, ie. increase fiber density of the acoustico-facial bundle to compensate the cochlear injury. Interestingly, the presence of a significant correlation between the age of patients and AFD values of the bundle on the symptomatic sides appears coherent with the progressive evolution of this disease over time in adults. The absence of correlation between AFD increase and the presence of endolymphatic hydrops support the multi-causal dimension of the disease.

Limitations

SC-based tractography has shown difficulties to be applied in areas with low SNR/ Susceptibility artifacts such as the porus of the internal auditory canal. In our study, we were unable to reconstruct a continuous cluster of the acoustico-facial bundle in 5 subjects, owing to FOD with different amplitudes on the nerve course. Our use of the term spectral clustering-based tractography is also not without limitations. SC-based tractography may be misinterpreted as being an anatomical structure directly reflected by the cluster, whereas it estimates and merges the voxels with similar FOD amplitudes in a local region previously defined. We can hypothesize in pathological acute modification of the FOD (eg. owing to ischemia or demyelinating disorders), the clustering method would exclude voxels that actually contain diseased cranial nerves. Here, using two clusters to distinguish the nerve from the background was efficient because the temporal bone contains voxels with poor diffusivity properties. We believe that SC-based tractography is appropriate because it is at least related to the amplitude of the FOD to select voxels with close inherent structure, which can be globally preserved in cases with axonal loss or tumor infiltration [102] along a specific nerve. Further study is warranted to validate the cluster projection by linking each cluster to histologically studied nerves.

Importantly, streamline tractography is also known to be sensitive to various artifacts for white matter bundle reconstruction. In pathological condition, acute disorders such as ischemic optic neuropathy is also related to optic nerve fascicle interruption [109]. Another on-going problem of streamline tractography relies on difficulties to terminate the tracks in tumor condition

or in non-nervous tissues [70]. The overestimation of the track size with probabilistic algorithms may partially explain in our study the variability of the quantitative values extracted from this process.

Spectral-Clustering based tractography is easily interpretable by clinical audiences with anatomical knowledge because, in contrast to white matter fascicles, the cranial nerves courses can be displayed by morphological MRI sequences. Another limitation is the the rotational sensitivity of the amplitude metric. For example, the facial nerve was not displayed after the canalar segment. We can mention that streamline tractography has also demonstrated such issue, both in the literature and in our study. We have performed streamline tractography without using exclusion ROIs, that is time-consuming in clinical practice. It cannot be set at the template level owing to the anatomical variability between patients and registration potential problem. Termination points such as those proposed by the anatomically-constrained tractography framework [114] would be useful for cranial nerve exploration.

Recently-developed technique of fiber tract-specific statistical analysis [86] also hold promise for brain white matter fascicles quantitative analysis, relying on the combination of local quantitative biomarkers and anatomical connectivity information for selection of voxels of interest. Here, we have used the total AFD value (ie. the sum of the AFD for all fiber populations). It is less informative than the AFD per fiber population, based on the fiber tract-specific statistical analysis (referred as "fixel AFD or FD in the literature). Yet, we have proposed an anatomical clustering method without the need to perform streamlines tractography, to improve reproducibility and inter-reader robustness of quantitative analysis owing to the absence of usual tracking parameters setting.

Finally, the SC algorithm is highly efficient in terms of computer requirements. The spectral clustering algorithm can be achieved in a selected anatomical area in the order of seconds/minutes with usual local computer. This can be important for future expansion in the clinical setting. Such techniques have never been applied for cranial nerve exploration and larger group studies with a more important number of patients are needed to compare different approaches.

2.3 Manifold Learning

2.3.1 Manifold Learning : General Introduction

Manifold learning is a class of machine learning methods that are gaining success and attracting interest, allowing reconstruction of a manifold subspace to represent, understand and visualize degrees of freedom of complex data. The idea behind is that the number of observations/data/samples is generally too low for describing the complexity of the data. In other words, the data can generally be described by a small number of latent variables, equivalent to degrees of freedom. The reader can refer to the **Statistical Learning comprehensive book** . A good example in the daily life is visage recognition algorithms, which use a manifold subspace to identify faces regardless of the brightness or orientation of each individual. In Medicine, Manifold Learning algorithms have recently proved to dramatically improved image reconstruction (CT, MRI, Pet) for different applications [115].

Manifold learning has also been used for various problems of medical imaging like registration, segmentation, and classification. For example, Gerber et al. [116] use manifold learning to perform a population analysis of brain images (figure 2.8).

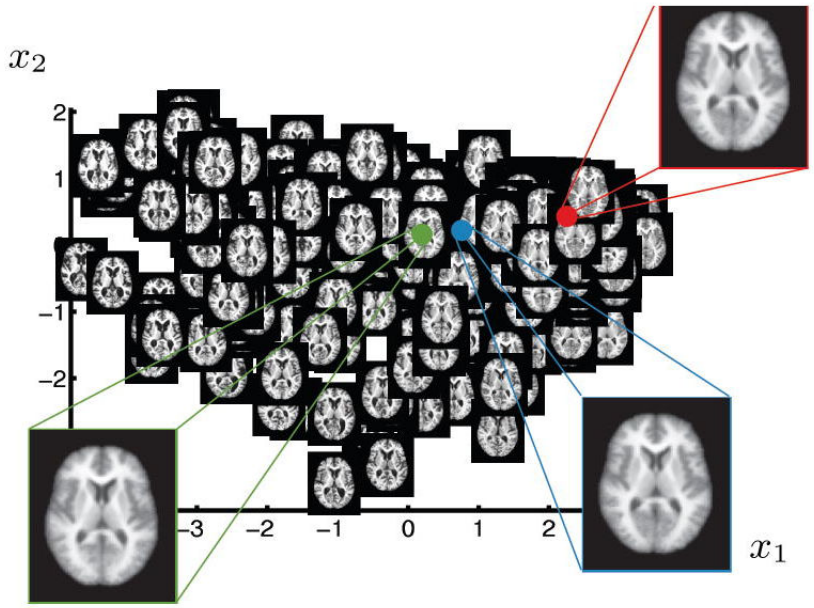

FIGURE 2.21 – 2D parametrization of OASIS brain MRI database obtained by a manifold subspace. This work raise the hypothesis that a low-dimensional, nonlinear model can effectively represent variability in brain anatomy such as ventricles size. For each brain image axial slice number 80 is visualized at the corresponding location on the 2D manifold. The insets show the mean (green), median (blue) and mode (red) of the learned manifold and the corresponding reconstructed images

A key factor in such methods is image representation. The manifold could be approximated using the Euclidean distance between image pairs, however this would not be robust to translation or scaling [117]. The Isomap (Isometric Feature Mapping) algorithm has been designed to overcome this limitation. Unlike Principle Component Analysis, Isomap is a non-linear feature reduction method illustrated in Figure 2.22. The Isomap application can be divided in three steps :

— The estimation of the distances of local neighbors of each observation
— The creation of a graph based on these distances and the calculation of the new geodesic distances between each pair of observations based on the Dijkstra's algorithm. This algorithm find the shortest paths between nodes in a graph [117]
— The multidimensional scaling (MDS) algorithm then obtains the reduced space. The MDS algorithm tries to set each object such that the geodesic between-object distances estimated in the second step are preserved as well as possible.

Thus, the high dimensional space is projected on a reduced space with the respect of its internal structure.

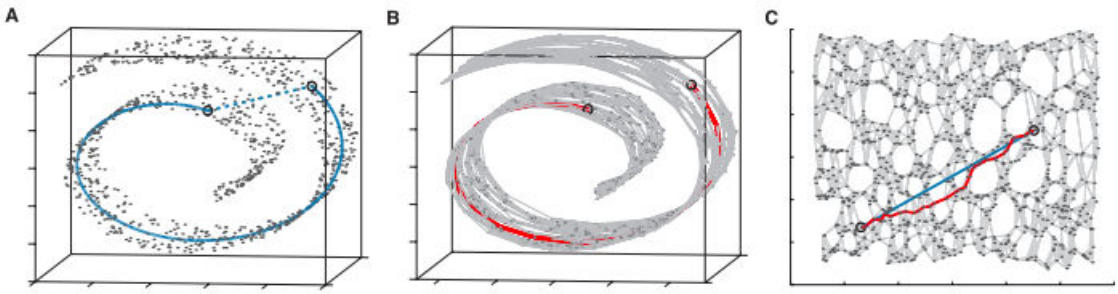

FIGURE 2.22 – Extracted from [117] A/Two points close together in Euclidean Space in this "Swiss roll" dataset may not reflect the intrinsic similarity between these two points.B/A graph is constructed with each point as n nearest neighbours (K=7 here). The shortest geodesic distance is then calculated by a path finding algorithm. C/The 2D graph is recovered from applying Multidimensional scaling to the matrix of graph distances. A straight line has been applied to represent a simpler and cleaner approximation to the true geodesic path shown in A.

2.3.2 Manifold Learning : Application to DWI

The FOD intrinsically contains the anatomical information of the fiber architecture, which disappears when extracting a understandable scalar parameter such as the AFD coefficient. Direct analysis of the FOD as a mathematical object requires advanced tools with the ability to manage high-dimensional vector space. Since typical clinical studies often include a limited number of patients, the natural mathematical space of the FOD at the group level need to be

constrained. This problem is known as the Curse of Dimensionality and explain why we need to reduce the space to apply classification and/or clustering algorithms on FOD analysis.

The estimation of the embedding reduced space for DTI-based tensors have been previously described [118] using Manifold Learning. Mathematically, it has been showed that no Diffusion modelling method (including DTI and high-orders models) [97, 119] can't be properly analyzed in a linear Euclidean space. Defining a metric between FOD is a key step to assessing similarity, estimating distributions and testing hypotheses. In practice, the DWI signal cannot be represented in a manifold linear subspace such as that proposed by principal component analysis (PCA), which is already used in the field of DWI for denoising process for example [120]. Segmentation of FOD data is a challenging problem because it is necessary to develop algorithms that can correctly handle the non-Euclidian mathematical structure of the diffusion function [97, 119]. Recent methodological developments follow the principle of clustering regions that we have described previously for quantitative data extraction from FOD amplitudes. We can divided methods for FOD segmentation into two categories : those with mathematical *a priori* based on Riemannian spaces estimation [97] and methods based on data which mimic the underlying structure without any *a priori* [117, 118]. Methods based upon Riemannian spaces require the definition of a complex distance, which limits possibilities to perform basic mathematical operations [97] for clinical research application.

More recently, manifold learning has been used on DWI to map the white matter fiber in a controlled subspace with an adapted model of fingerprint called "fiberprint" [87] and on multimodal MRI acquisition including DWI data [121]. These previous studies have shown interesting relationship between compact fingerprint and genetic biomarkers on large population.

Here we propose to use a manifold learning representation of the diffusion data through constrained spherical deconvolution estimation, in order to analyze anatomically relevant brain or cranial nerve structure. We have firstly tested our algorithm on synthetic data, by generating five different patterns of single and crossing fibers using DIPY (http ://nipy.org/dipy/index.html), a free and open source software project for computational neuroanatomy, focusing mainly on diffusion magnetic resonance imaging (dMRI) analysis (Figure 2.23).

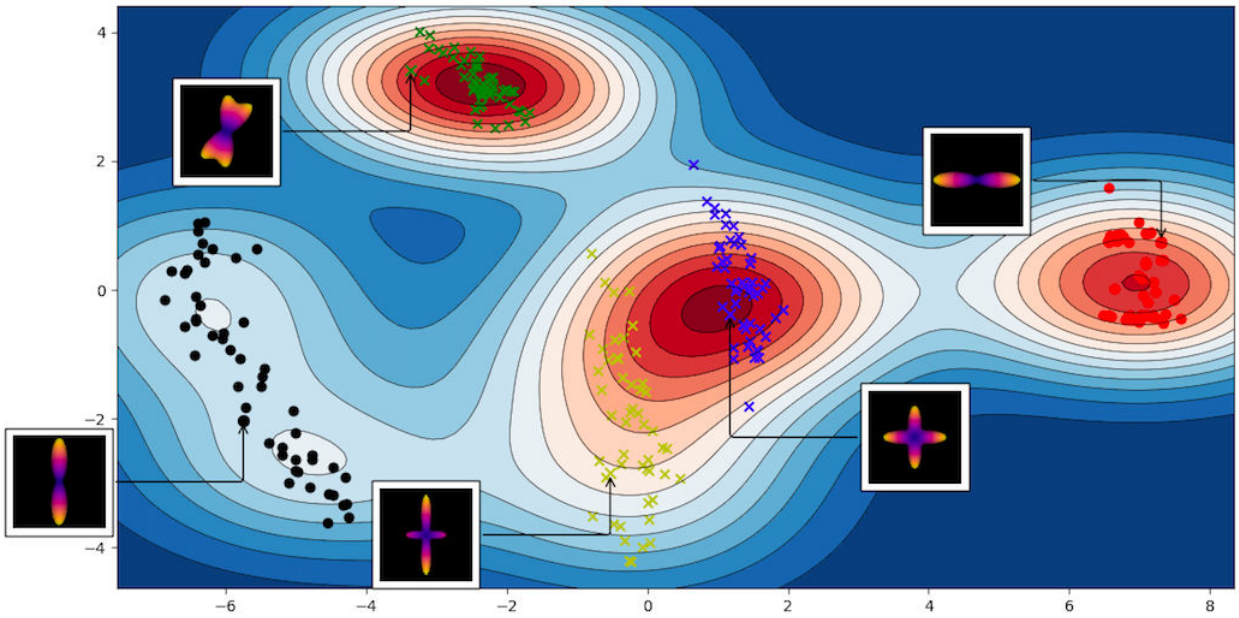

FIGURE 2.23 – Example of Manifold learning representation of FOD data with synthetic modification of number of fibers per voxel and of degrees of freedom between fibers. We have firstly generated five FOD patterns as follow : three populations of crossing fibers with various degree of rotation and two populations of single fibers with rotation variation. We have then added some noise on amplitude degree or direction in order to obtain 50 FOD population per pattern (total of 250 FOD population). The Manifold subspace represents the different clusters of FODs : the green, yellow and blue crosses encompass crossing fibers population. The red and black points represents single fibers' population. The different patters are well distinguished allowing to compute Gaussian distributions in the subspace.

2.3.3 Manifold Learning analysis of the corpus callosum : test-retest procedure

Using the same Diffusion-weighted dataset previously described, we have intended to evaluate the robustness of CC manifold dimension reduction reproducibility. The objective was firstly to extract the background from the CC structure in the manifold subspace, then to segment the CC main cluster with reference to post-mortem anatomy.

The manifold learning is not a clustering method as itself. We have therefore used a mean shift semi-supervised kernel clustering method in the manifold subspace. Mean shift clustering is a powerful nonparametric technique that does not require prior knowledge of the number of clusters and does not constrain the shape of the clusters [122]. The mean shift algorithm cannot be used directly in the natural FOD space since the number of observations is too sparse. Here the constraints are imposed by a non linear transformation of the mapped points in the manifold subspace, which allows to accurately estimate the underlying distribution of the obtained data.

The corpus callosum (CC) has been studied and segmented in the human brain in order to better understand its function in various MR imaging studies. It has been divided in various ways, including division based upon gross morphologic components (eg. the genu and splenium), and functional partitioning based upon tractography designed using target regions in the cerebral cortex [108]. Functional partitioning usually implies to perform tractography to cluster the CC structure into meaningful parcels.

Post-mortem anatomy taught us that the CC can be divided in five functional parts [123, 124]. The CC1 part comprises the genu and rostrum while most of the prefrontal fibers course through this sector. CC2 is presumed to be related to the fibers that arise from the dorsal premotor area. It is situated between the caudal portion of the genu and the rostral limits of CC3. CC3 lies above the fornix in the midportion of the CC and contains interhemispheric fibers from the motor cortex. CC4 conveys fibers that originate mostly in the parietal lobe. Finally, CC5 includes the splenium and conveys fibers from the temporal and occipital lobes.

Here we want to illustrate the potential of FOD dimensionality reduction on CC segmentation with comparison to knowledge coming from Rhesus monkey dissection.

METHODS

Firstly we have extracted the amplitude of spherical harmonic images along 100 specified directions. We have then used the Isomap (Isometric Feature Mapping) algorithm of Python SciKit-Learn ToolBox. The main idea of the Isomap algorithm is to estimate an embedding reduced space that preserves the distance between the pairwise geodesic distances between samples in the natural space. The algorithm firstly calculates the distance of a sample for its k nearest neighbors and constructs a graph between these distance from this local neighborhood.

It allows to estimate the intrinsic geometry of the data manifold based on a rough estimate of each data point's neighbors on the manifold. Thus the high dimensional space is projected on a reduced space with the respect of its internal structure.

We have then used an integrated kernel-based approach to voxel-based analysis that accurately estimates the underlying distribution of the obtained data. We have firstly computed an atlas of the probabilities densities of the CC FODs in each voxel. In other words, FODs morphology (ie. single fiber or crossing fibers with a given degree of rotation between fibers) in our population were merged by clusters with regards to close FOD's amplitude (Comparison of n=100 dimensions vectors). the Gaussian kernel density estimation allows to have a representation of the typical manifold subspace of volunteers corpus callosum structure. We consider points outside the lines as potential outliers like voxels in background or artifacts.

Informative explanation for the estimation of the distribution based on kernel density can be found in D.W. Scott's book, "Multivariate Density Estimation : Theory, Practice, and Visualization", John Wiley Sons, New York, Chicester, 1992.

To test the efficiency of the clustering method, we have evaluated the reproducibility of the clusters in terms of shape and homogeneity. For the shape comparison, we use the classic Dice metric for the patient j defined as $Dice(j) = \frac{2|ROI_1^j \cap ROI_2^j|}{|ROI_1^j| + |ROI_2^j|}$ where $||$ represent the cardinal of the set of voxels, and ROI_i^j represent the obtained clusters for the acquisition i and the patient j. We further consider the CC cluster for the homogeneity evaluation, and evaluate the mean of the AFD over the ROI. The considered metrics are the Intra Class Correlation (ICC) coefficient and the Bland-Altman plot. The ICC measure corresponds to the ICC(3,1), as extracted from the reference article [95].

Finally, we have studied the visual representation of the CC cluster in comparison with post-mortem anatomical atlas.

RESULTS

We have firstly obtain a clear representation of the background in the manifold subspace, as illustrated on the Figure 2.24. In order to compare with the SC-based tractography, we kept two ROIs : the first one with the higher AFD value is presumed to represent the CC while the other clusters were merged to represent the background.

The Figure 2.25 displays an example of the reproducibility of the CC main cluster extraction in two different sessions.

Space reproducibility for sessions 1 and 2 (intrasession) : the mean of the $Dice(j)$ over the control group is $0.91 +/- 0.11$. This score displays a very good reproducibility in term of shape. Only one patient has two clusterings slightly different. Homogeneity reproducibility for sessions 1 and 2 : The ICC of the AFD mean values over the CC ROI is 0.92 which corresponds to a very

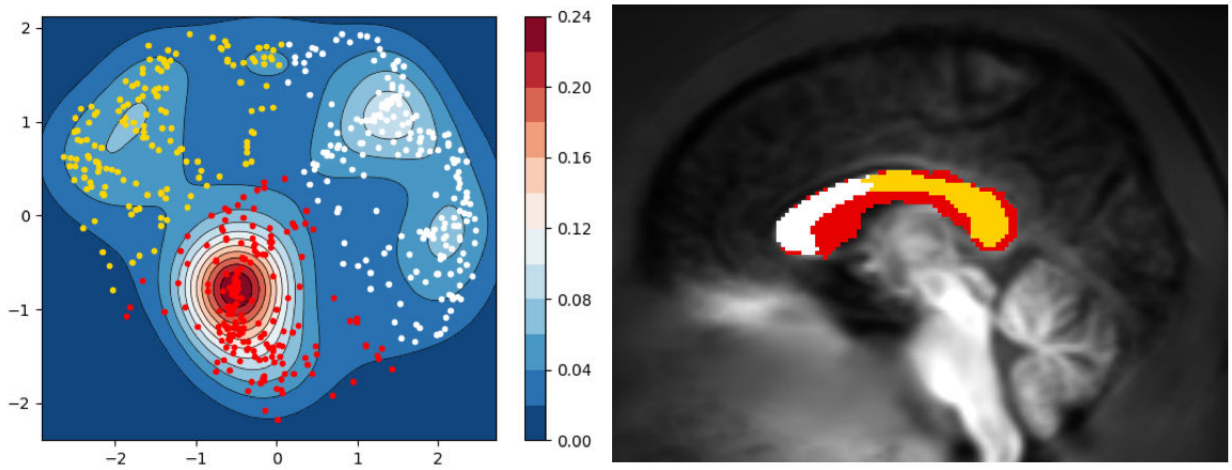

FIGURE 2.24 – Relationship between manifold clusters and anatomical subpart of the CC. The red points corresponds to the higher density in the manifold, and can be identified as the background on the template image. Interestingly, the manifold split the corpus callosum into the genu and the anterior part of the body with white points ; and the posterior part of the body added to the isthmus and the splenium with the yellow points.

		S1-S2	S1-S3
Spectral clustering			
	Dice	0.95 +- 0.04	0.88 +- 0.07
	ICC	0.98	0.84
Manifold learning analysis			
	Dice	0.91+- 0.11	0.89 +- 0.13
	ICC	0.92	0.73

TABLE 2.2 – Results for the Dice metric and the ICC for SC and manifold learning analysis between sessions 1 and 2, and between sessions 1 and 3.

high reproducibility .

Space reproducibility for sessions 1 and 3 (intersession) : the mean of the $Dice(j)$ over the control group is $0.89 +/- 0.13$. This score displays a very good reproducibility in term of shape. Only one patient has two clusterings slightly different. Homogeneity reproducibility for sessions 1 and 3 : The ICC of the AFD mean values over the CC ROI is 0.73, which corresponds to a high reproducibility.

We have summarized intra and intersession reproducibility of CC analysis for each method of Machine Learning in the following table 2.2.

After testing the reproducibility, we have extracted the main cluster of the CC for a new representation in the manifold. The objective was to compare anatomical known functional CC subpart with manifold representation. In 10 out of 15 patients, we have extracted 5 clusters coherent with the anatomical atlas, with a vertical separation between cluster. In 4 out of 15

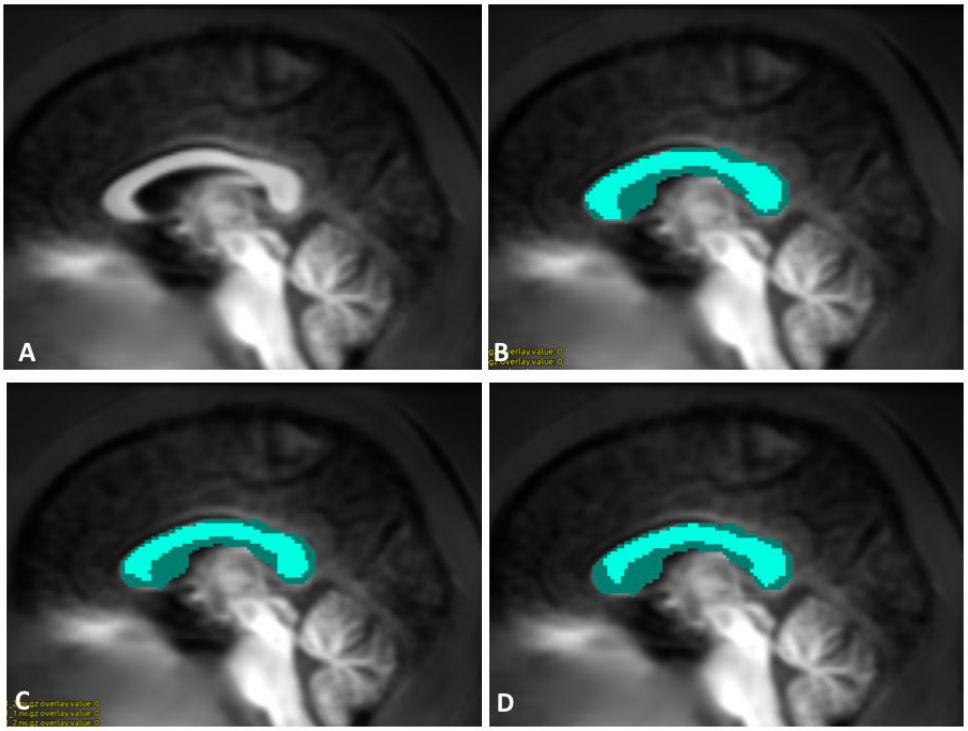

FIGURE 2.25 – Illustration of Corpus Callosum Manifold Clustering at each session (A : Template image, B : First Session, C : Second Session, D : Third session). The light blue area corresponds to the mask, as drawn in the template space. The dark blue area corresponds to the cluster of the CC, selected on the AFD mean value.

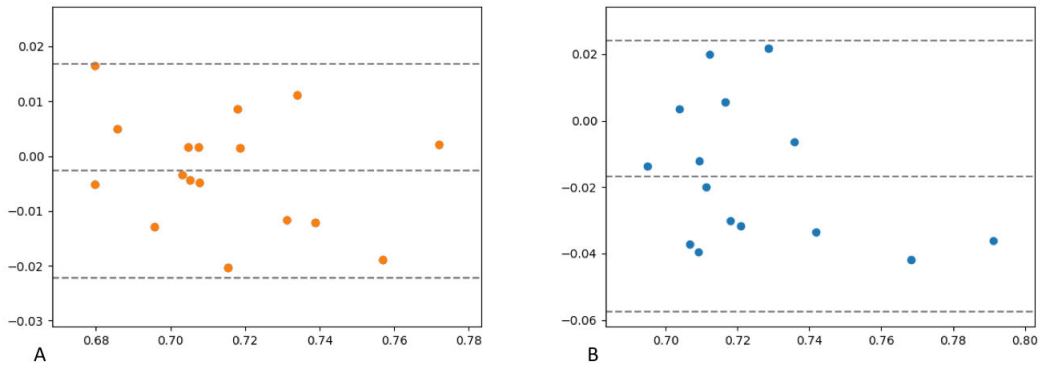

FIGURE 2.26 – Bland Altman diagram showing high reproducibility between AFD values extracted from Manifold Learning analysis of the Corpus Callosum for the intrasession test retest and lower reproducibility for the intersession test-retest. The abscissa (x-axis) value and the ordinate (y-axis) value respectively correspond to the mean of the two measurements and the difference between the two values.

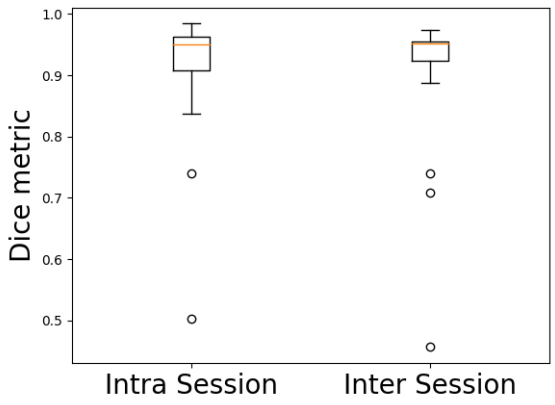

FIGURE 2.27 – Intrasession and Intersession DICE metrics for Manifold Learning analysis of the corpus callosum

patients, only 4 clusters were extracted while in one patient the clusters were not anatomically coherent.

DISCUSSION

Comparison of spectral clustering and manifold learning for clustering purpose

The SC and the manifold learning algorithms try to capture the intrinsic structure of the data by focusing on the local neighboring to estimate new geodesic distances between observations. In mathematics, this is a rough approximation of the Riemannian space of FODs in a large white matter fascicle. However, the true estimation of Riemannian space is complex and need to design specific metric [97], not adapted for further application in clinical studies. A major strength of the presented algorithms is the ability to deal with all the metrics include in the spherical harmonics representation of the diffusion signal, and theoretically coming from other high-order diffusion models.

The main difference between the SC and the manifold learning method is that the former is dedicated for the clustering while manifold learning also permits to capture the embedding space and to visualize it. In addition, the use of manifold learning allows a better understanding of the data structure and avoids the 'black box' aspect of deep learning algorithms.

Since statistical analysis on DTI data was complicated by the 3×3 positive-definite symmetric matrix at each voxel (instead of a single value as in the case of scalar image), Khurd et al. have proven the feasibility on Manifold Learning application including in clinical study [125]. Using both simulated and real data, they have shown that kernel principal component analysis can effectively learn the probability density of the tensors under consideration and that kernel Fisher

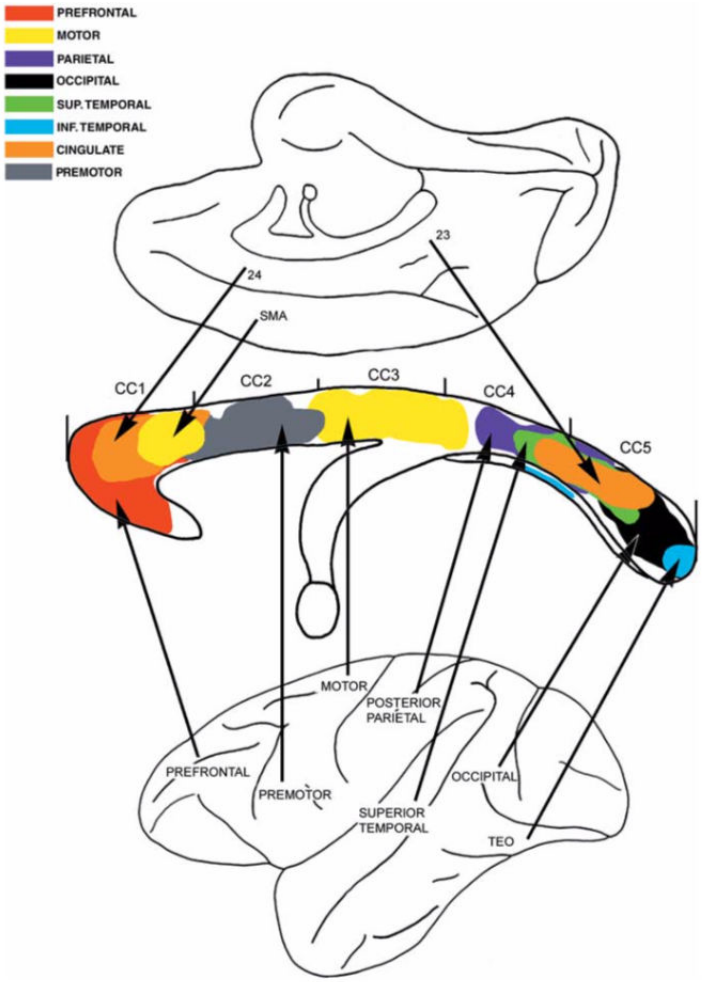

FIGURE 2.28 – Figure extracted from the "Fiber pathways of the brain" notebook, written in 2009 by Schmahmann and Pandya. Composite summary diagram of the topography in the midsagittal plane of the corpus callosum of axons derived from the major lobar regions of the cerebral hemisphere of the rhesus monkey. The lateral view of the cerebral hemisphere (below) and the medial view (above) depict the region of origin of the fibers traversing the corpus callosum, color-coded according to the legend at top left. The designations CC1 through CC5 refer to the five rostral to caudal sectors of the corpus callosum described in this atlas.

discriminant analysis can find good features that can optimally discriminate between groups.

Here, the reproducibility of clustering method in the Manifold subspace appeared lower that those of SC, yet still high with a dice metric of 0.89 and with an ICC measure greater than 0.7 for inter session analysis. As previously mentioned, the manifold learning permits to visualize the embedding space. Building clusters in a manifold subspace is a relevant next possibility in the context of anatomical structure extraction. Since the CC both include single fiber and crossing fiber populations, the results of manifold analysis that constantly displayed several clusters over

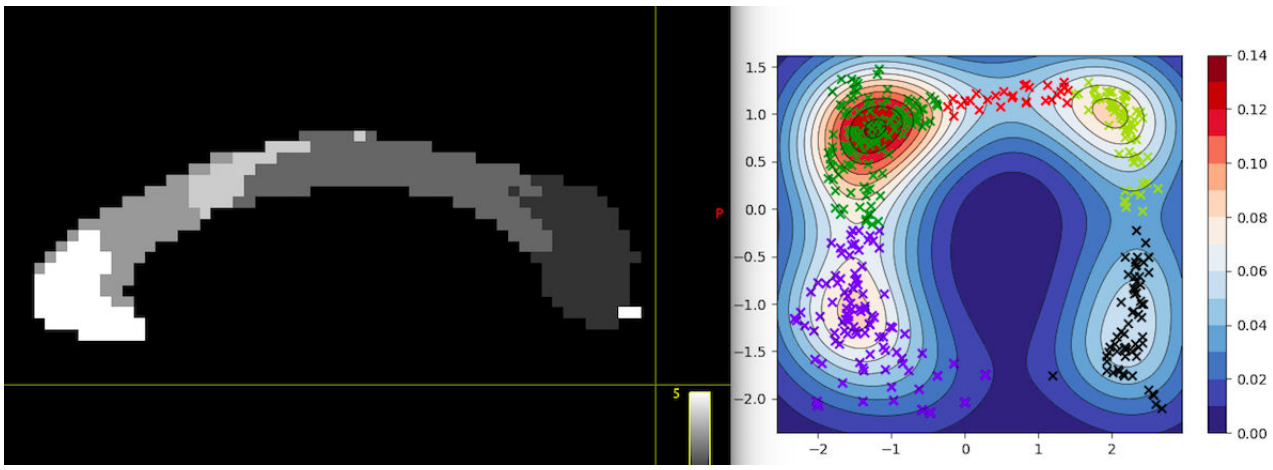

FIGURE 2.29 – CC "functional" clustering using manifold learning : 5 different clusters were individualized on the CC midplan while 4 Gaussian distribution were identified in the manifold subspace. The fifth cluster corresponds to red crosses, which are not sufficiently spatially close to be isolated with a high density, yet allowing to anatomically locate this cluster.

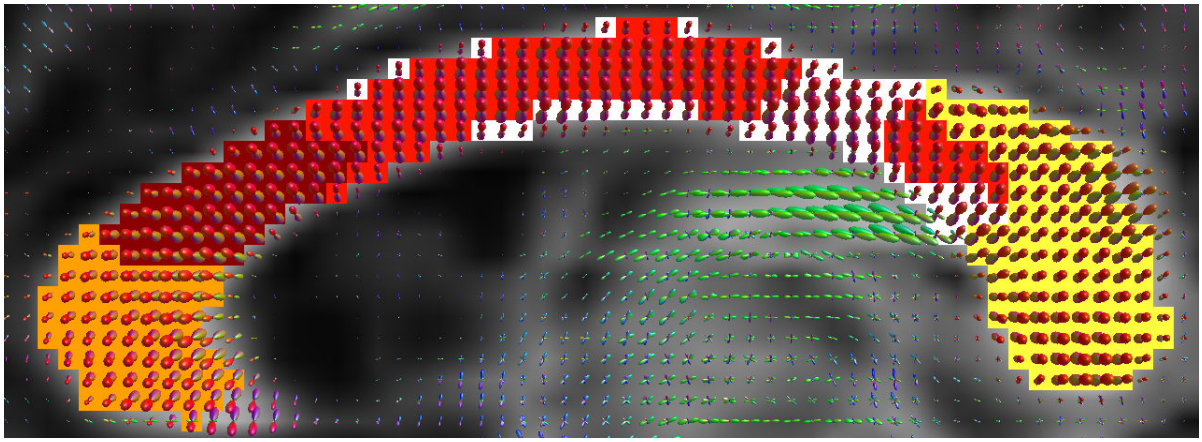

FIGURE 2.30 – Example of the subject 4 clusters, as obtained from the manifold subspace. The red cluster 3 is presumed to represent CC3, though not continuous.

MRI sessions can be explained by variation of spherical harmonics amplitude in this structure.

While SC-based tractography can be characterized by the higher intra and intersession reliability, the potential added value of manifold learning to study FOD variability can be summarized as follow :

1/ The ability to take into account complex variation of the Diffusion-Weighted Signal, either in multiple fiber population voxels of controls or in voxels with pathological modification of the intra or extra-axonal compartment. The manifold representation allows to display complex cluster structure while the SC algorithm imposes to previously set the number of required cluster.

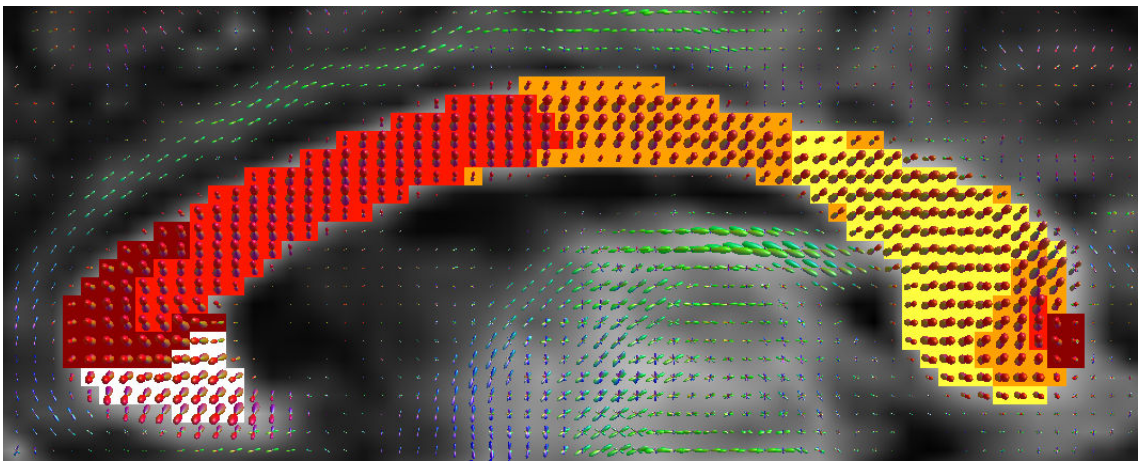

FIGURE 2.31 – Example of the subject 7 clusters, as obtained from the manifold subspace. The five CC functional part are well distributed, except in the CC splenium.

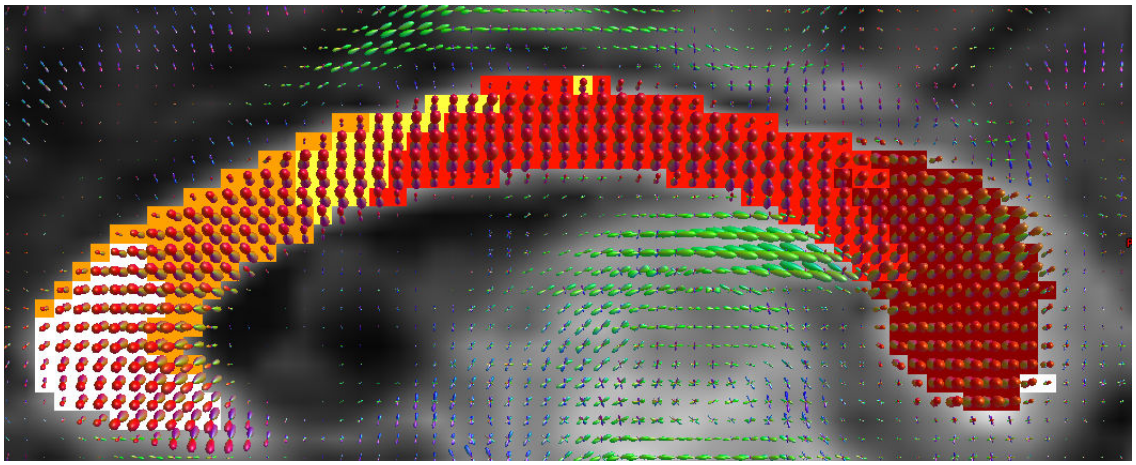

FIGURE 2.32 – Example of the subject 9 clusters, as obtained from the manifold subspace. The segmentation task appears close to anatomical reference book.

2/The possibility to represent a FOD distribution in an anatomical structure may help to precisely locate a disease process. Indeed, a disease can locally involve a part of the brain or nerve structure without global anatomical modification.

MRI functional representation of the corpus callosum structure

Several MRI studies have established a topographical distribution of the fiber connections to the cortex in midsagittal cross sections of the corpus callosum. Witelson has defined five vertical partitions mainly based on primate data (prefrontal, premotor, motor, sensory, and parietotemporo-occipital). He has also described CC variation size depending on hand preference from postmortem measurement [123, 124]. The use of callosotomy for intractable epilepsy has provided a unique opportunity to study the effects of disconnection of the hemispheres, as it has

revealed that it is responsible for transferring information concerning specific sensory modalities.

Using DTI-based tractography, the Witelson's classification in the human corpus callosum has been confirmed with striking differences in the midbody and anterior third of the CC [126]. More recently, Track-weighted functional connectivity, which combine structural/functional connectivity information into a single image, has also proposed [108] a realistic parcellation of the corpus callosum. Here we have demonstrated that the Manifold Learning representation of the FOD is a potential tool to obtain such segmentation without tractography process. The clinical application are numerous, including exploration of patients with epilepsia, tinnitus [127] or mild traumatic brain injury [128]. This procedure gave promising results yet not perfect with some discontinuous clusters. Please not that postmortem atlases have also described overlap between functional parts of the CC as well tractographic studies. Is is now important to test the potential of the manifold analysis faced with a disease model.

2.4 Manifold Learning analysis of the acoustico-facial bundle : added value in neurovascular compression

Authors : Arnaud Attyé, Timothée Jacquesson, Alexandre Krainik, Adrian Kastler, Emmanuel Barbier, Felix Renard

Rationale

We have previously demonstrated the reliability of Manifold Learning analysis of the corpus callosum with DWI multi-shell data. Though less robust than those of Spectral Clustering for extraction of anatomical structure, building a manifold subspace of the Fiber Orientation Distribution (FOD) may be relevant for studying disease process. The Manifold Learning representation requires to compute a group atlas of the FOD in a dedicated brain or cranial nerve region before being applied to identify altered voxels in patients. With this regards, unsupervised machine learning method can be used in individuals to diagnose disease at the voxel or group of voxels level. The potential added value on scalar metrics, as usually extracted from methods of tractography, is the ability to take into account complex variation of the spherical harmonics representation in a global anatomic structure. It can be relevant either in healthy areas with multiple fiber population voxels or in voxels with pathological modification of the intra or extra-axonal compartment. In addition, the possibility to represent a FOD distribution in an anatomical structure may help to precisely locate a disease process or pathophysiology.

Meniere's Disease can include recurrent episodes of vertigo as main patients' complaint. It can be difficult to make the differential diagnosis with neurovascular compression of the acoustico-facial bundles, a complex disease process. Neurovascular compression syndromes are usually caused by arteries that directly contact the cisternal portion of a cranial nerve. Not all cases of neurovascular contact are clinically symptomatic [129]. The acoustico-facial bundle contains two nerves that can be potentially implied : the facial nerve is known to cause hemifacial spasm in cases of compression in a transition zone, and the cochleo-vestibular nerve compression would be implied in vestibular paroxysmia. While MRI morphological sequences are very efficient in diagnosing schwannomas, the relationship between nerve/vessel contact, as assessed with morphological sequences, and patient symptoms remains debated. In addition, T1-weighted or T2 weighted sequences failed in providing quantitative information about the nerve status. In DTI studies, neurovascular compression may reveal a loss of anisotropy that can be explained by tissue damage associated with demyelination [130, 131].

The presence of a "ground truth" surgical checking of the nerve state would be of great help to evaluate the interest of Manifold Learning in these patients. Since the surgical treatment of neurovascular compression is known to be efficient, providing possibilities of DWI-based diagnostic may be important to manage these patients.

The objective of this scientific article is :

1 / To build an atlas based on the approximation of a Riemaniann space of the acoustico-facial bundles' FOD in controls.

2 / To evaluate manifold learning interest in assessing the nerve structure of acoustic-facial bundles in patients surgically managed for neurovascular compression.

Methods

Population and MRI acquisition

Five surgically-managed patients with clinically confirmed intractable vestibular paroxysmia (n=3) and facial hemispasm (n=2) and 18 healthy volunteers were recruited between August 2015 and May 2018. Healthy subjects aged 40 or over, with no history of inner ear disorders were consecutively included in this study. Imaging examinations were carried out on a 3T Philips Achieva® TX MRI scanner equipped with Quasar Dual gradients and with a 32-channel SENSE head coil. The MRI protocol includes heavily-weighted T2 sequences, 3D-FLAIR sequences with whole-brain coverage and T1-weighted sequences with contrast media administration.

For the diffusion-weighted acquisition, we used a b-value of 1000 s/mm2 and 60 diffusion-weighting non-collinear directions distributed over four scans, each with 15 directions and one b=0 s/mm2 acquisition, as previously described [104]. Other parameters of the diffusion sequence were : single-shot spin-echo sequence ; TE/TR= 89/3300 ms ; acquired field of view : 224x224 mm2, voxel size : 2x2 mm2 ; 26 slices (2 mm slice thickness, no gap) ; SENSE factor= 1.9 ; NSA (number of signal averages) =2 ; nominal matrix 112x111 ; A-P ; water-fat shift : 15 pixels ; scan duration of 2'21" per 15 direction scan (total : 9'24"). To minimize movement, subjects were instructed to sight a fixed reference point using the head coil mirror.

Preprocessing

Preprocessing of diffusion-weighted images included denoising of data [91], eddy-current correction and motion correction [81] bias field correction and Gibbs artifacts' corrections [92], and up-sampling DWI spatial resolution by a factor in all three dimensions using cubic b-spline interpolation, to a voxel size of 1.3 mm3 [93]. All preprocessing steps were conducted using commands either implemented within MRtrix3 (www.mrtrix.org), or using MRtrix3 scripts that interfaced with external software packages. Spatial correspondence was achieved by first generating a group-specific population template with an iterative registration and averaging approach using FOD images from all the controls. Each subject's FOD image was then registered to the template via a FOD-guided non-linear registration [93]. We have estimated fiber orientation distributions using the Constrained Spherical Deconvolution model [77] using a group average RF as estimated with the *FA* algorithm.

Machine Learning algorithms

We have the Isomap (Isometric Feature Mapping) algorithm of Python SciKit Learn ToolBox, as previously described. We have then used an integrated kernel-based approach to voxel-based analysis that accurately estimates the underlying distribution of the obtained data. Indeed, individuals are now mapped into the reduced Euclidian space allowing to apply statistical test based on Probability Density Functions estimated with a Gaussian Kernel approach. We have subsequently classified patients using their distributions in our controlled space.

Manifold Learning : Atlas approach for individual diagnostic

We have firstly computed two atlas of the probabilities densities of the healthy acoustico-facial bundles, one for each side (ie. right internal auditory canals and left internal auditory canals) (figure 2.33). As amplitudes are metrics sensitive to FOD rotation, we needed to take into account different orientation for cranial nerves in the temporal bone. The Gaussian kernel density estimation allows to have a representation of the typical manifold subspace of volunteers left and right acoustico-facial bundles. We consider points outside the lines as potential outliers like voxels in background or artifacts.

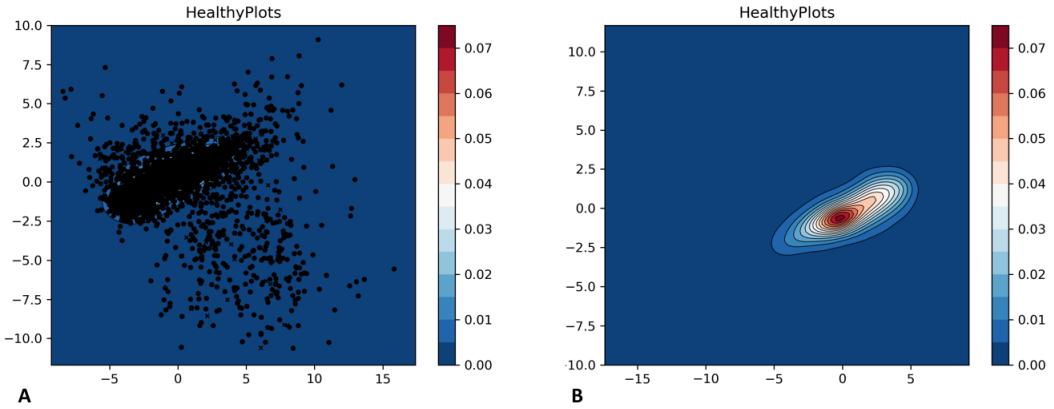

FIGURE 2.33 – A : The circle and cross points represents healthy FOD in the Manifold subspace. B : We have built the kernel density based on the points distribution. Blue lines represent low density areas white red lines represent high density areas. Please note the relative location of the kernel density representation in the manifold subspace between the two pictures.

The statistical distributions of the FOD distances were examined by considering the symmetric Kullback-Liebler distances on the probability density functions. It can be defined as follow : $D_{KL}(C,P) = \sum^i C(i) log \frac{C(i)}{P(i)} + \sum^i P(i) log \frac{P(i)}{C(i)}$, where C and P are the discretized distributions of the controls and the patient respectively. We firstly identify the mean distance between volunteers using a leave-one-control-out cross-validation setup. Indeed, all FOD distribution of each control will be in the manifold atlas, and we have evaluated the robustness of the manifold atlas based on the mean distance with −n FOD distributions.

corresponding to −n controls, n being the total number of controls. We have then tested p

patients separately. Thus, at each testing session, we have evaluated p+1 times the distances between FOD distributions, including all the patients and the leave-one-control-out procedure (figure 2.34). Please note that patients have been tested on the two sides to confirm the robustness of the method on asymptomatic bundles.

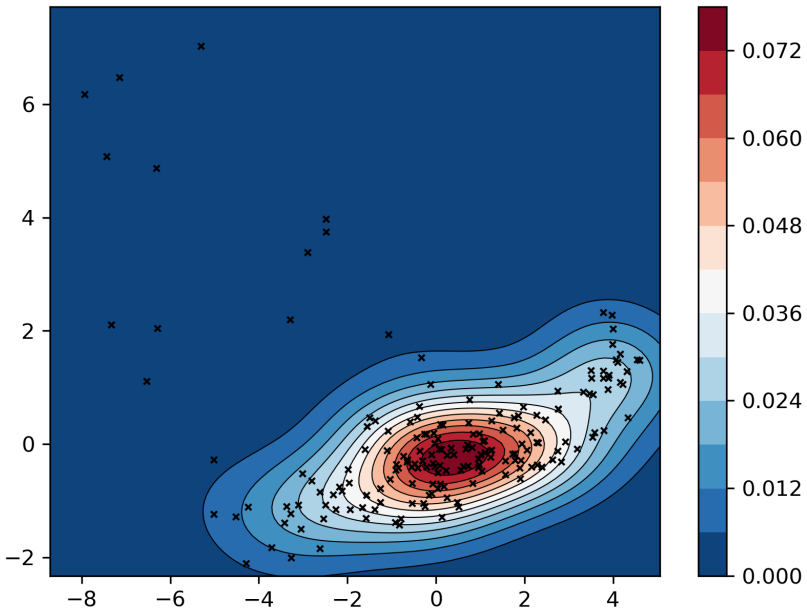

FIGURE 2.34 – Example of leave-one-control-out cross-validation setup. A : The cross points represents one randomly-excluded distribution of healthy FODs in the Manifold subspace, as compared with probabilities densities built on the others volunteers.

Statistically significant differences were detected between FOD distributions when permutation tests were performed on the resulting manifold atlas. We have then projected the Manifold analysis on FOD maps, to automatically detect the probabilities densities of each voxel along acoustico-facial bundles (figure 2.35). This is a relative value, which is set depending on the mean distance between controls, as evaluated during leave-one-control-out procedure.

Results

Manifold Learning analysis of patients with neurovascular compression.

The statistical distributions of the FOD distances between volunteers, as examined by considering the symmetric Kullback-Liebler distances on the probability density functions, were estimated as being 0.83 on the right sides (SD 0.43) and 0.56 on the left side (SD 0.31). The five patients presented with higher values side of the disease, respectively estimated as being

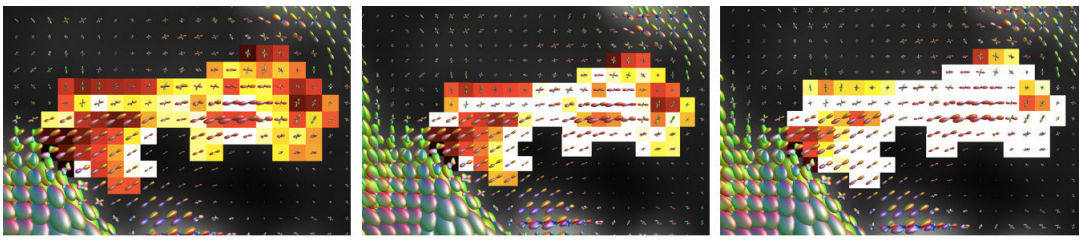

FIGURE 2.35 – Back projection of Manifold information onto the acoustico-facial left bundle of a patient with neurovascular compression. If the probability density has a relative high value in comparison with volunteers, the corresponding FOD appears with a dark color. The more the voxel is dark or red, the more the distance between the control group and the patient. We can vary the probability density to shift from the initial value (A) to a more permissive probabilities density (B and C), ie. by artificially increasing the mean distance between controls. (A) picture corresponds to the initial setting that classify numerous voxels of the bundle with an abnormal distance from volunteers' distribution.

3.12 and 4.78 for the two patients with facial hemispasm and 9.53 ; 3.17 and 4.53 for patients with vestibular paroxysmia. The five contralateral acoustico-facial bundles have distances within those of the control group. The figure 2.36 illustrates a typical difference of FOD distributions in the manifold subspace.

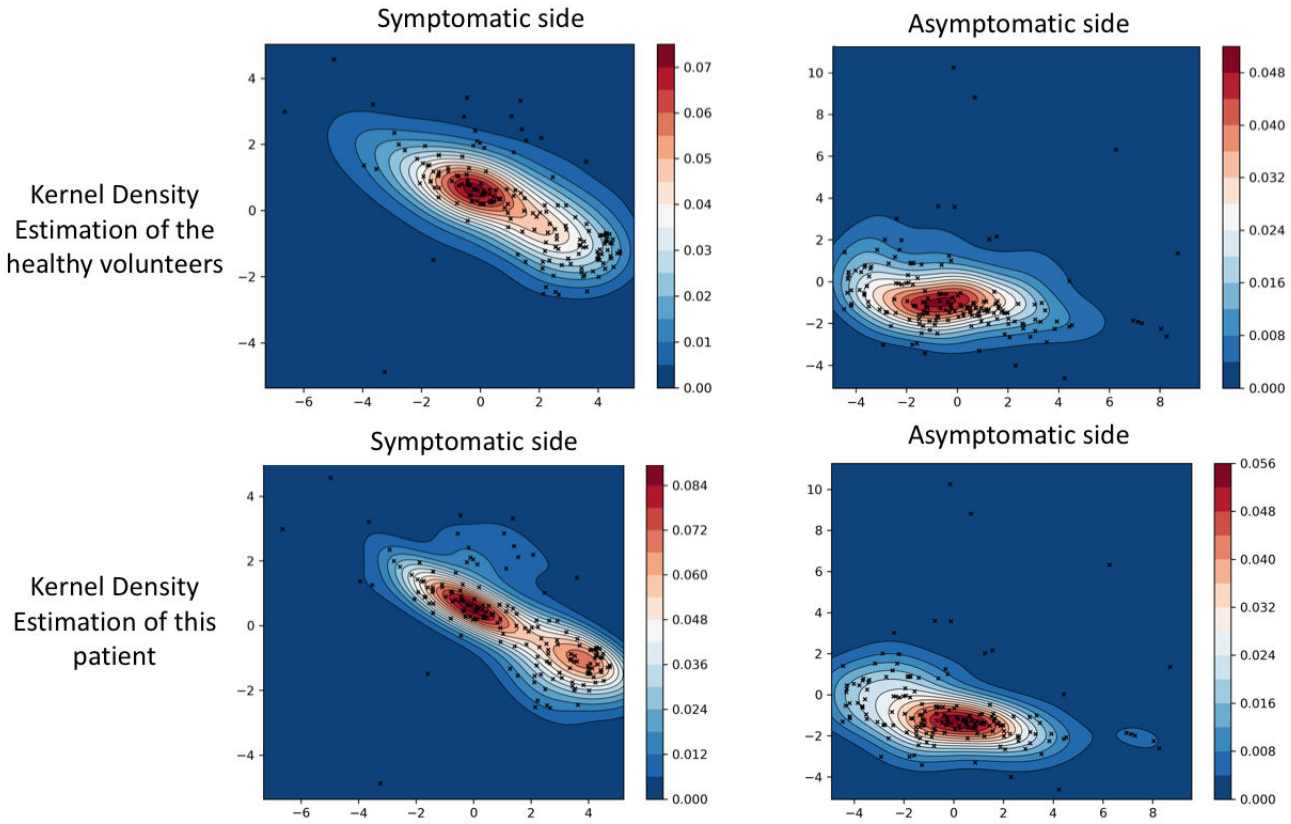

FIGURE 2.36 – Example of manifold subspaces representation in a subject with left vestibular paroxysmia. The left column represents the FOD of the symptomatic side while the right column represents the contralateral asymptomatic side. The first line represents the FOD locations with reference to the Manifold Atlas, as built on the control group. The second line represents the kernel density estimation of this patient. The diagnostic can be visually confirmed by comparing the shift of the Gaussian distribution between top left image and bottom left image. By contrast, on the asymptomatic sides the Gaussian distribution is roughly similar.

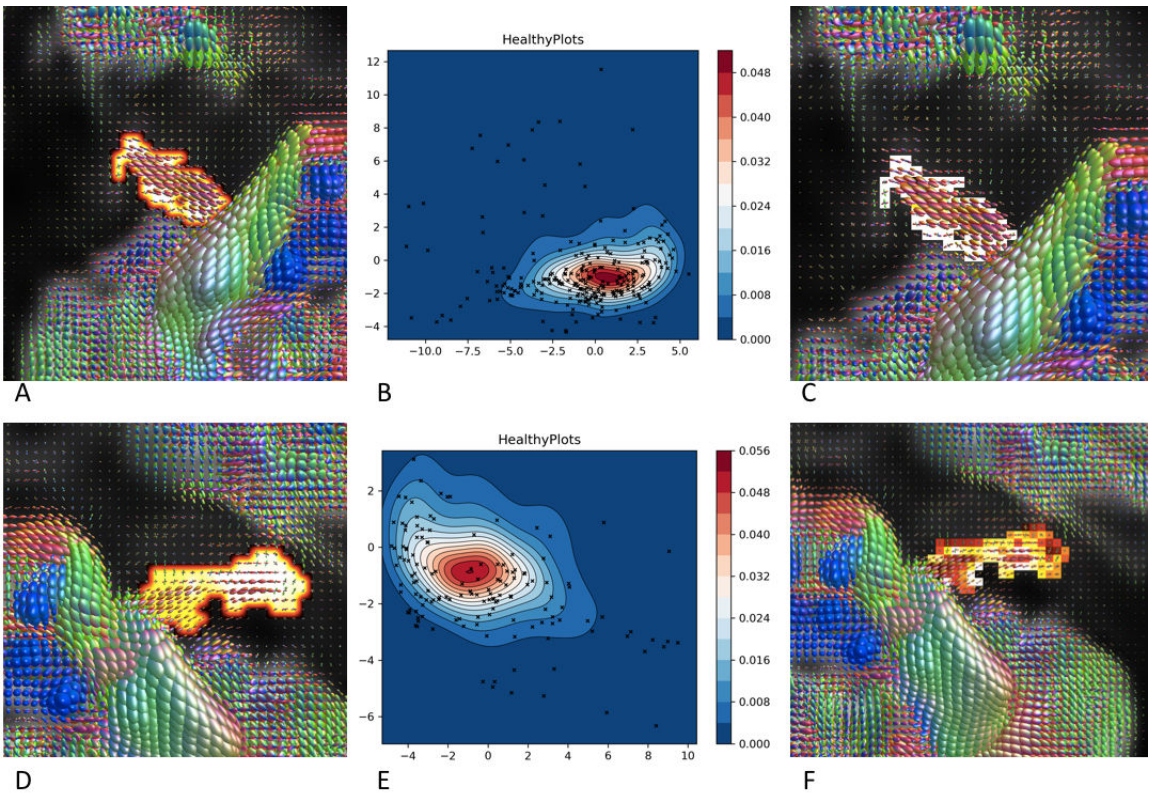

FIGURE 2.37 – Comparison between asymptomatic and symptomatic sides in a left-sided hemispasm facial patient. A and D : SC-based extraction of the acoustico-facial bundles. B : Manifold subspace representation of the healthy nerve onto the Manifold Atlas, with respect to the Gaussian distribution. E : Manifold subspace representation of the diseased nerve onto the Manifold Atlas, in which the vast majority of points are outside of the red lines (high density probabilities. C : Back projection of the Manifold information onto the right acoustico-facial bundle, estimated as normal with white voxels. F : Back projection of the Manifold information onto the left acoustico-facial bundle, estimated as abnormal merging voxels with high distance from controls.

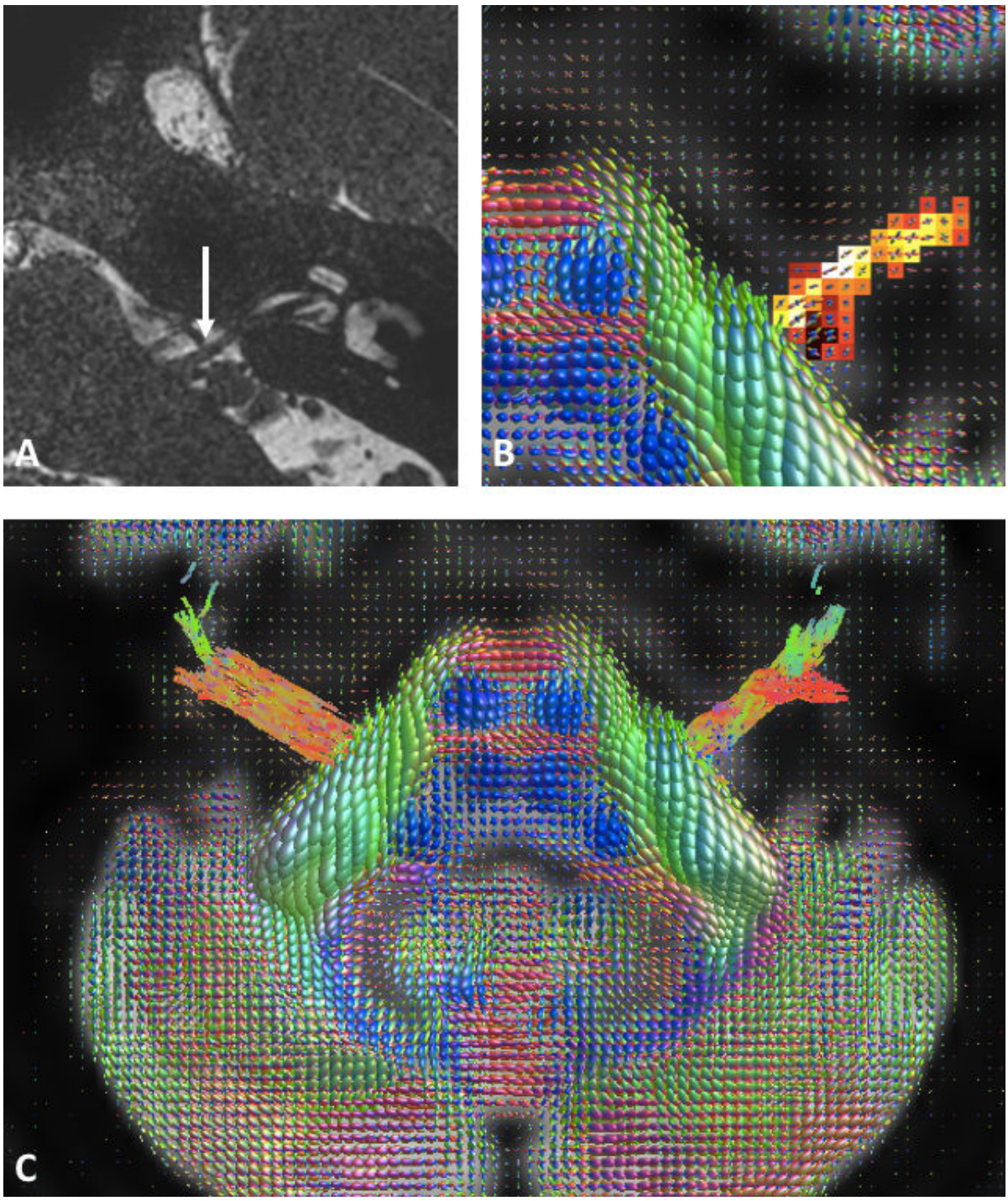

FIGURE 2.38 – Illustrative example of patient with left vestibular paroxysma. A : the close contact between the artery and the nerve, evaluated with T2-weighted imaging. B : The manifold back projection. C :The streamline tractography process, for comprehensive purpose.

Discussion

Individual MD diagnosis with Manifold Atlas

In Medicine, an atlas refers to a collection of images in a common template space, as extracted from a group of volunteers or patients. In DWI, metric such as AFD can be used to build this atlas, with the advantage of being reproducible over time and subjects, as previously demonstrated. The ability of the Manifold analysis to take into account complex variation of the Diffusion-Weighted Signal, as estimated with the CSD model, here enabled individual diagnostic.

The possibility to back projection of the Manifold Analysis on the FOD maps may help to precisely locate a disease process. Indeed, neurovascular compression can locally involve a part of the nerve structure without global modification. More generally, the statistical framework introduced in this paper proposed major advances in the field of diffusion MRI and statistical analysis. Firstly, as Diffusion-signal modelling is a sparse domain, using an algorithm that deals with the mathematical structure of the Fiber Orientation representation in a controlled subspace could allow expansion of this toolbox across models. We only need in this work to represent the diffusion signal through its peak amplitudes, though other relevant metrics could be tested. We can note that the constrain of positivity (imposed in various diffusion models) already implies to analyze the diffusion propagation in a non-Euclidean space [97, 119], making difficult the application of usual statistical tests.

Secondly, the proposed framework allows to perform analysis either at voxel or cluster level. The cluster's number of voxels may vary without difficulties to perform Manifold analysis. In a dedicated cluster, the addition of voxel information using the back projection may be relevant in various disease models. The absence of the need to smooth images is another strength of Manifold Learning analysis. The atlas approach enables in the same time individual diagnosis and group-based comparison. The use of kernel density estimation was only possible in such a reduced space, allowing to analyze data with non-Gaussian distribution.

Clinical Impact in patients with neurovascular compression

Neurovascular compression syndromes are usually caused by arteries or veins that directly contact the cisternal portion of a cranial nerve. Not all cases of neurovascular contact are clinically symptomatic. The transition zone between the central and peripheral myelin is the most vulnerable region for symptomatic neurovascular compression syndromes. Hemifacial spasm (cranial nerve VII) has a transition zone of 2.5 mm while vestibular paroxysmia (cranial nerve VIII) has a transition zone of 11 mm [129]. Symptomatic compressions are thought to occur in the transition zone yet there is no quantitative threshold for estimating whether a displaced nerve can be responsible for patients' symptoms. Here the Manifold analysis immediately provides a visual information on FOD alteration in these patients. The surgical confirmation of the nerve compression is crucial when attempting to validate a Machine Learning algorithm usefulness in

the clinical setting.

Limitations

Manifold learning can theoretically represent a FOD distribution based on small subset of controls, yet this assumption need to be tested on other disease models. The low number of patients is also problematic to confirm the value of the Manifold Learning at the individual level, though Neurovascular compression is a rare disease. By contrast with schwannomas, for which morphological enhanced MRI-sequences are informative, the association of morphological sequences with Diffusion-Weighted sequence seems to have a crucial role for diagnosing patients with neurovascular compression and improve their management. A future comparison with the fixel framework via directional Fiber Density coefficient would be interesting in such patients [86].

Finally, understanding the Manifold subspace representation can be difficult. In contrast to the Principal Component Analysis, the coordinates of the manifold space are not directly related to the extracted metric (here the FOD amplitude), owing to the need to capture the non-linear space of the diffusion-weighted data. The back projection process as itself is non-linear. The absence of relationship between the Manifold coordinates and a physically meaningful metric had difficulties in medical studies. To note, previous studies using the Isomap algorithm have demonstrated the robustness of the link between the natural space and the reduced manifold space that enables to observe the mathematical object in both spaces [117].

BIBLIOGRAPHIE

[1] C S Hallpike and H Cairns.
Observations on the Pathology of Ménière's Syndrome : (Section of Otology).
Proceedings of the Royal Society of Medicine, 31(11) :1317–1336, September 1938.
ISSN 0035-9157.

[2] Alec N. Salt and Stefan K. Plontke.
Endolymphatic hydrops : pathophysiology and experimental models.
Otolaryngologic Clinics of North America, 43(5) :971–983, October 2010.
ISSN 1557-8259.
doi : 10.1016/j.otc.2010.05.007.

[3] Jose A. Lopez-Escamez, John Carey, Won-Ho Chung, Joel A. Goebel, Måns Magnusson, Marco Mandalà, David E. Newman-Toker, Michael Strupp, Mamoru Suzuki, Franco Trabalzini, Alexandre Bisdorff, Classification Committee of the Barany Society, Japan Society for Equilibrium Research, European Academy of Otology and Neurotology (EAONO), Equilibrium Committee of the American Academy of Otolaryngology-Head and Neck Surgery (AAO-HNS), and Korean Balance Society.
Diagnostic criteria for Menière's disease.
Journal of Vestibular Research : Equilibrium & Orientation, 25(1) :1–7, 2015.
ISSN 1878-6464.
doi : 10.3233/VES-150549.

[4] S D Rauch, S N Merchant, and B A Thedinger.
Meniere's syndrome and endolymphatic hydrops. Double-blind temporal bone study.
The Annals of otology, rhinology, and laryngology, 98(11) :873–883, November 1989.
ISSN 0003-4894.

[5] K. C. Horner.
Review : morphological changes associated with endolymphatic hydrops.
Scanning Microscopy, 7(1) :223–238, March 1993.
ISSN 0891-7035.

[6] Ming-Yee Lin, Ferdinand C A Timmer, Brad S Oriel, Guangwei Zhou, John J Guinan, Sharon G Kujawa, Barbara S Herrmann, Saumil N Merchant, and Steven D Rauch.
Vestibular evoked myogenic potentials (VEMP) can detect asymptomatic saccular hydrops.
The Laryngoscope, 116(6) :987–992, June 2006.
ISSN 0023-852X.
doi : 10.1097/01.mlg.0000216815.75512.03.

[7] D. J. Pender.
Endolymphatic hydrops and Ménière's disease : a lesion meta-analysis.

The Journal of Laryngology and Otology, 128(10) :859–865, October 2014.
ISSN 1748-5460.
doi : 10.1017/S0022215114001972.

[8] Daniel J. Pender.
Membrane Stress in the Human Labyrinth and Meniere Disease : A Model Analysis.
International Archives of Otorhinolaryngology, 19(4) :336–342, October 2015.
ISSN 1809-9777.
doi : 10.1055/s-0035-1549157.

[9] Ömer Hızlı, Sebahattin Cureoglu, Serdar Kaya, Patricia A. Schachern, Michael M. Paparella, and Meredith E. Adams.
Quantitative Vestibular Labyrinthine Otopathology in Temporal Bones with Vestibular Schwannoma.
Otolaryngology–Head and Neck Surgery : Official Journal of American Academy of Otolaryngology-Head and Neck Surgery, 154(1) :150–156, January 2016.
ISSN 1097-6817.
doi : 10.1177/0194599815601070.

[10] Mohd Ridzo Mahmud, Aayesha M. Khan, and Joseph B. Nadol.
Histopathology of the inner ear in unoperated acoustic neuroma.
The Annals of Otology, Rhinology, and Laryngology, 112(11) :979–986, November 2003.
ISSN 0003-4894.
doi : 10.1177/000348940311201111.

[11] R. A. Schindler.
The ultrastructure of the endolymphatic sac in man.
The Laryngoscope, 90(6 Pt 2) :1–39, June 1980.
ISSN 0023-852X.

[12] Shinji Naganawa, Kojiro Suzuki, Masahiro Yamazaki, and Yasuo Sakurai.
Serial scans in healthy volunteers following intravenous administration of gadoteridol : time course of contrast enhancement in various cranial fluid spaces.
Magnetic resonance in medical sciences : MRMS : an official journal of Japan Society of Magnetic Resonance in Medicine, 13(1) :7–13, March 2014.
ISSN 1880-2206.

[13] Mina Park, Ho Sun Lee, Hyeonjin Kim, Seung Ha Oh, Jun Ho Lee, and Myung-Whan Suh.
Differences in perilymphatic space enhancement and adverse inflammatory reaction after intratympanic injection of two different gadolinium agents : A 9.4-T magnetic resonance imaging study.
Hearing Research, 333 :118–126, March 2016.
ISSN 1878-5891.
doi : 10.1016/j.heares.2015.10.022.

[14] S. Naganawa and M. Sone.
3d Real Inversion Recovery MR Imaging for the Visualization of Endolymphatic Hydrops.
AJNR. American journal of neuroradiology, September 2014.
ISSN 1936-959X.
doi : 10.3174/ajnr.A4126.

[15] Shinji Naganawa, Masahiro Yamazaki, Hisashi Kawai, Kiminori Bokura, Michihiko Sone, and Tsutomu Nakashima.

Estimation of perilymph enhancement after intratympanic administration of Gd-DTPA by fast T1-mapping with a dual flip angle 3d spoiled gradient echo sequence.
Magnetic resonance in medical sciences : MRMS : an official journal of Japan Society of Magnetic Resonance in Medicine, 12(3) :223–228, 2013.
ISSN 1880-2206.

[16] Tsutomu Nakashima, Shinji Naganawa, Ilmari Pyykko, William P R Gibson, Michihiko Sone, Seiichi Nakata, and Masaaki Teranishi.
Grading of endolymphatic hydrops using magnetic resonance imaging.
Acta oto-laryngologica. Supplementum, (560) :5–8, February 2009.
ISSN 0365-5237.
doi : 10.1080/00016480902729827.

[17] Arnaud Attyé, G. Dumas, I. Troprès, M. Roustit, A. Karkas, E. Banciu, J. Pietras, L. Lamalle, S. Schmerber, and A. Krainik.
Recurrent peripheral vestibulopathy : Is MRI useful for the diagnosis of endolymphatic hydrops in clinical practice ?
European Radiology, 25(10) :3043–3049, October 2015.
ISSN 1432-1084.
doi : 10.1007/s00330-015-3712-5.

[18] Arnaud Attyé, Michael Eliezer, Naïla Boudiaf, Irène Tropres, David Chechin, Sébastien Schmerber, Georges Dumas, and Alexandre Krainik.
MRI of endolymphatic hydrops in patients with Meniere's disease : a case-controlled study with a simplified classification based on saccular morphology.
European Radiology, December 2016.
ISSN 1432-1084.
doi : 10.1007/s00330-016-4701-z.

[19] A. Attyé, M. Eliezer, A. Galloux, J. Pietras, I. Tropres, S. Schmerber, G. Dumas, and A. Krainik.
Endolymphatic hydrops imaging : Differential diagnosis in patients with Meniere disease symptoms.
Diagnostic and Interventional Imaging, June 2017.
ISSN 2211-5684.
doi : 10.1016/j.diii.2017.06.002.

[20] Michael Eliezer, André Gillibert, Irène Tropres, Alexandre Krainik, and Arnaud Attyé.
Influence of inversion time on endolymphatic hydrops evaluation in 3d-FLAIR imaging.
Journal of Neuroradiology.
ISSN 0150-9861.
doi : 10.1016/j.neurad.2017.06.002.
URL `http://www.sciencedirect.com/science/article/pii/S015098611730250X`.

[21] M. Eliezer, G. Poillon, A. Gillibert, J. Horion, Y. Cruypeninck, E. Gerardin, N. Magne, and A. Attyé.
Comparison of enhancement of the vestibular perilymph between gadoterate meglumine and gadobutrol at 3-Tesla in Meniere's disease.
Diagnostic and Interventional Imaging, 99(5) :271–277, May 2018.
ISSN 2211-5684.
doi : 10.1016/j.diii.2018.01.002.

[22] J. Bykowski, J. P. Harris, M. Miller, J. Du, and M. F. Mafee.

Intratympanic Contrast in the Evaluation of Menière Disease : Understanding the Limits.
AJNR. American journal of neuroradiology, 36(7) :1326–1332, July 2015.
ISSN 1936-959X.
doi : 10.3174/ajnr.A4277.

[23] Stuart M. Grieve, Rupert Obholzer, Nathan Malitz, William P. Gibson, and Geoffrey D. Parker.
Imaging of endolymphatic hydrops in Meniere's disease at 1.5 T using phase-sensitive inversion recovery : (1) demonstration of feasibility and (2) overcoming the limitations of variable gadolinium absorption.
European Journal of Radiology, 81(2) :331–338, February 2012.
ISSN 1872-7727.
doi : 10.1016/j.ejrad.2011.01.073.

[24] Antonio Belinchon, Herminio Perez-Garrigues, Jose Maria Tenias, and Alberto Lopez.
Hearing assessment in Menière's disease.
The Laryngoscope, 121(3) :622–626, March 2011.
ISSN 1531-4995.
doi : 10.1002/lary.21335.

[25] Arnaud Attyé, Michael Eliezer, Maud Medici, Irène Tropres, Georges Dumas, Alexandre Krainik, and Sébastien Schmerber.
In vivo imaging of saccular hydrops in humans reflects sensorineural hearing loss rather than Meniere's disease symptoms.
European Radiology, March 2018.
ISSN 1432-1084.
doi : 10.1007/s00330-017-5260-7.

[26] Raphaële Quatre, Arnaud Attyé, Alexandre Karkas, Agnès Job, Georges Dumas, and Sébastien Schmerber.
Relationship Between Audio-Vestibular Functional Tests and Inner Ear MRI in Meniere's Disease.
Ear and Hearing, April 2018.
ISSN 1538-4667.
doi : 10.1097/AUD.0000000000000584.

[27] E. Ferrary and O. Sterkers.
Mechanisms of endolymph secretion.
Kidney International. Supplement, 65 :S98–103, April 1998.
ISSN 0098-6577.

[28] Nadia Aalling Jessen, Anne Sofie Finmann Munk, Iben Lundgaard, and Maiken Nedergaard.
The Glymphatic System : A Beginner's Guide.
Neurochemical Research, 40(12) :2583–2599, December 2015.
ISSN 1573-6903.
doi : 10.1007/s11064-015-1581-6.

[29] M. Ikeda and I. Sando.
Endolymphatic duct and sac in patients with Meniere's disease. A temporal bone histopathological study.
The Annals of Otology, Rhinology, and Laryngology, 93(6 Pt 1) :540–546, December 1984.
ISSN 0003-4894.

[30] Leslie Michaels and Sava Soucek.
The intravestibular source of the vestibular aqueduct. III : Osseous pathology of Ménière's disease, clarified by a developmental study of the intraskeletal channels of the otic capsule.

Acta Oto-Laryngologica, 130(7) :793–798, July 2010.
ISSN 1651-2251.
doi : 10.3109/00016480903443183.

[31] Takenori Miyashita, Yoshihiro Toyama, Ryuhei Inamoto, and Nozomu Mori.
Evaluation of the vestibular aqueduct in Ménière's disease using multiplanar reconstruction images of CT.
Auris, Nasus, Larynx, 39(6) :567–571, December 2012.
ISSN 1879-1476.
doi : 10.1016/j.anl.2011.11.005.

[32] Hideo Yamane, Kazuo Konishi, Hiramori Sakamaoto, Hidefumi Yamamoto, Naoki Matsushita, Masahiro Oishi, Hiroyoshi Iguchi, and Yuichi Inoue.
Practical 3dct imaging of the vestibular aqueduct for Meniere's disease.
Acta Oto-Laryngologica, 135(8) :799–806, August 2015.
ISSN 1651-2251.
doi : 10.3109/00016489.2015.1034879.

[33] A. N. Salt, J. J. Hartsock, R. M. Gill, E. King, F. B. Kraus, and S. K. Plontke.
Perilymph pharmacokinetics of locally-applied gentamicin in the guinea pig.
Hearing Research, 342 :101–111, December 2016.
ISSN 1878-5891.
doi : 10.1016/j.heares.2016.10.003.

[34] Tsutomu Nakashima, Shinji Naganawa, Makoto Sugiura, Masaaki Teranishi, Michihiko Sone, Hideo Hayashi, Seiichi Nakata, Naomi Katayama, and Ieda Maria Ishida.
Visualization of endolymphatic hydrops in patients with Meniere's disease.
The Laryngoscope, 117(3) :415–420, March 2007.
ISSN 0023-852X.
doi : 10.1097/MLG.0b013e31802c300c.

[35] H. Silverstein, P. T. Rowan, M. J. Olds, and S. I. Rosenberg.
Inner ear perfusion and the role of round window patency.
The American Journal of Otology, 18(5) :586–589, September 1997.
ISSN 0192-9763.

[36] D. Y. Kim, J. H. Lee, M. J. Goh, Y. S. Sung, Y. J. Choi, R. G. Yoon, S. H. Cho, J. H. Ahn, H. J. Park, and J. H. Baek.
Clinical significance of an increased cochlear 3d fluid-attenuated inversion recovery signal intensity on an MR imaging examination in patients with acoustic neuroma.
AJNR. American journal of neuroradiology, 35(9) :1825–1829, September 2014.
ISSN 1936-959X.
doi : 10.3174/ajnr.A3936.

[37] Shinji Naganawa, Hisashi Kawai, Michihiko Sone, Tsutomu Nakashima, and Mitsuru Ikeda.
Endolympathic hydrops in patients with vestibular schwannoma : visualization by non-contrast-enhanced 3d FLAIR.
Neuroradiology, 53(12) :1009–1015, December 2011.
ISSN 1432-1920.
doi : 10.1007/s00234-010-0834-y.

[38] Aïna Venkatasamy, Francis Veillon, Aude Fleury, Michael Eliezer, Maher Abu Eid, Benoit Romain, Hella Vuong, Dominique Rohmer, Anne Charpiot, Henri Sick, and Sophie Riehm.
Imaging of the saccule for the diagnosis of endolymphatic hydrops in Meniere disease, using a three-dimensional T2-weighted steady state free precession sequence : accurate, fast, and without contrast material intravenous injection.
European Radiology Experimental, 1(1) :14, 2017.
ISSN 2509-9280.
doi : 10.1186/s41747-017-0020-7.

[39] J. B. Nadol, J. C. Adams, and J. R. Kim.
Degenerative changes in the organ of Corti and lateral cochlear wall in experimental endolymphatic hydrops and human Menière's disease.
Acta Oto-Laryngologica. Supplementum, 519 :47–59, 1995.
ISSN 0365-5237.

[40] Norimasa Morita, Shin Kariya, Armin Farajzadeh Deroee, Sebahattin Cureoglu, Shigenobu Nomiya, Rie Nomiya, Tamotsu Harada, and Michael M Paparella.
Membranous labyrinth volumes in normal ears and Ménière disease : a three-dimensional reconstruction study.
The Laryngoscope, 119(11) :2216–2220, November 2009.
ISSN 1531-4995.
doi : 10.1002/lary.20723.

[41] A. R. Sepahdari, N. Vorasubin, G. Ishiyama, and A. Ishiyama.
Endolymphatic Hydrops Reversal following Acetazolamide Therapy : Demonstration with Delayed Intravenous Contrast-Enhanced 3d-FLAIR MRI.
AJNR. American journal of neuroradiology, 37(1) :151–154, January 2016.
ISSN 1936-959X.
doi : 10.3174/ajnr.A4462.

[42] David B. Allison, Richard M. Shiffrin, and Victoria Stodden.
Reproducibility of research : Issues and proposed remedies.
Proceedings of the National Academy of Sciences of the United States of America, 115(11) :2561–2562, March 2018.
ISSN 1091-6490.
doi : 10.1073/pnas.1802324115.

[43] Richard Van Noorden.
The science that's never been cited.
Nature, 552(7684) :162–164, 2017.
ISSN 1476-4687.
doi : 10.1038/d41586-017-08404-0.

[44] Robert Gürkov.
A WARNING ABOUT THE DRAWING OF WRONG CONCLUSIONS FROM A FAILURE TO REPRODUCE OTHER RESEARCHERS' FINDINGS.
Otology & Neurotology : Official Publication of the American Otological Society, American Neurotology Society [and] European Academy of Otology and Neurotology, March 2018.
ISSN 1537-4505.
doi : 10.1097/MAO.0000000000001770.

[45] Arnaud Attyé and Michael Eliezer.
MRI IDENTIFICATION OF THE SACCULE ? DO IT YOURSELF !
Otology & Neurotology : Official Publication of the American Otological Society, American Neurotology Society [and] European Academy of Otology and Neurotology, July 2018.
ISSN 1537-4505.
doi : 10.1097/MAO.0000000000001894.

[46] Irene Gazquez, Andres Soto-Varela, Ismael Aran, Sofia Santos, Angel Batuecas, Gabriel Trinidad, Herminio Perez-Garrigues, Carlos Gonzalez-Oller, Lourdes Acosta, and Jose A. Lopez-Escamez.
High prevalence of systemic autoimmune diseases in patients with Menière's disease.
PloS One, 6(10) :e26759, 2011.
ISSN 1932-6203.
doi : 10.1371/journal.pone.0026759.

[47] Lisa Caulley, Alexandra Quimby, Jacob Karsh, Azin Ahrari, Darren Tse, and Georgios Kontorinis.
Autoimmune arthritis in Ménière's disease : A systematic review of the literature.
Seminars in Arthritis and Rheumatism, November 2017.
ISSN 1532-866X.
doi : 10.1016/j.semarthrit.2017.11.008.

[48] Jessica S. Tyrrell, David J. D. Whinney, Obioha C. Ukoumunne, Lora E. Fleming, and Nicholas J. Osborne.
Prevalence, associated factors, and comorbid conditions for Ménière's disease.
Ear and Hearing, 35(4) :e162–169, August 2014.
ISSN 1538-4667.
doi : 10.1097/AUD.0000000000000041.

[49] Y. H. Cha, J. Brodsky, G. Ishiyama, C. Sabatti, and R. W. Baloh.
The relevance of migraine in patients with Meńière's disease.
Acta Oto-Laryngologica, 127(12) :1241–1245, December 2007.
ISSN 0001-6489.
doi : 10.1080/00016480701242469.

[50] Teresa Requena, Sonia Cabrera, Carmen Martín-Sierra, Steven D. Price, Anna Lysakowski, and José A. Lopez-Escamez.
Identification of two novel mutations in FAM136a and DTNA genes in autosomal-dominant familial Meniere's disease.
Human Molecular Genetics, 24(4) :1119–1126, February 2015.
ISSN 1460-2083.
doi : 10.1093/hmg/ddu524.

[51] Carmen Martín-Sierra, Alvaro Gallego-Martinez, Teresa Requena, Lidia Frejo, Angel Batuecas-Caletrío, and Jose A. Lopez-Escamez.
Variable expressivity and genetic heterogeneity involving DPT and SEMA3d genes in autosomal dominant familial Meniere's disease.
European journal of human genetics : EJHG, 25(2) :200–207, 2017.
ISSN 1476-5438.
doi : 10.1038/ejhg.2016.154.

[52] Carmen Martín-Sierra, Teresa Requena, Lidia Frejo, Steven D. Price, Alvaro Gallego-Martinez, Angel Batuecas-Caletrio, Sofía Santos-Pérez, Andrés Soto-Varela, Anna Lysakowski, and Jose A. Lopez-Escamez.

A novel missense variant in PRKCB segregates low-frequency hearing loss in an autosomal dominant family with Meniere's disease.
Human Molecular Genetics, 25(16) :3407–3415, 2016.
ISSN 1460-2083.
doi : 10.1093/hmg/ddw183.

[53] Herminio Perez-Garrigues, Jose A. Lopez-Escamez, Paz Perez, Ricardo Sanz, Miguel Orts, Jaime Marco, Rafael Barona, Mari C. Tapia, Ismael Aran, Carlos Cenjor, Nicolas Perez, Constantino Morera, and Rafael Ramirez.
Time course of episodes of definitive vertigo in Meniere's disease.
Archives of Otolaryngology–Head & Neck Surgery, 134(11) :1149–1154, November 2008.
ISSN 1538-361X.
doi : 10.1001/archotol.134.11.1149.

[54] John W. House, Joni K. Doherty, Laurel M. Fisher, M. Jennifer Derebery, and Karen I. Berliner.
Meniere's disease : prevalence of contralateral ear involvement.
Otology & Neurotology : Official Publication of the American Otological Society, American Neurotology Society [and] European Academy of Otology and Neurotology, 27(3) :355–361, April 2006.
ISSN 1531-7129.

[55] Tadao Yoshida, Satofumi Sugimoto, Masaaki Teranishi, Hironao Otake, Masahiro Yamazaki, Shinji Naganawa, Tsutomu Nakashima, and Michihiko Sone.
Imaging of the endolymphatic space in patients with Ménière's disease.
Auris, Nasus, Larynx, February 2017.
ISSN 1879-1476.
doi : 10.1016/j.anl.2017.02.002.

[56] Ali R. Sepahdari, Gail Ishiyama, Nopawan Vorasubin, Kevin A. Peng, Michael Linetsky, and Akira Ishiyama.
Delayed intravenous contrast-enhanced 3d FLAIR MRI in Meniere's disease : correlation of quantitative measures of endolymphatic hydrops with hearing.
Clinical Imaging, 39(1) :26–31, February 2015.
ISSN 1873-4499.
doi : 10.1016/j.clinimag.2014.09.014.

[57] Taeko Ito, Tadashi Kitahara, Hiroshi Inui, Toshiteru Miyasaka, Kimihiko Kichikawa, Ichiro Ota, Kazuhiko Nario, Yachiyo Matsumura, and Toshiaki Yamanaka.
Endolymphatic space size in patients with Meniere's disease and healthy controls.
Acta Oto-Laryngologica, 136(9) :879–882, September 2016.
ISSN 1651-2251.
doi : 10.3109/00016489.2016.1169556.

[58] John H. Keller, Barry E. Hirsch, Ryan S. Marovich, and Barton F. Branstetter.
Detection of endolymphatic hydrops using traditional MR imaging sequences.
American Journal of Otolaryngology, 38(4) :442–446, August 2017.
ISSN 1532-818X.
doi : 10.1016/j.amjoto.2017.01.038.

[59] François Simon, Jean-Pierre Guichard, Romain Kania, Julie Franc, Philippe Herman, and Charlotte Hautefort.
Saccular measurements in routine MRI can predict hydrops in Menière's disease.
European archives of oto-rhino-laryngology : official journal of the European Federation of Oto-Rhino-Laryngological Societies (EUFOS) : affiliated with the German Society for Oto-Rhino-Laryngology - Head and Neck Surgery, 274(12) :4113–4120, December 2017.

ISSN 1434-4726.
doi : 10.1007/s00405-017-4756-8.

[60] Shinji Naganawa, Masahiro Yamazaki, Hisashi Kawai, Kiminori Bokura, Michihiko Sone, and Tsutomu Nakashima.
Imaging of Ménière's disease after intravenous administration of single-dose gadodiamide : utility of subtraction images with different inversion time.
Magnetic resonance in medical sciences : MRMS : an official journal of Japan Society of Magnetic Resonance in Medicine, 11(3) :213–219, 2012.
ISSN 1880-2206.

[61] Mari Hagiwara, J. Thomas Roland, Xin Wu, Annette Nusbaum, James S. Babb, Pamela C. Roehm, Paul Hammerschlag, Anil K. Lalwani, and Girish Fatterpekar.
Identification of endolymphatic hydrops in Ménière's disease utilizing delayed postcontrast 3d FLAIR and fused 3d FLAIR and CISS color maps.
Otology & Neurotology : Official Publication of the American Otological Society, American Neurotology Society [and] European Academy of Otology and Neurotology, 35(10) :e337–342, December 2014.
ISSN 1537-4505.
doi : 10.1097/MAO.0000000000000585.

[62] Arnaud Attyé and Michael Eliezer.
Endolymphatic Hydrops : A Warning About the Interpretation of Magnetic Resonance Images Without Refreshed Knowledge of Inner Ear Endolymphatic Structure Anatomy.
Otology & Neurotology : Official Publication of the American Otological Society, American Neurotology Society [and] European Academy of Otology and Neurotology, 39(5) :654–655, June 2018.
ISSN 1537-4505.
doi : 10.1097/MAO.0000000000001769.

[63] Fang Liu, Weining Huang, Qinghua Chen, Xixi Meng, Zhenchang Wang, and Yuxia He.
Noninvasive evaluation of the effect of endolymphatic sac decompression in Ménière's disease using magnetic resonance imaging.
Acta Oto-Laryngologica, 134(7) :666–671, July 2014.
ISSN 1651-2251.
doi : 10.3109/00016489.2014.885118.

[64] Robert Gürkov, Wilhem Flatz, Birgit Ertl-Wagner, and Eike Krause.
Endolymphatic hydrops in the horizontal semicircular canal : a morphologic correlate for canal paresis in Ménière's disease.
The Laryngoscope, 123(2) :503–506, February 2013.
ISSN 1531-4995.
doi : 10.1002/lary.23395.

[65] H. Spoendlin, V. Balle, G. Bock, G. Bredberg, N. Danckwardt-Lillieström, H. Felix, M. Gleeson, L. G. Johnsson, L. Luciano, and H. Rask-Andersen.
Multicentre evaluation of the temporal bones obtained from a patient with suspected Menière's disease.
Acta Oto-Laryngologica. Supplementum, 499 :1–21, 1992.
ISSN 0365-5237.

[66] Chih-Ming Chang, Yi-Ho Young, Fu-Shan Jaw, Chi-Te Wang, and Po-Wen Cheng.

Degeneration of the vestibular nerve in unilateral Meniere's disease evaluated by galvanic vestibular-evoked myogenic potentials.
Clinical Neurophysiology : Official Journal of the International Federation of Clinical Neurophysiology, 128(9) : 1617–1624, 2017.
ISSN 1872-8952.
doi : 10.1016/j.clinph.2017.06.004.

[67] Saumil N. Merchant, Joe C. Adams, and Joseph B. Nadol.
Pathophysiology of Meniere's syndrome : are symptoms caused by endolymphatic hydrops ?
Otology & Neurotology : Official Publication of the American Otological Society, American Neurotology Society [and] European Academy of Otology and Neurotology, 26(1) :74–81, January 2005.
ISSN 1531-7129.

[68] Annika Henneberger, Birgit Ertl-Wagner, Maximilian Reiser, Robert Gürkov, and Wilhelm Flatz.
Morphometric evaluation of facial and vestibulocochlear nerves using magnetic resonance imaging : comparison of Menière's disease ears with normal hearing ears.
European archives of oto-rhino-laryngology : official journal of the European Federation of Oto-Rhino-Laryngological Societies (EUFOS) : affiliated with the German Society for Oto-Rhino-Laryngology - Head and Neck Surgery, 274(8) :3029–3039, August 2017.
ISSN 1434-4726.
doi : 10.1007/s00405-017-4616-6.

[69] Wilhelm H. Flatz, Annika Henneberger, Maximilian F. Reiser, Robert Gürkov, and Birgit Ertl-Wagner.
In Vivo Morphometric Analysis of Human Cranial Nerves Using Magnetic Resonance Imaging in Menière's Disease Ears and Normal Hearing Ears.
Journal of Visualized Experiments : JoVE, (132), 2018.
ISSN 1940-087X.
doi : 10.3791/57091.

[70] Timothée Jacquesson, Carole Frindel, Gabriel Kocevar, Moncef Berhouma, Emmanuel Jouanneau, Arnaud Attyé, and Francois Cotton.
Overcoming Challenges of Cranial Nerve Tractography : A Targeted Review.
Neurosurgery, July 2018.
ISSN 1524-4040.
doi : 10.1093/neuros/nyy229.

[71] D. Le Bihan, E. Breton, D. Lallemand, P. Grenier, E. Cabanis, and M. Laval-Jeantet.
MR imaging of intravoxel incoherent motions : application to diffusion and perfusion in neurologic disorders.
Radiology, 161(2) :401–407, November 1986.
ISSN 0033-8419.
doi : 10.1148/radiology.161.2.3763909.

[72] P. J. Basser.
Inferring microstructural features and the physiological state of tissues from diffusion-weighted images.
NMR in biomedicine, 8(7-8) :333–344, December 1995.
ISSN 0952-3480.

[73] C. Pierpaoli and P. J. Basser.
Toward a quantitative assessment of diffusion anisotropy.

Magnetic Resonance in Medicine : Official Journal of the Society of Magnetic Resonance in Medicine / Society of Magnetic Resonance in Medicine, 36(6) :893–906, December 1996.
ISSN 0740-3194.

[74] Shawna Farquharson, J-Donald Tournier, Fernando Calamante, Gavin Fabinyi, Michal Schneider-Kolsky, Graeme D Jackson, and Alan Connelly.
White matter fiber tractography : why we need to move beyond DTI.
Journal of neurosurgery, 118(6) :1367–1377, June 2013.
ISSN 1933-0693.
doi : 10.3171/2013.2.JNS121294.

[75] Maxime Descoteaux, Rachid Deriche, Thomas R Knösche, and Alfred Anwander.
Deterministic and probabilistic tractography based on complex fibre orientation distributions.
IEEE transactions on medical imaging, 28(2) :269–286, February 2009.
ISSN 1558-254X.
doi : 10.1109/TMI.2008.2004424.

[76] J-Donald Tournier, Fernando Calamante, David G Gadian, and Alan Connelly.
Direct estimation of the fiber orientation density function from diffusion-weighted MRI data using spherical deconvolution.
NeuroImage, 23(3) :1176–1185, November 2004.
ISSN 1053-8119.
doi : 10.1016/j.neuroimage.2004.07.037.

[77] J-Donald Tournier, Fernando Calamante, and Alan Connelly.
Robust determination of the fibre orientation distribution in diffusion MRI : non-negativity constrained super-resolved spherical deconvolution.
NeuroImage, 35(4) :1459–1472, May 2007.
ISSN 1053-8119.
doi : 10.1016/j.neuroimage.2007.02.016.

[78] Derek K. Jones, Thomas R. Knösche, and Robert Turner.
White matter integrity, fiber count, and other fallacies : the do's and don'ts of diffusion MRI.
NeuroImage, 73 :239–254, June 2013.
ISSN 1095-9572.
doi : 10.1016/j.neuroimage.2012.06.081.

[79] Ylva Lilja, Maria Ljungberg, Göran Starck, Kristina Malmgren, Bertil Rydenhag, and Daniel T. Nilsson.
Visualizing Meyer's loop : A comparison of deterministic and probabilistic tractography.
Epilepsy Research, 108(3) :481–490, March 2014.
ISSN 1872-6844.
doi : 10.1016/j.eplepsyres.2014.01.017.

[80] W. Koos, G. Kletter, F. Bock, and S. Salah.
[Microsurgery of bilateral tumors of the cerebellopontile angle].
Neuro-Chirurgie, 18(1) :75–76, February 1972.
ISSN 0028-3770.

[81] Jesper L. R. Andersson, Stefan Skare, and John Ashburner.
How to correct susceptibility distortions in spin-echo echo-planar images : application to diffusion tensor imaging.

NeuroImage, 20(2) :870–888, October 2003.
ISSN 1053-8119.
doi : 10.1016/S1053-8119(03)00336-7.

[82] P. Sampath, D. Rini, and D. M. Long.
Microanatomical variations in the cerebellopontine angle associated with vestibular schwannomas (acoustic neuromas) : a retrospective study of 1006 consecutive cases.
Journal of Neurosurgery, 92(1) :70–78, January 2000.
ISSN 0022-3085.
doi : 10.3171/jns.2000.92.1.0070.

[83] Amir Zolal, Stephan B. Sobottka, Dino Podlesek, Jennifer Linn, Bernhard Rieger, Tareq A. Juratli, Gabriele Schackert, and Hagen H. Kitzler.
Comparison of probabilistic and deterministic fiber tracking of cranial nerves.
Journal of Neurosurgery, 127(3) :613–621, September 2017.
ISSN 1933-0693.
doi : 10.3171/2016.8.JNS16363.

[84] Brendan Behan, David Q. Chen, Francesco Sammartino, Danielle D. DeSouza, Erika Wharton-Shukster, and Mojgan Hodaie.
Comparison of Diffusion-Weighted MRI Reconstruction Methods for Visualization of Cranial Nerves in Posterior Fossa Surgery.
Frontiers in Neuroscience, 11 :554, 2017.
ISSN 1662-4548.
doi : 10.3389/fnins.2017.00554.

[85] David Raffelt, J.-Donald Tournier, Stephen Rose, Gerard R. Ridgway, Robert Henderson, Stuart Crozier, Olivier Salvado, and Alan Connelly.
Apparent Fibre Density : a novel measure for the analysis of diffusion-weighted magnetic resonance images.
NeuroImage, 59(4) :3976–3994, February 2012.
ISSN 1095-9572.
doi : 10.1016/j.neuroimage.2011.10.045.

[86] David A. Raffelt, J.-Donald Tournier, Robert E. Smith, David N. Vaughan, Graeme Jackson, Gerard R. Ridgway, and Alan Connelly.
Investigating white matter fibre density and morphology using fixel-based analysis.
NeuroImage, 144(Pt A) :58–73, January 2017.
ISSN 1095-9572.
doi : 10.1016/j.neuroimage.2016.09.029.

[87] Kuldeep Kumar, Christian Desrosiers, Kaleem Siddiqi, Olivier Colliot, and Matthew Toews.
Fiberprint : A subject fingerprint based on sparse code pooling for white matter fiber analysis.
NeuroImage, 158 :242–259, 2017.
ISSN 1095-9572.
doi : 10.1016/j.neuroimage.2017.06.083.

[88] Eugenia Solano-Castiella, Alfred Anwander, Gabriele Lohmann, Marcel Weiss, Carol Docherty, Stefan Geyer, Enrico Reimer, Angela D. Friederici, and Robert Turner.
Diffusion tensor imaging segments the human amygdala in vivo.
NeuroImage, 49(4) :2958–2965, February 2010.

ISSN 1095-9572.
doi : 10.1016/j.neuroimage.2009.11.027.

[89] Qiuting Wen, Brian D. Stirling, Long Sha, Li Shen, Paul J. Whalen, and Yu-Chien Wu.
Parcellation of Human Amygdala Subfields Using Orientation Distribution Function and Spectral K-means Clustering.
Computational Diffusion MRI : MICCAI workshop, Athens, Greece, October 2016. CDMRI (Workshop) (8th : 2016 : Athens, Greece), 2016 :123–132, 2016.
doi : 10.1007/978-3-319-54130-3_10.

[90] Fernando Calamante, Robert E. Smith, Jacques-Donald Tournier, David Raffelt, and Alan Connelly.
Quantification of voxel-wise total fibre density : Investigating the problems associated with track-count mapping.
NeuroImage, 117 :284–293, May 2015.
ISSN 1095-9572.
doi : 10.1016/j.neuroimage.2015.05.070.

[91] Jelle Veraart, Dirk H. J. Poot, Wim Van Hecke, Ines Blockx, Annemie Van der Linden, Marleen Verhoye, and Jan Sijbers.
More accurate estimation of diffusion tensor parameters using diffusion Kurtosis imaging.
Magnetic Resonance in Medicine : Official Journal of the Society of Magnetic Resonance in Medicine / Society of Magnetic Resonance in Medicine, 65(1) :138–145, January 2011.
ISSN 1522-2594.
doi : 10.1002/mrm.22603.

[92] Nicholas J. Tustison, Brian B. Avants, Philip A. Cook, Yuanjie Zheng, Alexander Egan, Paul A. Yushkevich, and James C. Gee.
N4itk : improved N3 bias correction.
IEEE transactions on medical imaging, 29(6) :1310–1320, June 2010.
ISSN 1558-254X.
doi : 10.1109/TMI.2010.2046908.

[93] David Raffelt, J.-Donald Tournier, Stuart Crozier, Alan Connelly, and Olivier Salvado.
Reorientation of fiber orientation distributions using apodized point spread functions.
Magnetic Resonance in Medicine, 67(3) :844–855, March 2012.
ISSN 1522-2594.
doi : 10.1002/mrm.23058.

[94] Ben Jeurissen, Jacques-Donald Tournier, Thijs Dhollander, Alan Connelly, and Jan Sijbers.
Multi-tissue constrained spherical deconvolution for improved analysis of multi-shell diffusion MRI data.
NeuroImage, 103 :411–426, December 2014.
ISSN 1095-9572.
doi : 10.1016/j.neuroimage.2014.07.061.

[95] P. E. Shrout and J. L. Fleiss.
Intraclass correlations : uses in assessing rater reliability.
Psychological Bulletin, 86(2) :420–428, March 1979.
ISSN 0033-2909.

[96] J. M. Bland and D. G. Altman.
Statistical methods for assessing agreement between two methods of clinical measurement.

Lancet (London, England), 1(8476) :307–310, February 1986.
ISSN 0140-6736.

[97] Alvina Goh, Christophe Lenglet, Paul M. Thompson, and René Vidal.
A nonparametric Riemannian framework for processing high angular resolution diffusion images and its applications to ODF-based morphometry.
NeuroImage, 56(3) :1181–1201, June 2011.
ISSN 1095-9572.
doi : 10.1016/j.neuroimage.2011.01.053.

[98] Thomas Schultz and Gordon L. Kindlmann.
Open-box spectral clustering : applications to medical image analysis.
IEEE transactions on visualization and computer graphics, 19(12) :2100–2108, December 2013.
ISSN 1941-0506.
doi : 10.1109/TVCG.2013.181.

[99] Lisa Willats, David Raffelt, Robert E. Smith, J.-Donald Tournier, Alan Connelly, and Fernando Calamante.
Quantification of track-weighted imaging (TWI) : characterisation of within-subject reproducibility and between-subject variability.
NeuroImage, 87 :18–31, February 2014.
ISSN 1095-9572.
doi : 10.1016/j.neuroimage.2013.11.016.

[100] Wonil Joo, Fumitaka Yoshioka, Takeshi Funaki, Koji Mizokami, and Albert L. Rhoton.
Microsurgical anatomy of the trigeminal nerve.
Clinical Anatomy (New York, N.Y.), 27(1) :61–88, January 2014.
ISSN 1098-2353.
doi : 10.1002/ca.22330.

[101] Wonil Joo and Albert L. Rhoton.
Microsurgical anatomy of the trochlear nerve.
Clinical Anatomy (New York, N.Y.), 28(7) :857–864, October 2015.
ISSN 1098-2353.
doi : 10.1002/ca.22602.

[102] René-Charles Rouchy, Arnaud Attyé, Maud Medici, Félix Renard, Adrian Kastler, Sylvie Grand, Irène Tropres, Christian Adrien Righini, and Alexandre Krainik.
Facial nerve tractography : A new tool for the detection of perineural spread in parotid cancers.
European Radiology, April 2018.
ISSN 1432-1084.
doi : 10.1007/s00330-018-5318-1.

[103] Lauren J. O'Donnell and Carl-Fredrik Westin.
Automatic tractography segmentation using a high-dimensional white matter atlas.
IEEE transactions on medical imaging, 26(11) :1562–1575, November 2007.
ISSN 0278-0062.
doi : 10.1109/TMI.2007.906785.

[104] J. Dubois, C. Poupon, F. Lethimonnier, and D. Le Bihan.
Optimized diffusion gradient orientation schemes for corrupted clinical DTI data sets.

Magma (New York, N.Y.), 19(3) :134–143, August 2006.
ISSN 0968-5243.
doi : 10.1007/s10334-006-0036-0.

[105] J-Donald Tournier, Fernando Calamante, and Alan Connelly.
Determination of the appropriate b value and number of gradient directions for high-angular-resolution diffusion-weighted imaging.
NMR in biomedicine, 26(12) :1775–1786, December 2013.
ISSN 1099-1492.
doi : 10.1002/nbm.3017.

[106] Alessandro Calamuneri, Alessandro Arrigo, Enricomaria Mormina, Demetrio Milardi, Alberto Cacciola, Gaetana Chillemi, Silvia Marino, Michele Gaeta, and Angelo Quartarone.
White Matter Tissue Quantification at Low b-Values Within Constrained Spherical Deconvolution Framework.
Frontiers in Neurology, 9 :716, 2018.
ISSN 1664-2295.
doi : 10.3389/fneur.2018.00716.

[107] Robert E. Smith, Jacques-Donald Tournier, Fernando Calamante, and Alan Connelly.
SIFT : Spherical-deconvolution informed filtering of tractograms.
NeuroImage, 67 :298–312, February 2013.
ISSN 1095-9572.
doi : 10.1016/j.neuroimage.2012.11.049.

[108] Fernando Calamante.
Track-weighted imaging methods : extracting information from a streamlines tractogram.
Magma (New York, N.Y.), February 2017.
ISSN 1352-8661.
doi : 10.1007/s10334-017-0608-1.

[109] Arnaud Attyé, Clément Jean, Perrine Remond, Carole Peyrin, Augustin Lecler, Naïla Boudiaf, Florent Aptel, Christophe Chiquet, Laurent Lamalle, and Alexandre Krainik.
Track-weighted imaging for neuroretina : Evaluations in healthy volunteers and ischemic optic neuropathy.
Journal of magnetic resonance imaging : JMRI, January 2018.
ISSN 1522-2586.
doi : 10.1002/jmri.25941.

[110] Arnaud Attyé, Alexandre Karkas, Irène Troprès, Matthieu Roustit, Adrian Kastler, Georges Bettega, Laurent Lamalle, Félix Renard, Christian Righini, and Alexandre Krainik.
Parotid gland tumours : MR tractography to assess contact with the facial nerve.
European Radiology, October 2015.
ISSN 1432-1084.
doi : 10.1007/s00330-015-4049-9.

[111] Ravi N. Samy, Lisa Houston, Michael Scott, Daniel I. Choo, and Jareen Meinzen-Derr.
Cochlear implantation in patients with Meniere's disease.
Cochlear Implants International, 16(4) :208–212, July 2015.
ISSN 1754-7628.
doi : 10.1179/1754762814Y.0000000104.

[112] Paul Mick, Hosam Amoodi, Christoph Arnoldner, David Shipp, Lendra Friesen, Vincent Lin, Julian Nedzelski, and Joseph Chen.
Cochlear implantation in patients with advanced Ménière's disease.
Otology & Neurotology : Official Publication of the American Otological Society, American Neurotology Society [and] European Academy of Otology and Neurotology, 35(7) :1172–1178, August 2014.
ISSN 1537-4505.
doi : 10.1097/MAO.0000000000000202.

[113] Theodore Richardson McRackan, Rene H. Gifford, Charissa N. Kahue, Robert Dwyer, Robert F. Labadie, George B. Wanna, David S. Haynes, and Marc L. Bennett.
Cochlear implantation in Ménière's disease patients.
Otology & Neurotology : Official Publication of the American Otological Society, American Neurotology Society [and] European Academy of Otology and Neurotology, 35(3) :421–425, March 2014.
ISSN 1537-4505.
doi : 10.1097/MAO.0000000000000247.

[114] Robert E Smith, Jacques-Donald Tournier, Fernando Calamante, and Alan Connelly.
Anatomically-constrained tractography : improved diffusion MRI streamlines tractography through effective use of anatomical information.
NeuroImage, 62(3) :1924–1938, September 2012.
ISSN 1095-9572.
doi : 10.1016/j.neuroimage.2012.06.005.

[115] Bo Zhu, Jeremiah Z. Liu, Stephen F. Cauley, Bruce R. Rosen, and Matthew S. Rosen.
Image reconstruction by domain-transform manifold learning.
Nature, 555(7697) :487–492, 2018.
ISSN 1476-4687.
doi : 10.1038/nature25988.

[116] Samuel Gerber, Tolga Tasdizen, P. Thomas Fletcher, Sarang Joshi, Ross Whitaker, and Alzheimers Disease Neuroimaging Initiative (ADNI).
Manifold modeling for brain population analysis.
Medical Image Analysis, 14(5) :643–653, October 2010.
ISSN 1361-8423.
doi : 10.1016/j.media.2010.05.008.

[117] J. B. Tenenbaum, V. de Silva, and J. C. Langford.
A global geometric framework for nonlinear dimensionality reduction.
Science (New York, N.Y.), 290(5500) :2319–2323, December 2000.
ISSN 0036-8075.
doi : 10.1126/science.290.5500.2319.

[118] Rajeev Kumar Verma, Raimund Kottke, Lukas Andereggen, Christian Weisstanner, Christoph Zubler, Jan Gralla, Claus Kiefer, Johannes Slotboom, Roland Wiest, Gerhard Schroth, Christoph Ozdoba, and Marwan El-Koussy.
Detecting subarachnoid hemorrhage : Comparison of combined FLAIR/SWI versus CT.
European journal of radiology, April 2013.
ISSN 1872-7727.
doi : 10.1016/j.ejrad.2013.03.021.

[119] Vincent Arsigny, Pierre Fillard, Xavier Pennec, and Nicholas Ayache.
Log-Euclidean metrics for fast and simple calculus on diffusion tensors.
Magnetic Resonance in Medicine, 56(2) :411–421, August 2006.
ISSN 0740-3194.
doi : 10.1002/mrm.20965.

[120] Jelle Veraart, Dmitry S. Novikov, Daan Christiaens, Benjamin Ades-Aron, Jan Sijbers, and Els Fieremans.
Denoising of diffusion MRI using random matrix theory.
NeuroImage, 142 :394–406, November 2016.
ISSN 1095-9572.
doi : 10.1016/j.neuroimage.2016.08.016.

[121] Kuldeep Kumar, Matthew Toews, Laurent Chauvin, Olivier Colliot, and Christian Desrosiers.
Multi-modal brain fingerprinting : A manifold approximation based framework.
NeuroImage, 183 :212–226, December 2018.
ISSN 1095-9572.
doi : 10.1016/j.neuroimage.2018.08.006.

[122] Saket Anand, Sushil Mittal, Oncel Tuzel, and Peter Meer.
Semi-Supervised Kernel Mean Shift Clustering.
IEEE transactions on pattern analysis and machine intelligence, 36(6) :1201–1215, June 2014.
ISSN 1939-3539.
doi : 10.1109/TPAMI.2013.190.

[123] S. F. Witelson.
Hand and sex differences in the isthmus and genu of the human corpus callosum. A postmortem morphological study.
Brain : A Journal of Neurology, 112 (Pt 3) :799–835, June 1989.
ISSN 0006-8950.

[124] S. F. Witelson.
The brain connection : the corpus callosum is larger in left-handers.
Science (New York, N.Y.), 229(4714) :665–668, August 1985.
ISSN 0036-8075.

[125] Parmeshwar Khurd, Ragini Verma, and Christos Davatzikos.
Kernel-based manifold learning for statistical analysis of diffusion tensor images.
Information Processing in Medical Imaging : Proceedings of the ... Conference, 20 :581–593, 2007.
ISSN 1011-2499.

[126] Sabine Hofer and Jens Frahm.
Topography of the human corpus callosum revisited–comprehensive fiber tractography using diffusion tensor magnetic resonance imaging.
NeuroImage, 32(3) :989–994, September 2006.
ISSN 1053-8119.
doi : 10.1016/j.neuroimage.2006.05.044.

[127] Eugen Diesch, Verena Schummer, Martin Kramer, and Andre Rupp.
Structural changes of the corpus callosum in tinnitus.
Frontiers in Systems Neuroscience, 6 :17, 2012.

ISSN 1662-5137.
doi : 10.3389/fnsys.2012.00017.

[128] Aurélie Delouche, Arnaud Attyé, Olivier Heck, Sylvie Grand, Adrian Kastler, Laurent Lamalle, Felix Renard, and Alexandre Krainik.
Diffusion MRI : Pitfalls, literature review and future directions of research in mild traumatic brain injury.
European Journal of Radiology, 85(1) :25–30, January 2016.
ISSN 1872-7727.
doi : 10.1016/j.ejrad.2015.11.004.

[129] S. Haller, L. Etienne, E. Kövari, A. D. Varoquaux, H. Urbach, and M. Becker.
Imaging of Neurovascular Compression Syndromes : Trigeminal Neuralgia, Hemifacial Spasm, Vestibular Paroxysmia, and Glossopharyngeal Neuralgia.
AJNR. American journal of neuroradiology, 37(8) :1384–1392, 2016.
ISSN 1936-959X.
doi : 10.3174/ajnr.A4683.

[130] Sami H. Erbay, Rafeeque A. Bhadelia, Mark O'Callaghan, Punita Gupta, Ron Riesenburger, Warren Krackov, and Joseph F. Polak.
Nerve atrophy in severe trigeminal neuralgia : noninvasive confirmation at MR imaging–initial experience.
Radiology, 238(2) :689–692, February 2006.
ISSN 0033-8419.
doi : 10.1148/radiol.2382042214.

[131] C. Herweh, B. Kress, D. Rasche, V. Tronnier, J. Tröger, K. Sartor, and C. Stippich.
Loss of anisotropy in trigeminal neuralgia revealed by diffusion tensor imaging.
Neurology, 68(10) :776–778, March 2007.
ISSN 1526-632X.
doi : 10.1212/01.wnl.0000256340.16766.1d.